ROMA TRE UNIVERSITY

SCIENCE DEPARTMENT

PhD programme in Science of Matter and Nanomaterials

Ge/SiGe heterostructures for opto-electronic applications

Tutors:
Prof.ssa Monica De Seta
Prof. Giovanni Capellini

Candidate:
Elena Campagna

XXXVIII cycle PhD courses

CONTENTS

ACRONYMS

Si Silicon

Ge Germanium

QWs Quantum Wells

PQWs Parabolic Quantum Wells

IBT Interband transition

ISBT Intersubband transitions

VB valence band

CB conduction band

MD misfit dislocations

TD threading dislocations

USC ultra-strong coupling

CVD Chemical Vapor Deposition

UHV ultra-high vacuum

INTRODUCTION

The terahertz (THz) frequency range, typically defined between 0.1 and 10 THz, remains one of the least exploited regions of the electromagnetic spectrum. Despite its high potential for applications in spectroscopy, imaging, security, non-destructive diagnostics, and high-speed wireless communications, the so-called *THz gap*, i.e. the limited availability of compact, efficient, and integrable sources and detectors persists [1, 2, 3]. In this context, semiconductor quantum structures based on Intersubband transitions (ISBT) in Quantum Wells (QWs) have proven to be excellent candidates for the realization of THz optoelectronic devices, including quantum cascade lasers and photodetectors [4].

In recent years, the integration of intersubband systems into optical microcavities has made it possible to explore the regimes of *strong* and ultra-strong light-matter coupling [5]. In these conditions, the Rabi frequency Ω_R, which quantifies the rate of coherent energy exchange between cavity photons and intersubband transitions, becomes comparable to or larger than the bare intersubband transition frequency ω_0. As a result, hybrid quasiparticles, the *intersubband polaritons*, are formed, whose dispersion relation can be engineered through the design of the heterostructure and precise control of the doping. The normalized coupling ratio $\eta = \frac{\Omega_R}{\omega_0}$ is commonly used to identify the ultra-strong coupling (USC) regime, typically defined for $\eta \gtrsim 0.1$ [6]. In ISBTs, the Rabi frequency scales as $\Omega_R \propto \sqrt{n_{2D}}$; consequently, the ratio η can be enhanced by increasing the doping level and reducing the transition energy ω_0, thus favoring the THz spectral range. Access to such regimes in the THz range opens pathways toward novel functionalities, including non-classical light generation, polaritonic modulators, and quantum-information-oriented photonic devices.

Achieving accurate control of the transition energy, linewidth, and oscillator strength in the THz range, however, remains challenging. In conventional square quantum wells, many-body effects play a prominent role; in particular, the depolarization shift produces a blue-shift of the transition energy that increases with electron density, and its magnitude differs for each pair of subbands. Consequently, devices based on square QWs often exhibit absorption spectra that are broad, multipeak, and highly sensitive to temperature. Parabolic Quantum Wells (PQWs) offers a solution to these limitations. In fact, their harmonic confinement potential leads to equally spaced subbands, and in modulation-doped structures, the depolarization shift is canceled in accordance with Kohn's theorem [7]. As a result, a single, well-defined intersubband resonance emerges, whose energy is largely insensitive to the carrier density and the occupation of higher subbands. This robustness against temperature and doping variations makes PQWs particularly attractive for high-performance THz devices and for the exploration of strong and ultra-strong coupling regimes [6, 8]. Indeed, PQWs based on III-V semiconductors have enabled some of the highest values of η reported in the literature, including demonstrations of room temperature operation in optoelectronic devices.

While the majority of PQWs implementations have historically been based on III-V materials, group-IV semiconductors, particularly Ge/SiGe heterostructures, have recently emerged as a promising alternative. These materials can be manufactured with processes and methods compatible with the state-of-the art Si-CMOS technology, reduced electron effective masses, and simplified subband structure in the conduction band of n-type Ge-rich wells [3]. In particular, $Si_{1-x}Ge_x$ PQWs with $x > 0.8$ provide an advantageous platform for THz ISBT-based devices due to the possibility of achieving narrow absorption linewidths. An additional key advantage is the absence of the Reststrahlen band: unlike III-V compounds, whose polar nature leads to strong phonon absorption and limits operation above 5 THz, SiGe is non-polar and therefore transparent over a much broader spectral window, enabling devices to operate throughout the entire 1-10 THz range.

The fabrication of high-quality Ge/SiGe PQWs on Si remains technologically challenging. The 4.2% lattice mismatch between Germanium (Ge) and Silicon (Si) can lead to threading dislocations, crosshatch patterns, and plastic relaxation, requiring highly controlled growth conditions and refined strain-engineering strategies [9]. Further complications arise from Ge surface segregation, Si-Ge interdiffusion, and donor migration during epitaxy, which makes it difficult to control the epitaxy at the sub-nanometer level, as required by the heterostructure design. Despite these challenges, recent advances in UHV-CVD growth have enabled the fabrication of high-quality Ge/SiGe PQWs with excellent control of composition and doping across multiple periods.

These structures show a single, narrow ISBT resonance whose energy remains independent of doping level and temperature, consistent with the quasi-harmonic potential landscape [10].

A critical aspect of designing these devices is the optimization of modulation doping. In n-type Ge/SiGe PQWs, donors placed in the barriers transfer electrons into the Ge-rich well, where the conduction-band minimum lies in the L valleys. The efficiency of this charge transfer depends sensitively on the alignment of the band minima between barriers and wells, which is dictated by epitaxial strain and by temperature-dependent thermal strain.

The main objective of this PhD thesis is the design and physical characterization of Ge/SiGe parabolic quantum wells (PQWs) grown on silicon substrates, with particular emphasis on their application to THz intersubband photonics. The work focuses on the epitaxial growth, structural and optical characterization, and device-level integration of Ge/SiGe heterostructures, culminating in their incorporation into microcavities operating in the USC regime.

By combining HR-XRD, FTIR spectroscopy and multivalley Schrödinger-Poisson simulations, we have illustrated how the separation between the Δ and L valleys in the barriers, together with the strain field, governs charge-transfer efficiency. These analyzes provide key guidelines for correlating doping density, well width, and strain state with the achievable electron concentration and the resulting ISBT oscillator strength, both of which are essential for THz device optimization and for tailoring light-matter coupling.

Furthermore, we achieved the full integration of Ge/SiGe PQWs into THz microcavities operating in the strong and ultra-strong coupling regimes, marking a significant step toward a fully group-IV THz photonic platform. By incorporating modulation-doped PQWs into plasmonic patch-antenna resonators, we demonstrated the USC regime at frequencies around 3.1 THz, with a normalized coupling ratio of $\Omega_R/\omega_0 \approx 0.2$ maintained from cryogenic to room temperature. Finally, through the use of heavily doped SiGe layers as plasmonic mirrors, we realized fully semiconductor THz microcavities compatible with silicon photonics. These devices exhibit polaritonic quality factors exceeding unity even at room temperature, enabling amplitude modulation and tunable absorption in the THz range and broadening the accessible USC regime within group-IV material platforms.

The thesis is organized as follows:

- Chapter 1 provides a general introduction to the materials employed, the properties of SiGe alloys, the physical fundamentals of quantum wells and intersubband transitions, and the principles of strong and ultra-strong coupling in microcavities.

- Chapter 2 describes the theoretical model and the procedure used for the growth and analysis of the experimental results throughout the project. Particular emphasis is placed on UHV-CVD epitaxial growth, as well as on the structural and optical characterization methods employed (AFM, HR-XRD, FTIR, and Schrödinger-Poisson simulations on the theory side).

- Chapter 3 presents and contextualizes the first scientific publication produced during the PhD, which is dedicated to the demonstration of high-quality Ge/SiGe PQWs and their FTIR optical characterization. This confirms the realization of a parabolic potential and a single, well-defined ISBT absorption peak that is independent of temperature and doping.

- Chapter 4 focuses on the content of the second publication, demonstrating the use of PQWs to illustrate, for the first time, the formation of ISBT polaritons using group IV semiconductor heterostructures. This chapter discusses the integration of PQWs for THz microcavity arrays based on plasmonic ground plane/semiconductor/metal patch antennas and the resulting observation of ultra-strong coupling in the Ge/SiGe system. In the introductory section of the chapter, particular attention is devoted to the optimization of the design and growth of the complete back-mirror structure, based on heavily doped SiGe, which plays a crucial role in enabling efficient confinement and coupling within the microcavity.

- Chapter 5 addresses the optimization of modulation doping in Ge/SiGe PQWs. The impact of epitaxial and thermal strain on charge-transfer efficiency is analyzed, and new approaches are proposed to enhance doping effectiveness and improve device performance.

1

Silicon Germanium Heterostructures and QWs properties

1.1 Properties and Band Structure of Silicon Germanium

In this chapter, I will analyze the fundamental properties of Si and Ge and their alloys. Both materials belong to group IV of the periodic table and have a diamond-like crystal structure, with a face-centered cubic (FCC) Bravais lattice with a 2 base atoms [11], as presented in Figure 1.1a. The lattice parameters of Si and Ge at room temperature are 5.431 Å and 5.658 Å, respectively.

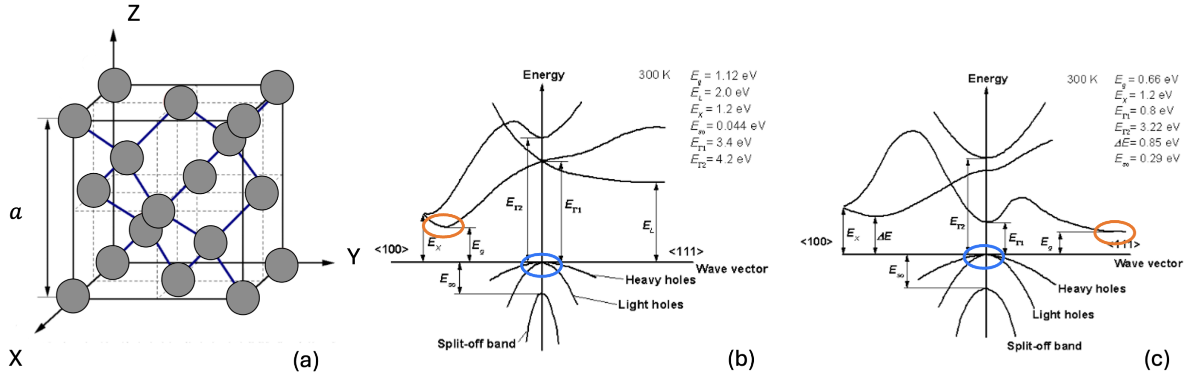

Figure 1.1: *Structural an electronic properties of Si and Ge. (a) FCC crystal structure of Si and Ge. Band structure of Si (b) and Ge (c) at room Temperature (T=300K).*

Figures 1.1b and c show the band structures of silicon and germanium, respectively. Both of them are characterized by an indirect bandgap, where the bottom of the conduction (highlighted with a orange circle) and top of valence bands (blue circle) are located at distinct points within the Brillouin zone. In both cases, the maximum of the valence band is at the Γ point, k=0. In the case of Si, the minimum of the conduction band is 6 times degenerate and occurs at the Δ point along the X direction, parallel to [100] crystallographic direction

[12], as presented in Figure 1.2a. In contrast, Germanium exhibits eight equivalent half ellipsoids located at the L point along the [111] crystallographic direction, see Figure 1.2b. The corresponding indirect gap for this material is 0.66 eV, while the direct gap, at Γ, is 0.8 eV. In this case, the energy difference between the L and Γ valleys is only 0.136 eV, and the difference between the X and Γ valleys is 2.3 eV.

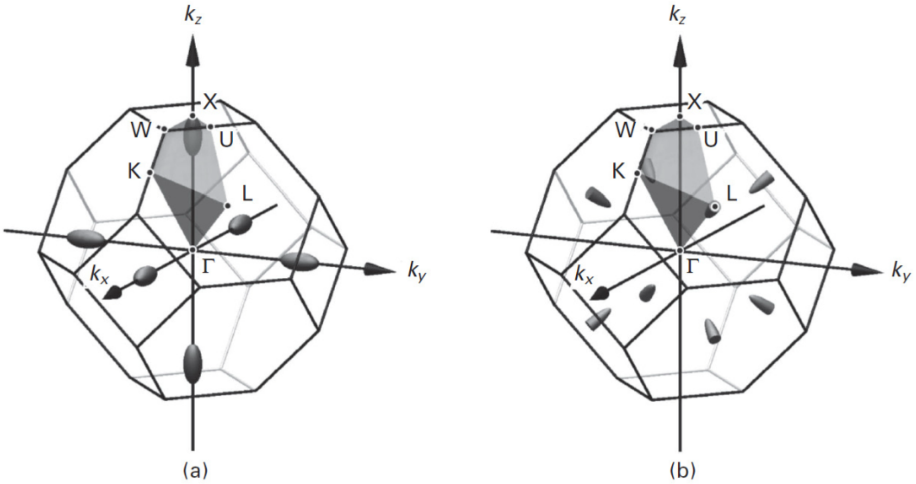

Figure 1.2: *Constant energy surfaces characterizing the conduction band minima of Si (a) and Ge (b) [13].*

The valence band of both materials is given by the atomic orbital p. The spin-orbit interaction splits the states $|P_j, m_j\rangle$ into two levels with total angular momentum $j = 3/2$ (degeneration 4) and $j = 1/2$ (degeneration 2). The states $|3/2, \pm 3/2\rangle$ are called heavy holes (HH), while $|3/2, \pm 1/2\rangle$ are called light holes (LH). The level $|1/2, \pm 1/2\rangle$, known as the split-off band, exists throughout the Brillouin zone; at the Γ point it lies at an energy Δ. In Germanium, the spin-orbit split is larger ($\Delta = 0.29$ eV) than in silicon ($\Delta = 0.044$ eV) due to the greater atomic number of Ge.

We now refer to the conduction band, as it is the relevant one for the analysis developed in this work. In the calculation of electronic properties, it is essential to consider the effective masses of the electrons in Si and Ge. These masses have a tensor form and depend on the confinement direction. In this case, it is important to consider the (001) direction, as it is the growth and confinement direction of the samples studied in this thesis. For silicon, the effective mass along this direction in the band minima at Δ/L is $m^*_{Si} \simeq 0.92m_0$, while for germanium, in the band Δ/L, it is $m^*_{Ge} \simeq 0.13m_0$ [14].

Having established the band structure of Si and Ge, we can now extend this discussion to the case in which both materials are combined. One of the main motivations for creating alloys is to tune bandgaps and lattice constants, thereby obtaining intermediate bandgaps between those of the individual materials and/or lattice parameters that enable epitaxial growth with high crystalline quality. The properties of many alloys can be described as an interpolation between those of the two base materials [15]. For the SiGe alloy, the lattice parameter of the alloy, $a_{Si_{1-x}Ge_x}$, in terms of the Ge concentration, x, is described by the following relationship:

$$a_{Si_{1-x}Ge_x}(x) = (1-x)\,a_{Si} + x a_{Ge} - b^{SiGe}(1-x)\,x, \tag{1.1}$$

where a_{Si} and a_{Ge} are the lattice parameters of Si and Ge, respectively, and $b^{SiGe} = -0.0021$ nm is the bowing parameter.

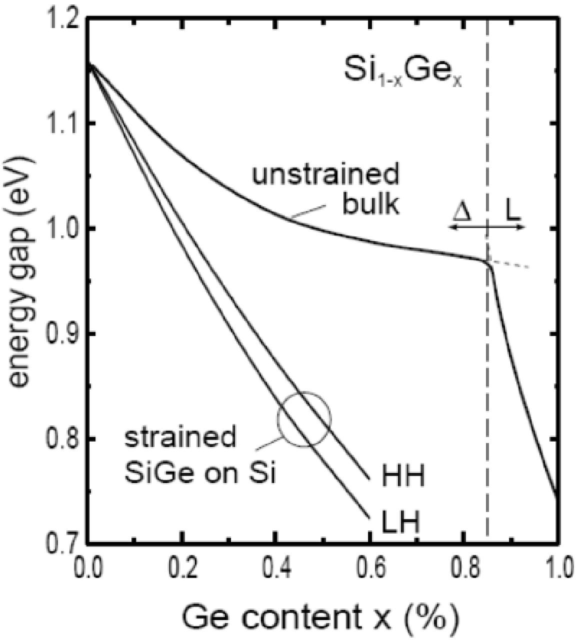

Figure 1.3: *Variation of the energy gap as a function of the Ge concentration in the $Si_{1-x}Ge_x$ alloy. The minimum of the conduction band is at Δ for $x < 0.82$ and at L for $x > 0.82$ [16].*

The SiGe alloy is completely miscible across the entire composition range, which allows its electronic properties to be continuously tuned. In particular, the band structure of $Si_{1-x}Ge_x$ as a function of x changes markedly around $x \sim 0.85$, as shown in Figure 1.3. This is because the conduction band minimum lies at the Δ point for $x < 0.85$, similar to Si, while for $x > 0.85$ the minimum shifts to the L point, as in Ge. These trends apply to a cubic alloy without strain. The concentration dependence of the bandgap energy can be written as [17]:

$$E_g^{\Delta}(x) = 1.155 - 0.430x + 0.206x^2 \; eV \qquad x < 0.85 \tag{1.2}$$

$$E_g^{L}(x) = 2.010 - 1.270x \; eV \qquad x > 0.85 \tag{1.3}$$

This capability to tailor the bandgap and the electronic structure through composition makes SiGe alloys particularly attractive for advanced CMOS technologies and photonic components based on SiGe heterostructures with varying Ge content.

1.2 SiGe heterostructure epitaxial growth

In order to fully exploit the tunable properties of SiGe alloys, it is essential to understand how they are implemented in real devices. This naturally leads us to the epitaxial growth of

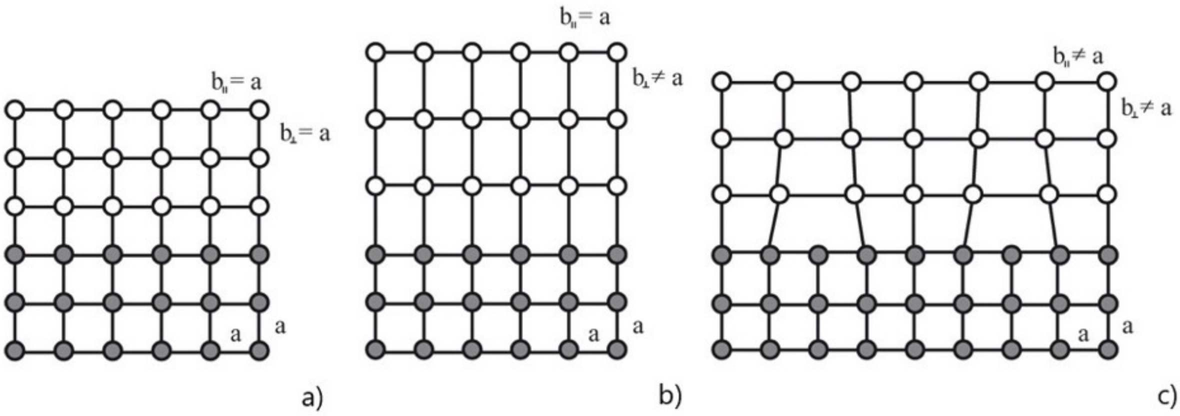

Figure 1.4: *Comparison between lattice matched (a), out-of-plane mismatched (b), and in- and out-of-plane mismatched lattice parameters (c). (b) The film grows consistently with the same parameter in the plane but the elementary cell is deformed with the accumulation of elastic energy. (c) The difference between the in-plane lattice parameter mismatch is compensated by the introduction of crystallographic defects.*

heterostructures, which is the focus of this section. Epitaxial growth consists of the oriented deposition of a material on an oriented substrate. Two parameters play a central role in determining how the film grows on the substrate: the lattice parameter mismatch and the adhesion coefficient.

Figure 1.4 illustrates different scenarios for lattice-matched and lattice-mismatched planar heterostructures. The lattice parameter mismatch between the substrate, a_s, and the epilayer, a_e, is defined as $f = \frac{a_e - a_s}{a_s}$. Panel (a) shows the case $f = 0$, in which the lattice parameters of the substrate and the film are equal. In this situation, the epilayer grows coherently on the substrate without deformation of its lattice. Panels (b) and (c) present the case $f \neq 0$, where a mismatch exists between the materials. The epilayer may still initially grow coherently, accumulating elastic energy associated with the biaxial tetragonal strain imposed by the substrate. However, beyond a critical thickness, the coherent configuration becomes energetically unfavourable: the system may reduce its elastic energy by introducing misfit dislocations, leading to incoherent growth and subsequent plastic relaxation of the strain. These aspects will be discussed in more detail in the following section. Notice, however, that in the presence of a significant lattice mismatch f, three-dimensional growth is thermodynamically favored. The emergence of islands results from the competition between accumulated elastic and surface energies, as the system always evolves toward minimizing its total free energy.

The second important parameter affecting the growth dynamics is the adhesion coefficient, defined as [18]:

$$\sigma = \frac{\gamma_s - \gamma_e}{\gamma_s}, \tag{1.4}$$

where γ_s and γ_e are the surface free energies of the substrate and the epilayer, respectively.

Under thermodynamic equilibrium, the interplay between f and σ leads to three distinct growth modes, according to the Bauer classification, illustrated in Figure 1.5:

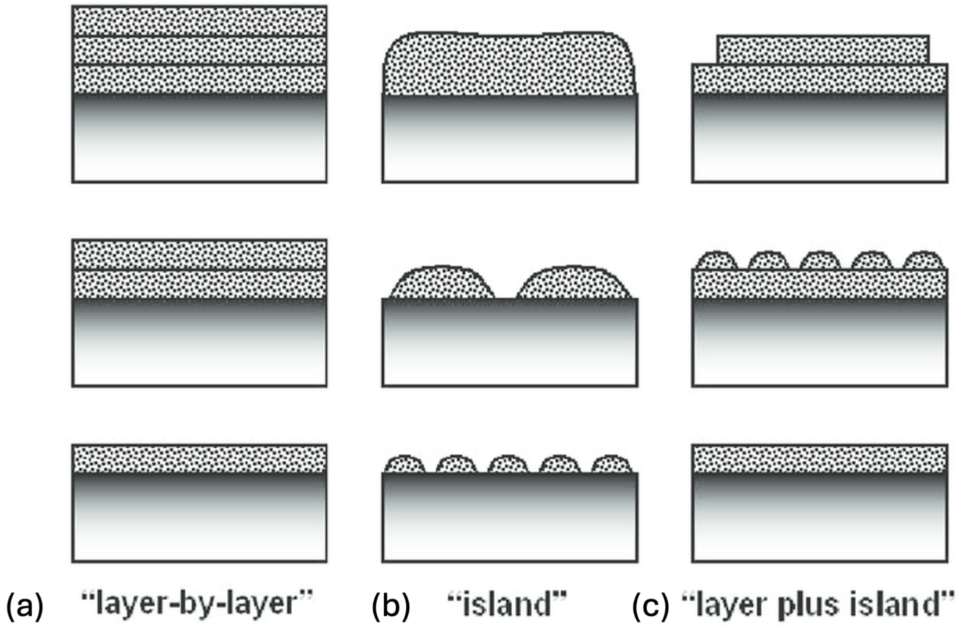

Figure 1.5: *Scheme of the three main epitaxial growth modes: (a) the layer-by-layer growth, Frank-Van der Merwer, (b) Volmer- Weber island growth mode and (c) the mixed Stranski-Kanstanov growth mode.*

- $\sigma > 0$, small f: Growth proceeds layer-by-layer (2D), corresponding to the Frank-Van der Merwe mode. Beyond a critical thickness, h_c, the growth remains planar, but dislocations form within the film.

- $\sigma < 0$: The growth mode is characterized by the formation of three-dimensional islands (Volmer-Weber). These islands subsequently expand laterally until coalescing and covering the surface.

- $\sigma > 0$, large f (typically $> 2\%$): Growth begins layer-by-layer until it surpasses a critical thickness h_c; at this point, the internal stress becomes too large, and three-dimensional islands grow until they merge, a process known as Stranski-Krastanov growth.

In the specific case of Ge/Si heteroepitaxy, the favored growth mechanism is Stranski-Krastanov. However, it has been shown [19] that low-temperature growth, discussed in detail below, can shift to a growth mode toward planar deposition. In this thesis, we optimized the growth conditions to achieve planar heterostructures, as discussed in the following.

1.3 Strain development in SiGe heterostructures

Building on the discussion of epitaxial growth mechanisms, we now examine the development of strain within SiGe heterostructures, a key aspect that governs their structural and electronic behaviour. In order to understand the mechanical response of the material to lattice deformation, it is necessary to formally define the stresses that arise within the system.

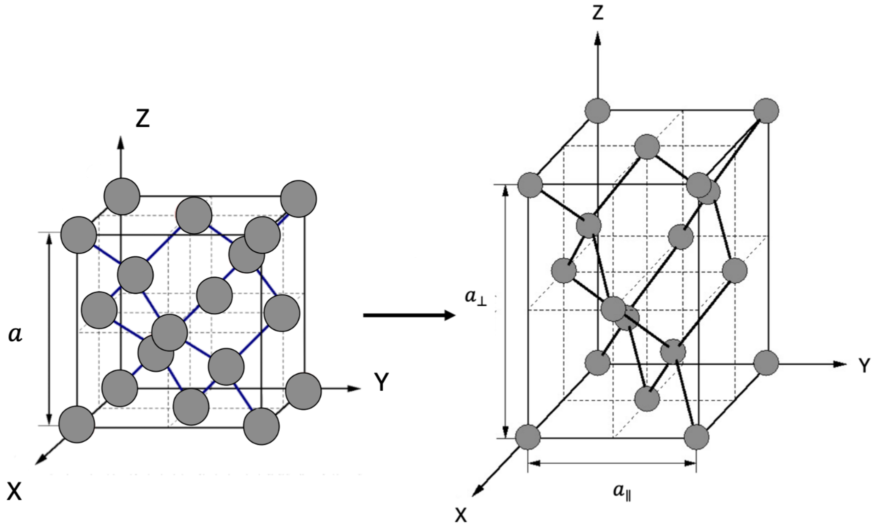

Figure 1.6: *Schematic illustration of the deformation of a diamond-type crystal lattice from a cubic to a tetragonal unit cell upon epitaxial growth on a substrate with a smaller lattice parameter. The in-plane lattice constant is forced to match the substrate, resulting in out-of-plane lattice distortion.*

Internal stress, defined according the Hooke's law, can be expressed in tensor form through the stress tensor σ_{ij}, given by [20]:

$$\sigma_{ij} = C_{ijkl}\varepsilon_{kl}, \tag{1.5}$$

where ε_{kl} is the strain tensor and C_{ijkl} is the stiffness tensor. This relation can be simplified depending on the system symmetry. For materials with cubic symmetry, such as Si and Ge, Eq. 1.5 in Voigt notation:

$$\begin{bmatrix} \sigma_{xx} \\ \sigma_{yy} \\ \sigma_{zz} \\ \sigma_{yz} \\ \sigma_{zx} \\ \sigma_{xy} \end{bmatrix} = \begin{bmatrix} c_{11} & c_{12} & c_{12} & 0 & 0 & 0 \\ c_{12} & c_{11} & c_{12} & 0 & 0 & 0 \\ c_{12} & c_{12} & c_{11} & 0 & 0 & 0 \\ 0 & 0 & 0 & c_{44} & 0 & 0 \\ 0 & 0 & 0 & 0 & c_{44} & 0 \\ 0 & 0 & 0 & 0 & 0 & c_{44} \end{bmatrix} \cdot \begin{bmatrix} \varepsilon_{xx} \\ \varepsilon_{yy} \\ \varepsilon_{zz} \\ \varepsilon_{yz} \\ \varepsilon_{zx} \\ \varepsilon_{xy} \end{bmatrix} \tag{1.6}$$

The elastic constants of Si, Ge and SiGe alloys are reported in table 1.1.

	Si	**Ge**	**$\mathrm{Si}_{1-y}\mathrm{Ge}_y$**
C_{11} (Mbar)	1.68	1.285	$(1-y)C_{11}^{\mathrm{Si}} + yC_{11}^{\mathrm{Ge}}$
C_{12} (Mbar)	0.639	0.483	$(1-y)C_{12}^{\mathrm{Si}} + yC_{12}^{\mathrm{Ge}}$
C_{44} (Mbar)	0.796	0.668	$(1-y)C_{44}^{Si} + yC_{44}^{Ge}$

Table 1.1: *Elastic constants characteristic of Si and Ge.*

When the epilayer is deposited coherently, that is with the same orientation and an in-plane lattice parameter matching that of the substrate, it undergoes an in-plane biaxial strain $\varepsilon_{||}$, defined as:

$$\varepsilon_{\parallel} = \frac{a - a_0}{a_0}, \tag{1.7}$$

where a is the in-plane lattice parameter of the strained epilayer and a_0 is the relaxed lattice parameter of the unstrained material. Under epitaxial growth conditions, as in our case, the unit cell is deformed from cubic to tetragonal, as illustrated in Figure 1.6. Along the out-of-plane direction, the strain is given by:

$$\varepsilon_{\perp} = -\frac{2\nu}{1-\nu}\varepsilon_{\parallel}, \tag{1.8}$$

where ν, the Poisson module, is defined as:

$$\nu = \frac{C_{12}}{C_{11} + C_{12}}. \tag{1.9}$$

The elastic energy U_{strain}, defined as the deformation work per unit volume, can be written as:

$$U_{strain} = [C_{11} + C_{12} - 2\frac{C_{12}^2}{C_{11}}]\varepsilon_{\parallel}^2. \tag{1.10}$$

Integrating over the thickness of the film yields the stored elastic energy per unit area:

$$E_{strain} = [C_{11} + C_{12} - 2\frac{C_{12}^2}{C_{11}}]\varepsilon_{\parallel}^2 h = A\varepsilon_{\parallel}^2 h \tag{1.11}$$

where A is the biaxial modulus and h is the epilayer thickness.

1.3.1 Relaxation mechanism of SiGe heterostructures

To understand how strained layers evolve during epitaxy, it is necessary to examine the mechanisms through which SiGe heterostructures relieve accumulated elastic energy.

The difference in lattice parameters between the substrate and the deposited material introduces internal forces in the crystalline lattice, as the film must locally adapt its atomic arrangement to that of the substrate. As the coherently strained layer grows thicker, the elastic strain energy stored within it increases, as shown in equation 1.11. When this energy exceeds the cost of forming misfit dislocations, plastic relaxation becomes thermodynamically favorable. Consequently, beyond a critical thickness, as shown in Figure 1.7, the system predominantly relieves strain through the nucleation and propagation of misfit dislocations.

Figure 1.7a illustrates the mechanism by which strain relaxation occurs in SiGe/Si(001) heterostructures. This occurs through the formation of misfit dislocations (MDs) and threading dislocations (TDs). MDs are linear defects located at the interface. These dislocations are created through MD-TD semiloops, in which the interfacial MD segment connects to two threading arms. The TDs, predominantly screw-type and thus ineffective in strain relaxation, propagate upward through the epilayer and may eventually reach the surface, where they can degrade the active region of devices grown on such heterostructures.

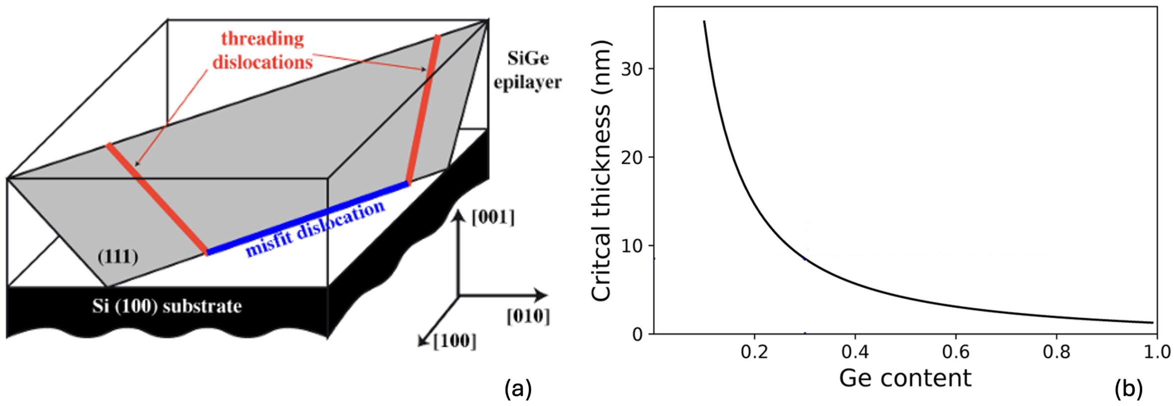

Figure 1.7: *(a) Misfit dislocation (blue line) lying along the crystallographic direction* $\langle 110 \rangle$*, connected to two threading dislocation segments (red lines) lying in the (111) plane. (b) Critical thickness as a function of the Ge concentration, calculated according to the Matthews-Blakeslee model [21].*

It is important to note that for SiGe alloys with a high Ge content ($x_{Ge} > 0.8$) grown on Si(001) substrates, the critical thickness (h_c) reaches values of only a few nanometers. This trend is presented in Figure 1.7b, which shows the rapid decrease of h_c with increasing Ge content. Such limited thicknesses are insufficient for the fabrication of functional device layers, making it essential to adopt specific strategies to ensure high crystalline quality in highly mismatched systems.

To mitigate these challenges and reduce the density of TDs in the active region, several approaches have been developed for the growth of Ge and SiGe heterostructures on Si(001). Among these, the use of virtual substrate (VS) and the deposition of strain-compensated active regions play a central role, as they provide a gradually relaxed template with a controlled lattice parameter. This concept will be discussed later in Section 2.1 in relation to the growth of the materials studied in this thesis.

1.3.2 Influence of temperature on biaxial deformation

In addition to composition and lattice mismatch, temperature also affects the strain state of epitaxial layers. Temperature variations modify the lattice parameter of each material according to their temperature-dependent thermal expansion coefficients, defined as:

$$\alpha\left(T\right) = \frac{1}{a}\frac{\partial a}{\partial T}. \tag{1.12}$$

The temperature dependence of the lattice parameters of Si and Ge is shown in Figure 1.8. This figure highlights that, due to their different thermal expansion behaviors, a temperature change impacts the relative lattice mismatch between the two materials.

As a consequence, when a Ge-rich SiGe heterostructure is deposited on a thick Si substrate, a thermal strain develops when the temperature deviates from the growth temperature, T_G, which can be expressed as [23]:

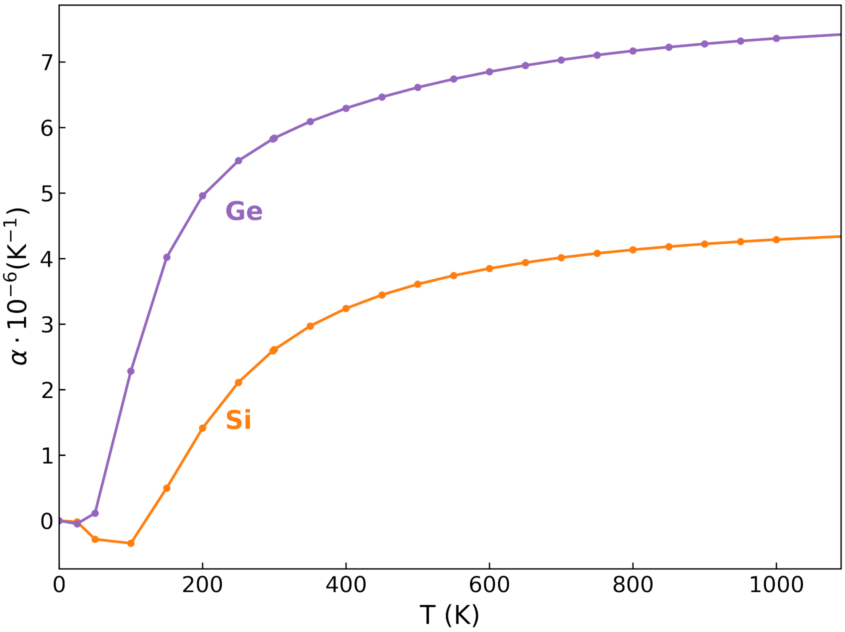

Figure 1.8: *Thermal expansion coefficient of Si and Ge as a function of temperature (K), obtained from experimental data reported in the literature [22].*

$$\varepsilon_{\|}^{therm}(T_G, T) = \int_{T}^{T_G} [\alpha_{Si_{1-y}Ge_y}(T') - \alpha_{Si}(T')]dT' \tag{1.13}$$

This expression is valid for the typical case of a thin film ($\sim 2/3\mu m$) grown on a much thicker substrate ($\sim 500\mu m$). The total in-plane strain is therefore composed of two contributions: the thermal strain and the epitaxial strain, $\varepsilon_{\|}^{epi}$. The resulting total biaxial strain can be written as:

$$\varepsilon_{\|} = \varepsilon_{\|}^{epi} + \varepsilon_{\|}^{therm} \tag{1.14}$$

1.3.3 Band structure strain effect

When a cubic cell is deformed into a tetragonal shape, the total deformation can be decomposed into two contributions: a hydrostatic term, ε_h, and a uniaxial term, ε_s. The hydrostatic component corresponds to the isotropic fractional change in volume, while the uniaxial component modifies the crystal symmetry along the z-axis in the tetragonally distorted cell. Thus, the total strain can be written as:

$$\varepsilon = \varepsilon_h + \varepsilon_s, \tag{1.15}$$

with:

$$\varepsilon_h = \frac{\Delta V}{V} = (2\varepsilon_{||} + \varepsilon_{\perp}), \tag{1.16}$$

$$\varepsilon_s = \varepsilon_{||} + \varepsilon_{\perp} \tag{1.17}$$

Hydrostatic strain produces a rigid shift of the band energies, which affects both the conduction band (CB) and the valence band (VB). These shifts can be written as:

$$\Delta E_c^{av} = a_c \varepsilon_h = a_c(2\varepsilon_{||} + \varepsilon_{\perp}), \tag{1.18}$$

$$\Delta E_v^{av} = a_v \varepsilon_h = a_c(2\varepsilon_{||} + \varepsilon_{\perp}), \tag{1.19}$$

where a_c and a_v are the hydrostatic deformation potentials in the conduction and valence bands, respectively.

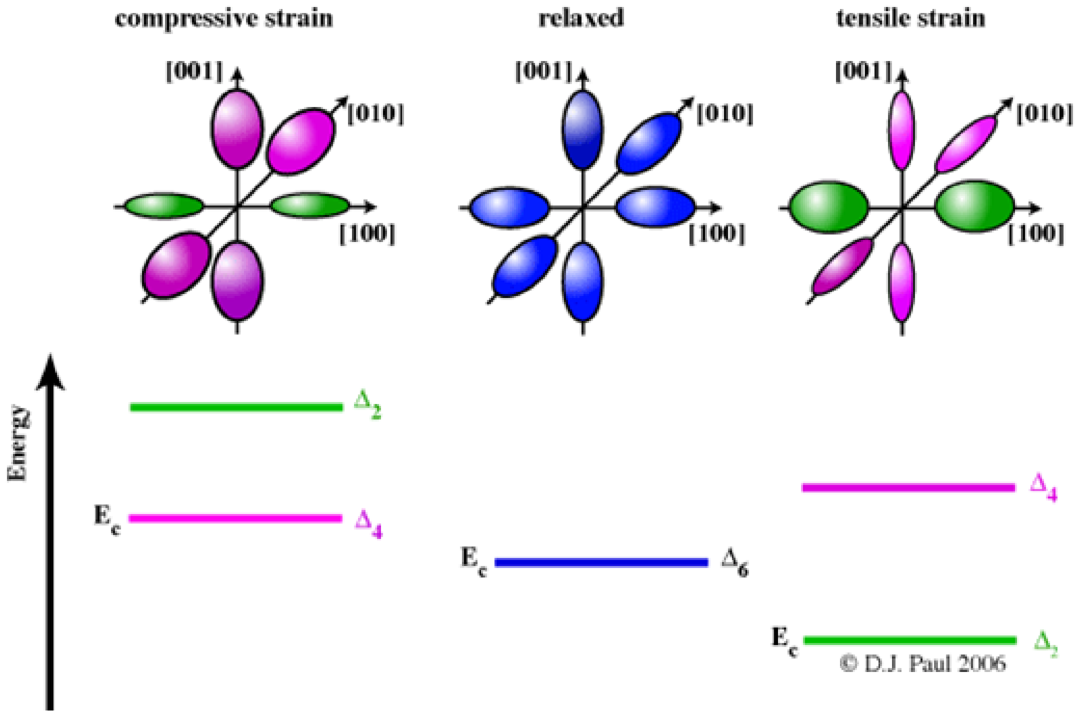

Figure 1.9: *Hydrostatic and uniaxial strain effects on the conduction-band valleys for (100)-oriented substrates. Under compressive strain (left panel), both Δ_2 and Δ_4 valleys lie above the relaxed conduction-band minimum, with Δ_2 at higher energy than Δ_4. Under tensile strain (right panel), Δ_4 lies above the relaxed level while Δ_2 shifts below it [24].*

In the conduction band, the application of uniaxial strain ε_s along the [001] direction partially lifts the sixfold degeneracy of the Δ valleys for Si, as shown in Section 1.1. In the unstrained, all six valleys are degenerate; however, tetragonal distortion splits them into two sets: the Δ_2 valleys oriented along [001], and the Δ_4 valleys lying along [100] and [010]. Under tensile biaxial strain the Δ_2 valleys shift to lower energy compared to the Δ_4 valleys, whereas compressive strain reverses this order.

Figure 1.9 illustrates this behavior by comparing the energy of the Δ valleys in three situations: (a) compressive strain, (b) the unstrained reference case, and (c) tensile strain. The figure highlights how hydrostatic strain shifts both sub-bands together, while uniaxial strain introduces a valley splitting between Δ_2 and Δ_4.

The energy shifts of the two conduction sub-bands are given by:

$$\Delta E_c^{\Delta 2} = \frac{2}{3}\Xi_u^{\Delta}(\varepsilon_{zz} - \varepsilon_{xx}), \tag{1.20}$$

$$\Delta E_c^{\Delta 4} = -\frac{1}{3}\Xi_u^{\Delta}(\varepsilon_{zz} - \varepsilon_{xx}), \tag{1.21}$$

where Ξ_u^{Δ} is the uniaxial deformation potential for the valleys.

For the L bands, which are fourfold degenerated along the [111] directions, strain along [001] causes a slight shift of the valley energy but does not lift their degeneracy.

This strain-induced modification of the electronic structure plays a crucial role in determining the band offsets at heterointerfaces, which we now examine in the following section.

1.4 Band alignment in SiGe heterostructures

A fundamental aspect of modern microelectronics is the ability to engineer band structures, band engineering, meaning the intentional control of the electronic band edges of a material in order to obtain specific electronic or optoelectronic functionalities. This can be achieved through the formation of heterostructures of material having different bandgaps, or through compositional grading and strain engineering. When two SiGe alloys with different Ge concentrations are combined, their mismatch in lattice parameter and bandgap leads to discontinuities in both the conduction and the valence band edges. Such band offsets define potential wells and barriers for electrons and holes. However, the engineering of SiGe heterostructures is particularly challenging because strain significantly modifies the band edges, as detailed in the previous subsections.

Figure 1.10 summarizes the key electronic properties of the $\mathrm{Si}_{1-x}\mathrm{Ge}_x$ active layer coherently grown on a relaxed $\mathrm{Si}_{1-y}\mathrm{Ge}_y$ substrate. In particular, panels (a)-(d) show the fundamental bandgap, valence band offsets, conduction band offsets, and the resulting band-edge profiles as functions of both x and y. In the present work, we focus on n-type SiGe heterostructures and, therefore, consider the conduction-band alignment. Based on the trends presented in this figure, we designed the active region with compositional graded parabolic $\mathrm{Si}_{1-x}\mathrm{Ge}_x$ wells with $x > 0.82$ and $\mathrm{Si}_{0.18}\mathrm{Ge}_{0.82}$ barriers. This choice ensures that the wells provide electrons in the L valley, where the effective mass is smaller, while the conduction-band discontinuity of approximately 110 meV is sufficiently high to produce THz-scale confinement.

In the n-type SiGe/Ge/SiGe structures studied in this thesis, the central Ge-rich layer, with its compositionally graded parabolic profile, defines a parabolic conduction-band edge at the L valley. Within the effective-mass approximation, this conduction-band edge profile $V_0(z)$ serves as the starting point for determining the electronic states in the quantum well, as discussed in Section 1.5. The SiGe barrier layers, with Ge concentration $y < 0.85$, have their conduction-band minimum in the Δ_2 valley. The energy difference between the Δ_2 edge of the barrier and the L edge of the well constitutes the effective conduction-band discontinuity, which is essential for enabling transfer doping and suppressing intervalley $L - \Delta$ scattering of electrons confined in the well. As highlighted by Figure 1.10, this intervalley L-band scattering is strongly strain-dependent through strain vs. composition effects; making accurate control of strain in the barriers a key requirement to achieve the desired optoelectronic properties. [25].

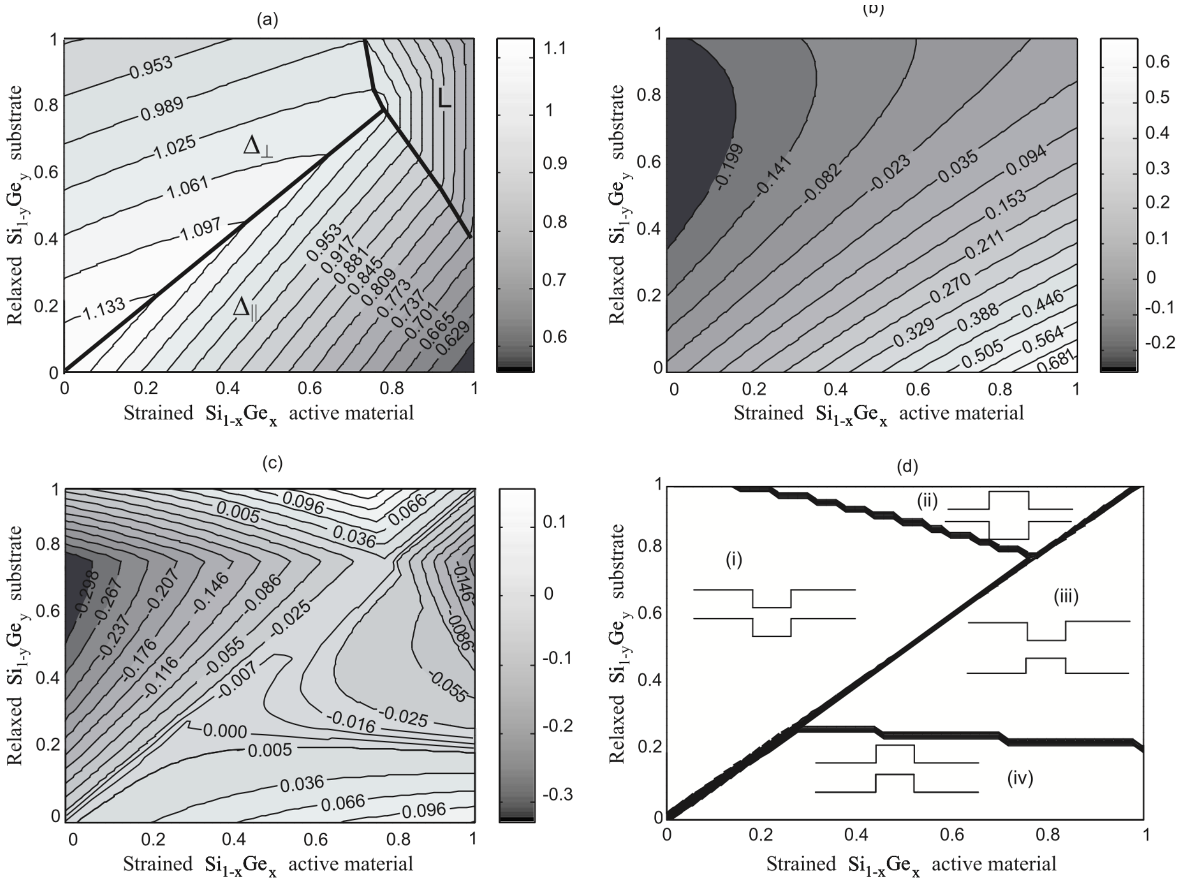

Figure 1.10: *(a) Fundamental bandgap energies; (b) valence band offsets; (c) conduction band offsets and (d) band-edge profiles of* $Si_{1-x}Ge_x$*alloy as a function of the Ge concentration in the strained active material (x axis) and y Ge concentration in the alloy substrate (y axis) which determines the* $a_{\|}$ *lattice constant of the active layer. Energies are in eV [25].*

1.5 Electronic states of SiGe heterostructures in the effective mass approssimation

To determine the electron wave function in a single QW, we start by considering the potential profile $V_0(z)$, where z is the growth direction, as previously discussed in Fig.1.10. In the present case, $V_0(z)$ represents the conduction-band edge associated with the L valley. The electronic states can be calculated within the effective-mass approximation using the envelope-function formalism, which is widely employed in the modeling of semiconductor heterostructures.

Within this approximation, the electron wave function can be expressed as:

$$\varphi(r) \simeq \sum_{k \simeq k_0} c_n(k) e^{ik \cdot r} u_{c,k_0}(r) = u_{c,k_0}(r) \psi(r), \tag{1.22}$$

where k_0 is the wave vector at the minimum of the conduction band; $u_{c,k_0}(r)$ is the lattice-periodic part of the Bloch function, assumed equal in both materials of the heterostructure, $u_A(r) = u_B(r)$; and $\psi(r)$ is the envelope function, which varies slowly over the scale of the lattice constant and carries the information on the confinement within the QW.

The full wave function $\varphi(\mathbf{r})$ satisfies the time-independent Schrödinger equation:

$$\left[-\frac{\hbar^2}{2m^*}\left(\frac{d^2}{dx^2} + \frac{d^2}{dy^2} + \frac{d^2}{dz^2}\right) + V_0(z)\right] \varphi(r) = E\varphi(r), \tag{1.23}$$

where m^* is the effective mass along the z direction. Since electrons are confined only in the z direction but remain free to move in the in-plane directions x and y, the wave function can be separated as:

$$\varphi(r) = \varphi(z)\chi(x,y) = \varphi(z) e^{ik \cdot r_\perp}, \tag{1.24}$$

$r_\perp = (x,y)$ and $k_\perp = (k_x, k_y)$ represent the in-plane coordinates and wave vector, respectively. The system behaves as a free two-dimensional electron gas, and the solution of the Schrödinger equation yields the in-plane kinetic energy: $E_\perp = \frac{\hbar^2 k_\perp^2}{2m^*}$.

Along the growth direction, the envelope function, $\varphi(z)$, satisfies:

$$\left[-\frac{\hbar^2}{2m^*}\frac{d^2}{dz^2} + V(z)\right] \varphi(r) = (E - E_\perp)\varphi(r) = E_n\varphi(r), \tag{1.25}$$

where E_n represents the discrete energy levels with confinement in the QW and depends on the system geometry and the potential $V(z)$.

Thus, the total energy in a two-dimensional system can be written as:

$$E = E_n + \frac{\hbar^2 k_\perp^2}{2m^*}. \tag{1.26}$$

The index n labels the quantized subbands formed along z, while the in-plane wave vector $k_\perp$ varies continuously. The ensemble of electrons occupying these subbands forms a two-dimensional electron gas (2DEG) [17].

1.5.1 Infinite square well

The simplest confinement potential is the infinitely deep square well. In this model, $V(z) = 0$ in the region $-a/2 < z < a/2$, and $V(z) = \infty$ in the barriers. Solving the Schrödinger equation under the condition that the wave function must vanish at the boundaries $\varphi(0) = 0$, the eigenfunctions take the form:

$$\varphi_n = \begin{cases} \sqrt{\frac{a}{2}} \cos\frac{n\pi z}{a}, & n \text{ odd} \\ \sqrt{\frac{a}{2}} \sin\frac{n\pi z}{a}, & n \text{ even} \end{cases} \tag{1.27}$$

and the corresponding eigenenergies are:

$$E_n = \frac{\hbar^2}{2m^*}\left(\frac{n\pi}{a}\right)^2, \quad n = 1, 2, 3, .. \tag{1.28}$$

The parity of the wave functions alternates with n: odd n produces even-parity states, while even n produce odd-parity states [12].

This simple model illustrates how the subband energies can be tuned by adjusting the QW thickness a: narrower wells yield larger energy spacings due to increased confinement.

1.5.2 Finite Square well

Let us consider the case of a QW with a finite potential barrier, $V(z) = V_0$ in the barrier regions. In this situation, all states with $E_n < V_0$ are discrete and correspond to bound states, whereas for $E_n > V_0$, the spectrum becomes continuous. As a consequence, the number of bound states is finite and depends on both the width a and the height V_0 of the well.

We define the QW in the region $-\frac{a}{2} < z < \frac{a}{2}$, with total width a. Inside the well, the eigenfunctions φ_n closely resemble those of the infinite square well (Eq.1.27), especially when the eigenenergies E_n lie well below the barrier height V_0. However, outside the well, the wave function no longer vanishes but instead decays exponentially into the barrier.

Imposing the continuity of φ_n and its derivative at the interfaces, the solution of the Schrödinger equation in the barriers takes the form:

$$\varphi_n = C\begin{cases} Ae^{\xi z}, & z < -\frac{a}{2}, \\ De^{-\xi z}, & z > \frac{a}{2}, \end{cases} \tag{1.29}$$

ξ is the evanescent decay constant.

Solving for the allowed bound-state energies requires matching these functions to the sinusoidal solutions inside the well. This procedure leads to the equations:

$$\begin{cases} \tan\theta = \sqrt{\frac{\theta_0^2}{\theta^2} - 1}, & \text{even eigenfunction,} \\ -\cot\theta = \sqrt{\frac{\theta_0^2}{\theta^2} - 1}, & \text{odd eigenfunction,} \end{cases} \tag{1.30}$$

where the dimensionless parameter

$$\theta_0^2 = \frac{m^* V_0 a^2}{2\hbar^2} \tag{1.31}$$

encapsulates all the physical inputs of the problem, namely the particle effective mass, the well width, and the barrier height. Because the quantization conditions depend only on θ_0, the solution can be obtained graphically, as illustrated in Fig. 1.11.

The graphical construction shows that for any finite well depth V_0 there always exists at least one bound state [12, 17].

This finite-well model provides a more realistic description of semiconductor heterostructures than the infinite-well approximation, since in real materials the

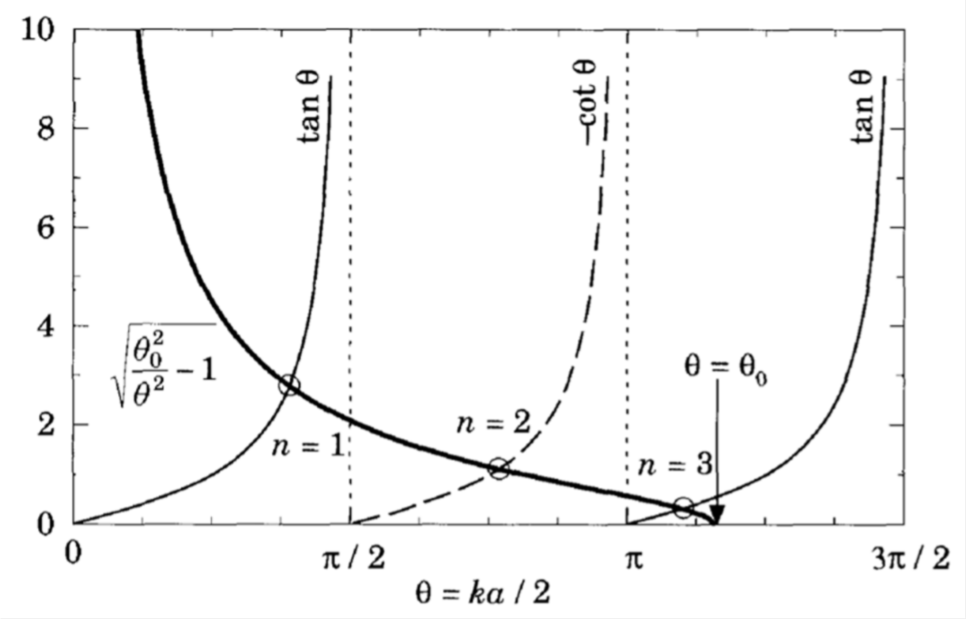

Figure 1.11: *Graphic solution of the equation 1.31.*

conduction-band offset is always finite and wave functions extend into the barrier. These considerations will be essential when discussing parabolic quantum wells (PQWs), where the confinement potential is smooth and position dependent.

1.5.3 Parabolic quantum wells (PQWs)

A particularly interesting case is that of a parabolic confinement potential, in which the energy levels are equidistant. The potential along the growth direction z is given by:

$$V(z) = \frac{1}{2}Kz^2, \tag{1.32}$$

as illustrated in Figure 1.12. Here, K characterizes the curvature of the parabola, which is related to the well depth and width, where $\omega_0 = \sqrt{\frac{K}{m^*}}$ is in accordance with equation 1.34. In this type of potential, the energy levels of the quantized states are given by:

$$E_n = \left(n - \frac{1}{2}\right)\hbar\omega_0 \tag{1.33}$$

where ω_0 is the frequency of the harmonic oscillator:

$$\omega_0 = \sqrt{\frac{8\Delta}{m^*a^2}} \tag{1.34}$$

In these expressions, a is the width, and Δ is the depth of the PQW; m^* is the effective mass of the electron [17, 26].

The energy of the intersubband transitions depends primarily on the depth Δ and the width a of the well; narrower wells produce higher transition energies. In practice, the depth Δ of the well can be tuned by adjusting the Ge content, x, in the $\mathrm{Si}_{1-x}\mathrm{Ge}_x$ barriers. In the

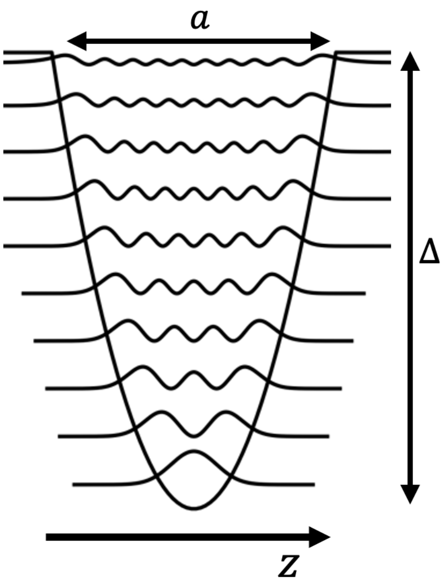

Figure 1.12: *Parabolic confinement potential along the growth direction z. The figure depicts the parabolic potential well characterized by width a and depth Δ, together with the wavefunctions of electrons confined in the well, illustrating the spatial distribution of the bound states along the growth direction.*

PQWs studied in this thesis, the barrier concentration was $x = 0.82$, resulting in a well depth of $\Delta = 112\ meV$.

An additional advantage of PQWs is that, for an ideal parabolic potential, electron-electron interactions cancel out in optical transitions, as predicted by Kohn's theorem. This property makes PQWs excellent candidates for room-temperature optoelectronic applications and for devices operating in the THz range, as we will discuss in more details in the following.

1.5.4 Intersubband transition (ISBT)

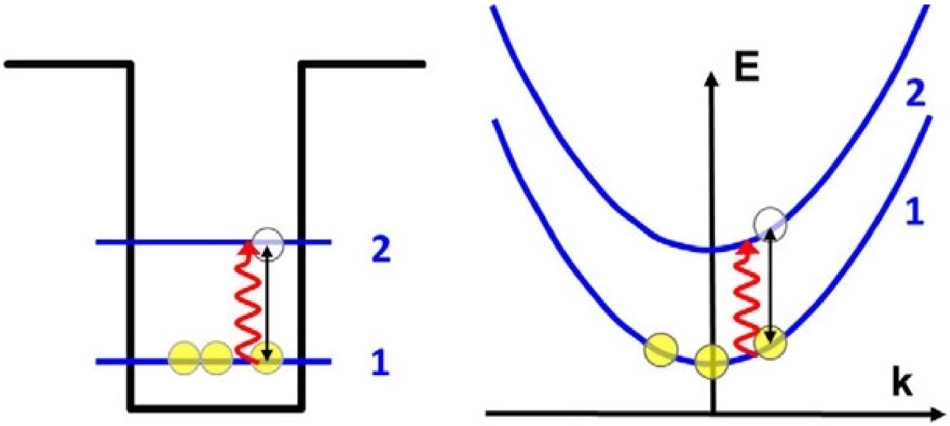

Figure 1.13: *Intersubband transition in a quantum well. In a lightly doped quantum well, the intersubband absorption corresponds to a single-particle transition from the ground subband to the first excited subband, illustrated both in real space (left) and reciprocal space (right). [27]*

The optical properties of QWs arise from the interaction between the electronic system and an incident optical field. Depending on the photon energy, two types of transitions can occur:

- Interband transition (IBT): transitions from an initial state in the valence band (VB) to a final state in the conduction band (CB).
- Intersubband transitions (ISBT): transitions between different subbands within the same band, either CB or VB.

The absorption coefficient for these transitions can be derived starting from Fermi's golden rule, which gives the transition rate W_{if} between an inital state $|i\rangle$ and the final state $|f\rangle$.

$$W_{if} = \frac{2\pi}{\hbar} \left|\langle \varphi_i \left| H' \right| \varphi_f \rangle\right|^2 \delta(E_f - E_i - \hbar\omega) \tag{1.35}$$

where the interaction Hamiltonian is $H' = (\frac{e}{2m})(\mathbf{A} \cdot \mathbf{p} + \mathbf{p} \cdot \mathbf{A})$ and the vector potential $A(q)$ can be expressed as:

$$A = \frac{iE_0 e}{2\omega} e^{i(q \cdot r - \omega t)} + c.c. \tag{1.36}$$

with the corresponding electric field :

$$E = -\partial A / \partial t = E_0 ecos\left(q \cdot r - \omega t\right), \tag{1.37}$$

where e is the polarization vector and q is the propagation vector.

Using the dipole approximation, valid when the radiation wavelength is much larger than the characteristic size of the electronic system, the transition rate becomes:

$$W_{if} = \frac{2\pi}{\hbar} \frac{e^2 E_0^2}{4m^{*2}\omega^2} \left|\langle i | e \cdot p | f \rangle\right|^2 \delta\left(E_f - E_i - \hbar\omega\right). \tag{1.38}$$

Considering the properties of Bloch functions and the extended envelope functions, the matrix element can be rewritten as:

$$\langle i | \, e \cdot p \, | f \rangle = e \cdot \langle u_\nu | \, p \, | u_{\nu'} \rangle \langle f_n | f_{n'} \rangle + e \cdot \langle u_\nu | u_{\nu'} \rangle \langle f_n | \, p \, | f_{n'} \rangle, \tag{1.39}$$

where ν ,ν' and n, n' denote the band and subband indices of the initial and final states. For ISBT within the same band ($\nu = \nu'$), the first term vanishes, and the dipole element reduces to the second term, which involves only the envelope functions:

$$\langle f_{nk_\perp} | \, e \cdot p \, | f_{n'k'_\perp} \rangle = \frac{1}{A} \int d^3 r e^{-ik_\perp \cdot r} \phi_n^*(z) [e_x p_x + e_y p_y + e_z p_z] e^{-ik' \perp \cdot r} \phi_{n'}(z). \tag{1.40}$$

The in-plane components e_x and e_y do not contribute, so the electric field must have a component along z to couple to establishing the polarization selection rule for ISBT: only light polarized along the growth direction can induce these transitions. Integration over the in-plane coordinates imposes the vertical transition condition, $k'_\perp = k_\perp$. Therefore, the one-band dipole matrix element describing the transition probability reduces to:

$$\langle n \left| \left| p_z \right| \right| n' \rangle = \int dz \phi_n^*\left(z\right) p_z \phi_{n'}\left(z\right), \tag{1.41}$$

Since all subbands exhibit the same parabolic energy dispersion in $k_\perp$, as shown in Figure 1.13, all transitions between subbands $n \rightarrow n'$ at different $k_\perp$ values occur at the same energy. Therefore, a Dirac-delta-like absorption would be expected. In reality, however, the ISBT absorption spectrum exhibits a Lorentzian lineshape due to broadening effects associated with the finite lifetime of the excited states. This broadening is described by the parameter Γ, which is determined by the scattering rates that limit the phase coherence of the intersubband transition. The physical mechanisms responsible can be divided into two main contributions. Intrinsic broadening is associated with the material's own processes and carrier density, particularly with electron-phonon interaction and electron-electron scattering. Extrinsic broadening, on the other hand, depends on the structural quality of the sample and is related to scattering from ionized impurities, crystal defects, and interface roughness. These mechanisms set the population relaxation time (T_1) and the dephasing time (T_2), giving rise to homogeneous line broadening. Although well-width fluctuations can introduce an inhomogeneous component, in high-quality samples, or when collisional processes dominate, the line shape is generally well approximated by a Lorentzian [26, 17]. By defining the oscillator strength for the transition between subbands n and n' as:

$$f_{nn'} = \frac{2}{m^* \hbar \omega_{n'n}} \left| \langle n | p_z | n' \rangle \right|^2 = \frac{2m^* \omega_{n'n}}{\hbar} \left| \langle n | p_z | n' \rangle \right|^2 \tag{1.42}$$

the absorption coefficient at $T = 0$ is

$$\alpha_{2D} \left(T = 0 \right) = \frac{n_{2D} e^2 \hbar}{2 \varepsilon_0 c \eta m^*} f_{12} \frac{\Gamma}{\left(E_2 - E_1 - \hbar\omega \right)^2 + \Gamma^2} \tag{1.43}$$

where n_{2D} is the sheet electron density, Γ is the linewidth, ε_0 is the vacuum permittivity, c is the speed of light, η is the refractive index, and E_1, E_2 are the energies of the subbands involved.

1.5.5 Transfer doping and depolarization shift

To induce intersubband transitions (ISBT) in QWs, including PQWs, it is necessary to introduce free electrons into the active region [26]. This can be achieved either through direct doping, in which donor atoms are placed inside the well, or through modulation doping, where donors are inserted into the surrounding barrier layers [17, 10]. As shown in Figure 1.14, in the latter case the electrons occupying the higher-energy donor states in the barrier transfer move to the lower energy well quantized states. Among these two strategies, modulation doping is the approach adopted throughout this thesis.

Before discussing its advantages, it is essential to understand how electron-electron interactions modify the ISB absorption energy through the so-called *depolarization shift*. When an ISBT is driven by an external electromagnetic field, the motion of the electron gas induces an internal restoring field that shifts the resonance energy to higher values. For a single occupied subband, the depolarization-shifted transition energy reads [26]:

$$E_{\mathrm{ISB}} = E_{21} \sqrt{1 + \alpha} \quad with \quad \alpha = \frac{2 e^2 n_{2D}}{\varepsilon \varepsilon_0 E_{21}} S \tag{1.44}$$

where E_{21} is the bare subband spacing, n_{2D} is the sheet electron density, α is a structure-dependent parameter that incorporates the overlap between the initial and final wave functions, and S has the units of length. The shift therefore scales as $\sqrt{n_{2D}}$, and in square QWs it leads to a strong dependence of the absorption energy on doping, particularly at high carrier concentrations. This effect is explicitly included in the numerical model used in this work and represents a crucial aspect of the design of SiGe THz absorbers.

A second collective correction originates from the Hartree potential generated by the spatial separation between electrons and donor ions in modulation-doped structures. In square QWs, this electrostatic contribution modifies the effective confinement, shifting and distorting the subband energies. As a consequence, both the depolarization shift and the Hartree term contribute to a density-dependent shift of the ISB transition energy.

Parabolic quantum wells behave differently. According to Kohn's theorem, for an ideal harmonic potential, the effects of electron-electron interactions, including both the Hartree term and the depolarization shift, cancel exactly in the ISB resonance. As a result, the ISB transition energy remains strictly independent of carrier density and equal to the energy separation of quantized states of the bare harmonic potential. This property holds only if the confinement potential remains purely parabolic. Direct doping inside the well breaks this condition because the Coulomb attraction to donor ions distorts the potential and destroys its harmonicity. In contrast, modulation doping preserves the parabolic profile, ensuring the validity of Kohn's theorem and eliminating the density dependence of the ISB energy.

Figure 1.14 illustrates the effect of transfer doping for a square QW (left) and for a PQW (right). In the square well, the electrostatic potential generated by the donors breaks the symmetry of the confinement and alters the spacing between subbands. In contrast, in the PQW, the parabolic profile is preserved, and the subband levels remain equispaced even after electron transfer from the barrier to the well.

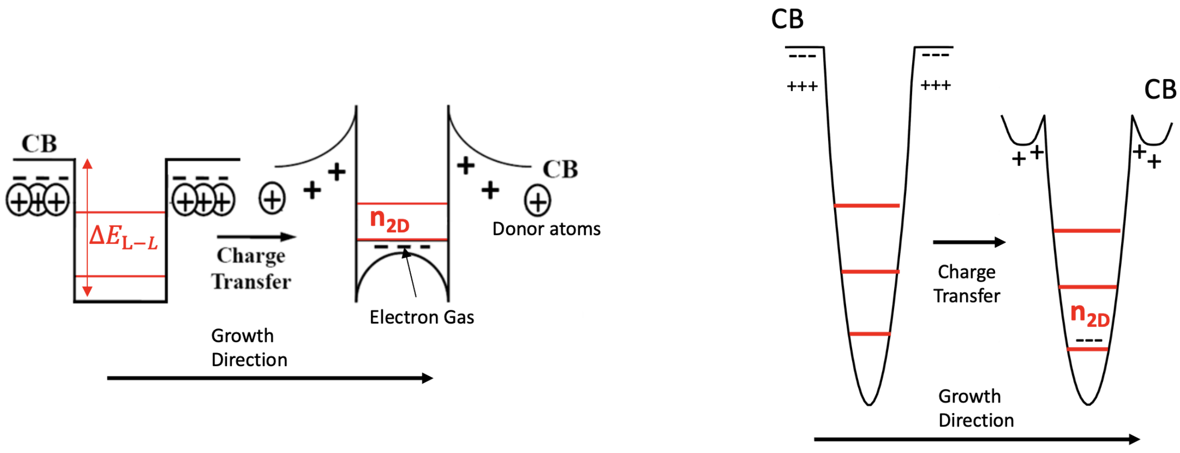

Figure 1.14: *Transfer doping process. Left: square QW, where the Hartree potential distorts the confinement and breaks level equidistance. Right: PQW, where the harmonic confinement is preserved and subband levels remain equally spaced.*

The depolarization shift in square QWs has also an impact on the broadening of ISBT absorption spectra at high temperatures. Notice that in square QWs, the ISB absorption spectrum broadens at high temperatures because electrons thermally populate several subbands, and the corresponding ISBTs occur at slightly different energies. This "spectral broadening" disappears in PQWs modulation-doped, where all intersubband spacings are identical and all transitions contribute at the same energy [10]. Furthermore, the use of modulation doping has the advantage of reducing the homogeneous line broadening because the spatial separation between electrons and donors ions suppress impurity scattering.

For these reasons, modulation-doped PQWs combine a transition energy independent of carrier density, the absence of thermal spectral broadening, and a reduced homogeneous line broadening. This makes them particularly suitable for room-temperature THz intersubband devices, as demonstrated in recent SiGe heterostructures [17, 10, 28].

1.6 Strong radiation-matter coupling effects in MQW heterostructures

The implementation of optical cavities enables the confinement of electromagnetic radiation, enhancing the interaction between light and matter in semiconductor. Under suitable conditions, specifically, when a resonant coupling between the cavity mode and a material excitation becomes sufficiently strong, this leads to the strong coupling (SC) regime. SC occurs when the interaction between a resonant two-level system and a photonic mode confined within an optical resonator exceeds the intrinsic decay rates of the individual components (Figure 1.15a).

In this regime, energy is exchanged coherently and periodically between light and matter, giving rise to new hybrid quasiparticles known as cavity polaritons. Polaritons exhibit a mixed photonic-electronic character and cannot be described as separate entities. They behave as bosons, and the most striking manifestation of SC is the splitting of the degeneracy between the cavity mode and the quantum emitter. In the energy-wave vector dispersion spectrum, this appears as an anticrossing between the cavity photon mode and the quantum matter mode, producing two distinct branches: the upper polariton (UP) and the lower polariton (LP) (Figure 1.15b).

When a two-level quantum system, such as an intersubband transition, interacts coherently with a resonant electromagnetic field, the probability of finding the system in the excited or ground state varies sinusoidally in time. This cyclic phenomenon of absorption and emission is known as Rabi oscillations. The frequency of these oscillations, called the Rabi frequency (Ω_{Rabi}), quantifies the rate of energy exchange between light and matter inside the cavity. The minimum energy separation between the polariton branches, referred to as the *Rabi splitting* , is equal to $2\Omega_{Rabi}$ and provides a direct measure of the light-matter coupling strength defined as the ratio between the Ω_{Rabi}/ω_0, where ω_0 is the quantum emitter frequency. For the

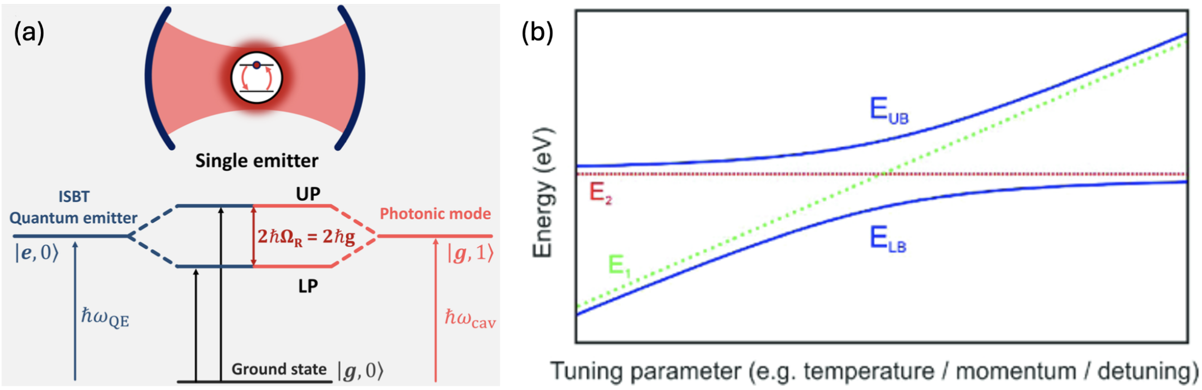

Figure 1.15: *(a) Scheme of the strong-coupling regime between a quantum emitter and a confined photonic cavity. When the energies $\hbar\omega_{QE}$ and $\hbar\omega_{cav}$ are resonant, the coupling g induces an energy splitting $2\hbar\Omega_R$, generating two hybrid states (UP and LP) as coherent superpositions of $|e,0\rangle$ and $|g,1\rangle$. (b) Polariton dispersion as a function of a tuning parameter. The blue curves (E_{UB}, E_{LB}) show the anticrossing and the energy splitting typical of the strong-coupling regime. The green and red curves (E_1, E_2) represent the cavity and the quantum emitter uncoupled energies .*

SC regime to be achieved, the Rabi splitting must exceed both the linewidth of the quantum emitter (γ_{eq}) and the cavity mode (γ_{cav}), ensuring that energy is coherently exchanged between light and matter at a frequency $2\Omega_{Rabi}$ higher than the system's damping rates.

Polaritons can arise in various physical systems depending on the type of excitation or material: exciton-polaritons in direct bandgap semiconductors, phonon-polaritons in polar materials, plasmon-polaritons in metals or doped semiconductors, and intersubband-polaritons in quantum heterostructures. The latter, active in the infrared and terahertz range, emerge when infrared or THz radiation couples to an ISBT between quantized levels in quantum wells. To describe the formation of intersubband polaritons in quantum wells, it is necessary to introduce the theoretical framework that governs their coupling with cavity modes. This framework is presented in the following section.

1.6.1 Intersubband polaritons theoretical principles

The interaction between a quantum emitter, modeled as a two-level system, and a cavity photon can be described using the total Hamiltonian [29]:

$$\hat{H}_{tot} = \hat{H}_{cav} + \hat{H}_{ISB} + \hat{H}_{int}. \tag{1.45}$$

Here, $\hat{H}_{cav}$ represents the photon field confined in the cavity, $\hat{H}_{ISB}$ corresponds to the intersubband transition, and $\hat{H}_{int}$ describes the interaction between light and matter. The two-level system, representing the ISB transition, consists of a ground state $|g\rangle$ and an excited state $|e\rangle$, separated by the transition energy $\hbar\omega_{ISB}$:

$$\hat{H}_{ISB} = \hbar\omega_{ISB}\hat{\sigma}^{\dagger}\hat{\sigma}, \tag{1.46}$$

where $\hat{\sigma} = |g\rangle\langle e|$ and $\hat{\sigma}^\dagger = |e\rangle\langle g|$ are the ladder operators. The transition dipole moment is defined as $\mathbf{d}_{eg} = \langle g|q\hat{\mathbf{r}}|e\rangle$, with q being the electron charge.

Quantization of the photon field leads to the Hamiltonian:

$$\hat{H} = \hbar\omega_{cav}\left(\hat{a}^\dagger\hat{a} + \frac{1}{2}\right), \tag{1.47}$$

where $\hat{a}$ and $\hat{a}^\dagger$ are the photon creation and annihilation operators, respectively. The interaction Hamiltonian, under the electric dipole approximation, can be written as:

$$\hat{H}_{int} = -\hat{\mathbf{d}} \cdot \hat{\mathbf{E}}(\mathbf{r}_d) \tag{1.48}$$

Combining these terms, the total Hamiltonian simplifies to [29]:

$$\hat{H}_{tot} = \hbar\omega_{cav}\hat{a}^\dagger\hat{a} + \hbar\omega_{ISB}\hat{\sigma}^\dagger\hat{\sigma} + \hbar g(\hat{\sigma}\hat{a}^\dagger + \hat{\sigma}^\dagger\hat{a}), \tag{1.49}$$

where the coupling strength is given by

$$g = \sqrt{\frac{e^2 f_{12}}{4\varepsilon\varepsilon_0 m^* V_{mode}}} \tag{1.50}$$

To solve the system, one typically uses the Jaynes-Cummings model [30], which expresses the total Hamiltonian in the basis of uncoupled states $|g, 1\rangle$ for an electron in the ground state with a single photon in the cavity and $|e, 0\rangle$ for the excited state with no photon in the cavity. The total Hamiltonian is reformulated into a matrix representation on this basis:

$$\hat{H}_{tot} = \begin{pmatrix} \hbar\omega_{cav} & \hbar g \\ \hbar g & \hbar\omega_{ISB} \end{pmatrix} \tag{1.51}$$

The state $|\psi\rangle$ of the newly coupled system, resulting from the interaction between light and matter, and the resulting energies can be found using the complete Hamiltonian:

$$\hat{H}_{tot}|\psi\rangle = E|\psi\rangle \Leftrightarrow \begin{pmatrix} \hbar\omega_{cav} - E & \hbar g \\ \hbar g & \hbar\omega_{ISB} - E \end{pmatrix} \begin{pmatrix} \psi_1 \\ \psi_2 \end{pmatrix} = 0. \tag{1.52}$$

Non-trivial solutions for the components ψ_1 and ψ_2 exist only when the determinant of the coefficients equals zero.

$$\begin{vmatrix} \hbar\omega_{cav} - E & \hbar g \\ \hbar g & \hbar\omega_{ISB} - E \end{vmatrix} = 0 \Leftrightarrow E^2 - (\hbar\omega_{cav} + \hbar\omega_{ISB}) - \hbar^2 g^2 = 0 \tag{1.53}$$

This procedure yields the polariton eigenstates and their corresponding energies:

$$E_{UP/LP} = \frac{\hbar\omega_{cav} + \hbar\omega_{ISB}}{2} \pm \frac{\sqrt{(\hbar\omega_{cav} + \hbar\omega_{ISB})^2 + (2\hbar g)^2}}{2} \tag{1.54}$$

As shown in Figure 1.15b, at resonance ($E_{cav} = E_{ISB} = E_0$), an anticrossing behavior is observed. Here, the upper and lower polariton energies are separated by the Rabi splitting, which is determined by the coupling terms under the square root in the previous relation:

$$E_{UP} = E_0 + \hbar\Omega_{Rabi} \tag{1.55}$$

$$E_{LP} = E_0 - \hbar\Omega_{Rabi} \tag{1.56}$$

As already pointed out, splitting provides a direct measure of the light-matter coupling strength and marks the formation of intersubband polaritons, which are hybrid quasiparticles resulting from the coherent interaction of cavity photons and ISB transitions in quantum wells.

One key advantage of intersubband transitions in quantum wells is that these structures can be heavily doped, allowing a large number N of electrons to couple coherently to the same resonant electromagnetic mode. In quantum wells, the subbands are parallel, so the vertical transitions in $k_\perp$ between different subband states all occur at the same energy. This means that all N electrons behave as quantum emitters at the same energy, resulting in a collective enhancement of the light-matter coupling. Consequently, the Rabi frequency scales with the square root of the carrier sheet density n_{2D}. Let us consider a typical double-metal cavity consisting of square patches of area A, as shown in Figure 1.16. The two metal layers encapsulate a stack of N_{QW} identical, doped quantum wells, each with a period P (barrier+well). The cavity volume is therefore $V_{cav} = L_{cav} \cdot A = N_{QW} \cdot P \cdot A$, and the total number of electrons participating in the coupling is $N = n_{2D} \cdot A \cdot N_{QW}$.

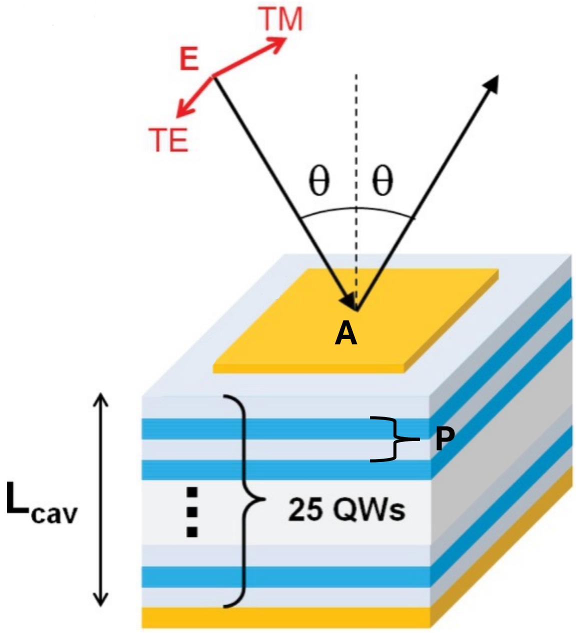

Figure 1.16: *Sketch of a single metal-metal patch cavity with a thickness of L_{cav}, incorporating 25 Ge/SiGe quantum wells e P is the period of QW [31].*

Using the expression for the single-electron coupling strength (Equation 1.50), the Rabi splitting between the polaritonic branches is [32, 33]:

$$E_{up-down} = 2\hbar\Omega_R = \hbar\sqrt{\frac{e^2 f N_{QW} n_{2D}}{\epsilon\epsilon_0 m_z^* L_{cav}}} = \hbar\sqrt{\frac{e^2 f n_{2D}}{\epsilon\epsilon_0 m_z^* PA}}.$$

where f is the oscillator strength of the transition. This relation shows explicitly that Ω_R scales with $\sqrt{n_{2D}}$, which is a crucial factor for reaching the ultrastrong coupling regime, defined by $\Omega_R/\omega_0 > 0.1$. By optimizing charge transfer and maximizing the number of electrons effectively coupled to the cavity mode, the performance of devices exploiting intersubband polaritons can be significantly enhanced. The understanding and engineering of the SC and USC regimes play a crucial role in the development of advanced optoelectronic devices, such as low-threshold lasers based on stimulated final state diffusion, high-speed optical modulators, and high-performance infrared detectors [34, 28]. The USC regime has also been successfully achieved at temperatures close to room temperature, particularly using PQWs, which overcome the intrinsic limitations of traditional square QWs, where the transition energy ω_0 increases with n_{2D} due to the depolarization shift, leading to a reduction of the ratio Ω_{Rabi}/ω_0. Moreover, in square QWs the confined states are not equally spaced, causing different intersubband transition energies for electrons occupying different subbands. As a consequence, the coupling shows a strong dependence on the carrier distribution and, therefore, on temperature, which is particularly limiting for THz-frequency ISB transitions.

The first experimental observation of Rabi splitting was reported by Dini et al. [35] in 2003 in planar microcavities, revealing a splitting of about 14 meV from 10 K up to room temperature using a resonator based on total internal reflection. Later, between 2009 and 2012, Todorov and collaborators [36, 37, 31] investigated ISB polaritons in subwavelength metal-dielectric microcavities operating in the THz range. They addressed the role of the depolarization shift in heavily doped QWs by introducing a dipole-gauge model that explicitly incorporates this contribution. This framework allowed accurate reproduction of experimental results and predicted the existence of a polaritonic gap, a hallmark of the USC regime.

In 2012, Delteil et al. [38] demonstrated charge-induced coherence between intersubband plasmons in highly doped QWs, showing that the optical absorption concentrates into a single narrow resonance. They achieved USC up to room temperature, with a Rabi to transition frequency ratio of 0.33. However, further enhancement of the coupling strength was hindered by the depolarization-induced blue shift of the ISB transitions.

To overcome these limitations, Geiser et al. [39, 6] employed parabolic quantum wells, in which all intersubband transitions share the same energy. In such systems, electron-electron interactions, including the depolarization shift, cancel out exactly, rendering the transition energy independent of temperature and carrier density. Their experiments demonstrated USC in modulation-doped PQWs coupled to LC resonators, achieving a Rabi ratio of 27% and a pronounced polaritonic gap. These results established PQWs as an ideal platform for exploring the USC regime.

More recently, between 2020 and 2023, Deimert, Goulain and co-workers [8, 40] realized arrays of semiconductor harmonic oscillators based on continuously graded PQWs. Their devices exhibited robust performance around 3 THz up to room temperature, with narrow linewidths and resonance frequencies insensitive to temperature and doping, in agreement with Kohn's theorem. They further demonstrated ISB polariton formation at frequencies as low as 1.8 THz, with Q-factors up to 17, maintaining USC up to 200 K and achieving strong/ultra-strong coupling with as few as $\sim$3000 electrons per sub-wavelength LC resonator. Notably, all these achievements were obtained using III-V quantum wells.

As previously mentioned, the main objective of this PhD thesis is to demonstrate and optimize ISB polaritons in the Ge/SiGe material system, extending these advances to group-IV semiconductors.

2

EXPERIMENTAL AND THEORETICAL METHODS

2.1 Chemical vapor deposition (CVD) growth process

The heterostructures investigated in this thesis have been grown in a Chemical Vapor Deposition (CVD) chamber, in an ultra-high vacuum (UHV) system with base pressures in the order of 10^{-10} Torr, to minimize the presence of contaminants such as carbon and oxygen. It is very important to examine the dynamics of the mechanisms that regulate CVD growth. In this technique, the deposited species are called reagent species and are incorporated into a gaseous precursor, which is transported to the surface of the substrate, kept at a temperature T. The precursor gasses used to deposit Si and Ge are, respectively, silane (SiH_4) and germane (GeH_4). The growth process is thermally activated and is divided into the following phases [41], as shown in Figure 2.1.

Considering C_g as the concentration of species S in the gas mixture sent towards the substrate; C_s the concentration of S at the surface; C_f the concentration of S within the grown film; h_g the mass transport coefficients in the gas phase and k_s the reaction rate at the surface, we can express the flow of the precursor gas reagent towards the surface, Φ_{gs} and the flow from the surface to the film (incorporation), Φ_{sf}, as:

$$\Phi_{gs} = h_g \left(C_g - C_s \right) \tag{2.1}$$

$$\Phi_{sf} = k_s C_s \tag{2.2}$$

In stationary conditions, the two flows are the same, therefore:

$$\Phi_{gs} = \Phi_{sf} = \Phi \tag{2.3}$$

$$h_g \left(C_g - C_s \right) = k_s C_s \tag{2.4}$$

The growth rate of the crystal can be determined by dividing the flow, Φ, in steady conditions by the number of atoms incorporated in a unit of film volume:

$$v = \frac{\Phi}{C_f} = \frac{k_s h_g}{k_s + h_g} \frac{C_g}{C_f} = \frac{k_s h_g}{k_s + h_g} \frac{C_t y}{C_f} \tag{2.5}$$

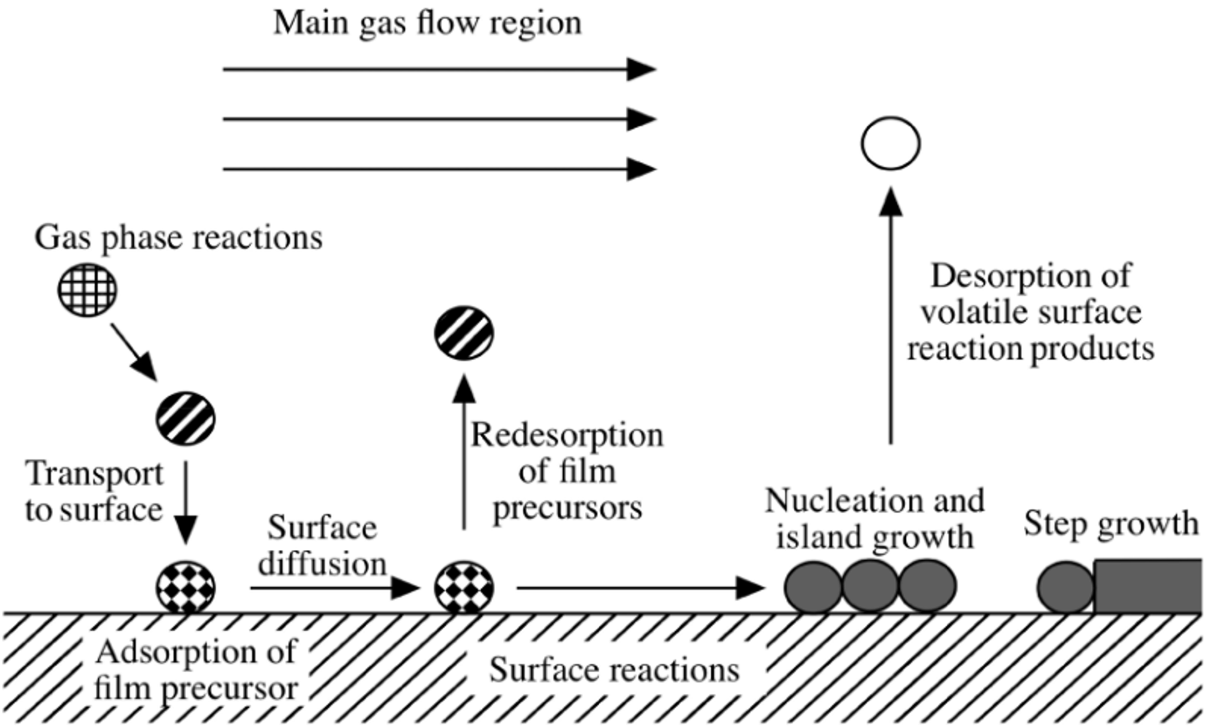

Figure 2.1: *Sketch of gas transport and reaction process for CVD growth. The diagram highlights the main stages involved: gas-phase reactions, transport of the precursors to the surface, adsorption, surface diffusion, desorption of volatile products, and nucleation.*

where y represents the molar fraction of the reagent species, and C_t is the total number of molecules per cm^3 in the gas. Once the molar fractions of the reagents are fixed, the process rate v is determined by the slower process between the mass transport and the surface reaction velocity. Chemical reactions on the surface are greatly influenced by temperature, as opposed to mass transport. At low temperatures, the deposition process is less efficient. This is due to the poor efficiency of the surface reactions: few molecules decompose, leaving few atoms available for the growth of the film. We are in the case of a kinetic regime. The speed of the process will be given:

$$v \sim k_s \left(\frac{C_t}{C_f} \right) y, \quad \text{for } k_s \ll h_g \tag{2.6}$$

When the temperature increases, the surface reactions become more efficient and the process becomes limited by the transport of matter to the surface itself; this is the diffusion regime, described by the equation:

$$v \sim h_g \left(\frac{C_t}{C_f} \right) y, \quad \text{for } h_g \ll k_s \tag{2.7}$$

The temperature at which the transition between these two regimes takes place depends on the type of precursor and the reagent streams used. Figure 2.2a presents the growth rate of a silicon film in terms of temperature for different reagent, including the presence of SiH_4 in some processes. Figure 2.2b shows the growth rate of germanium using the gas GeH_4 as a precursor. Both growth rates present two regimes: ″A″ at low temperatures and ″B″ at high-temperature.

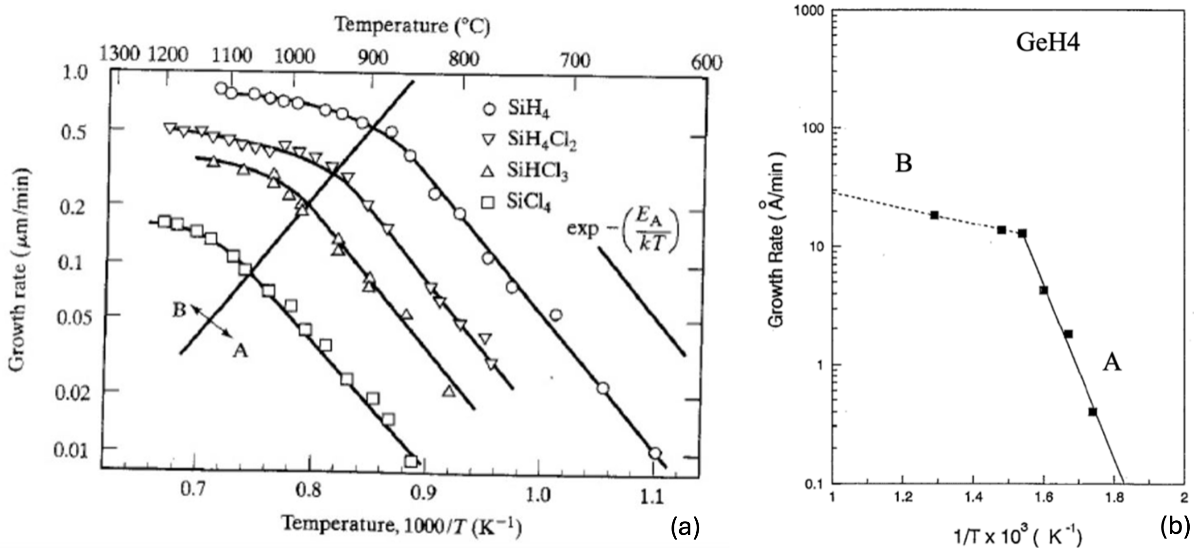

Figure 2.2: *Growth rate as a function of temperature for different gases including Silane (a) and (b) for Germane. The minimum growth rate of silane (SiH_4) occurs at a temperature of $\sim 500°C$, while for germane (GeH_4) it occurs at $\sim 300°C$.*

In the ″A″ region the rate of growth follows an exponential law of the type $v \propto e^{(-Ea/kT)}$, where the growth of the film can be controlled by manipulating the temperature and managing the surface reactions. In the high-temperature ″B″ region, the growth rate is mainly limited by the transport of matter and is therefore relatively independent of temperature. The chemical reactions that outline the growth process of Si, Ge and SiGe films, through the use of silane or germane as precursors, are:

$$SiH_{4(g)} + \mathrm{GeH}_{4(g)} \rightarrow Si_{(s)} + Ge_{(s)} + 4H_2 \tag{2.8}$$

Where (g) and (s) indicate the gaseous state and the solid state, respectively. As already anticipated, the difference in the lattice mismatch between Si and Ge is 4.2%, involving a significant challenge for the realization of heterostructures.

The heterostructures analyzed in this thesis consist of $\mathrm{Si}_{1-x}\mathrm{Ge}_x$ wells with x varying in the range of 0.82 to 1, and with $\mathrm{Si}_{0.18}\mathrm{Ge}_{0.82}$ barriers on germanium substrates on Si(001). At these concentration values, the critical thickness is extremely reduced, on the order of a few nanometers, making epitaxial growth particularly complex without the occurrence of dislocations.

To overcome this structural limit, a $\mathrm{Si}_{1-y}\mathrm{Ge}_y$ VS with a y Ge concentration equal to the average Ge content y_{eq} in the active region must be developed to obtain strain compensation conditions.

Figure 2.3 shows a schematic representation of the different regions of the sample: zone **A**, corresponding to the barrier, and zone **B**, corresponding to the well. In these regions, elastic

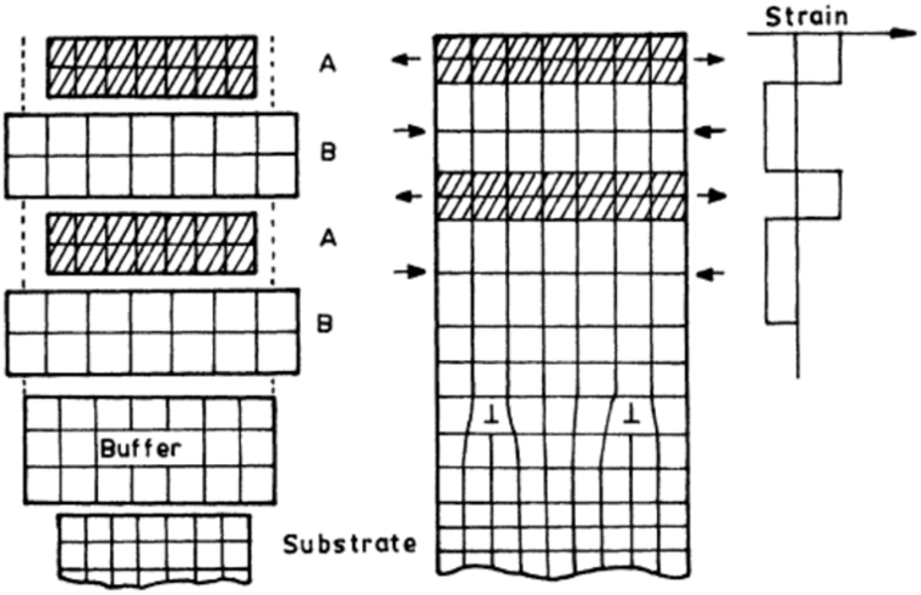

Figure 2.3: *Strain-compensated heterostructure scheme consisting of a compressively strained Ge quantum well (B), confined between tensile-strained SiGe barriers (A), grown on a substrate with an intermediate buffer. The alternation of compressive (Ge) and tensile (SiGe) strain enables lattice strain compensation, reducing stress build-up and preserving crystalline quality. The strain profile shown on the right highlights the oscillation between compression and tension, which ensures mechanical stability.*

deformation manifests as tensile strain in zone A and as *compressive strain* in zone B. For the doped samples, phosphine (PH_3) is utilized as the precursor gas and is introduced within the barrier regions.

The techniques usually used to grow the VS are the Forward Graded technique and the Reverse Graded technique. In the first case, the Ge content in the alloy is gradually increased, starting from the Si substrate until reaching the concentration $y = x_{average}$. The problem is that for high concentrations of y, very thick VS up to 15 μm would be obtained, making it ideal for Ge contents smaller than 50%. These high thicknesses result in the formation of a large number of dislocations, with a consequent increase in surface roughness, requiring chemical and mechanical smoothing of the surface [42]. The second method is a reverse graded approach, starting from the deposition of a Ge buffer on Si(001) and gradually arriving at the desired y. This technique is ideal for VS at high concentrations of Ge, as in the case of this thesis.

Another fundamental aspect is the growth temperature of heterostructures and the high-quality crystalline structure at the interface. To obtain high-quality interfaces and high crystalline quality, typical growth temperatures on the order of 500°C are used. However, when the samples are cooled to room temperature, a tensile thermal strain is established in the Ge rich epilayer region as a consequence of the thermal coefficient mismatch between the Si substrate and the epilayer.

2.1.1 Roma Tre CVD experimental set up

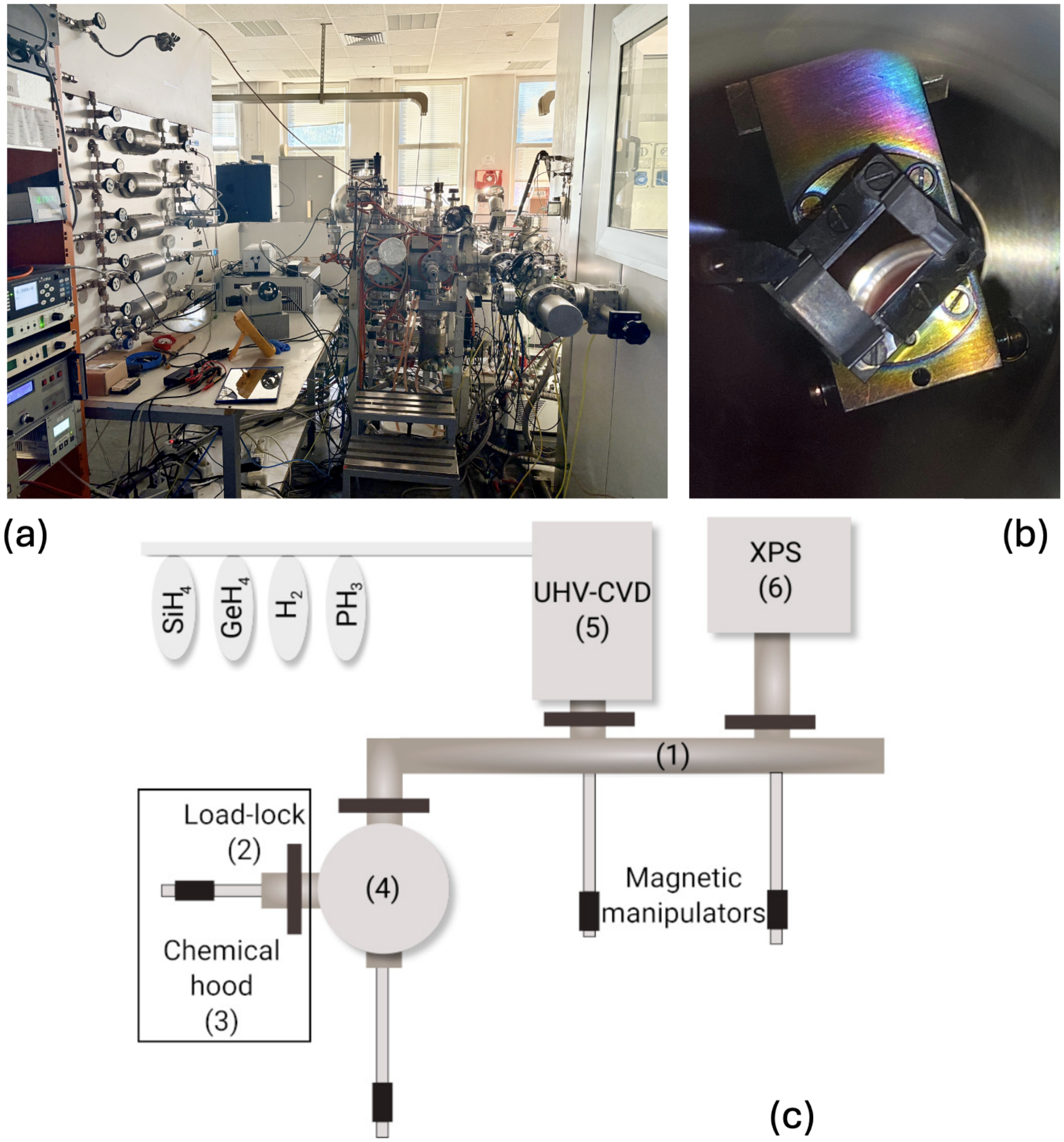

Figure 2.4: *On the left, CVD-UHV present at the Semiconductor Physics and Technology Laboratory of RomaTre. On the right, image of the sample holder used for growth. Sketch of the growth set-up shown below. The system consists of: (1) the main transfer pipe, (2) the load-lock chamber, (3) the chemical preparation hood, (4) the preparation chamber, (5) the UHV-CVD growth chamber, and (6) the XPS chamber. Magnetic manipulators allow sample transfer throughout the interconnected modules.*

At the Laboratory of Physics and Technology of Semiconductor of Roma Tre University, there is an Ultra-high Vacuum Chemical Vapor Deposition (UHV-CVD) system, introduced in the previous paragraph, which is used to grow the samples of this thesis, whose sketch is shown in Figure 2.4a. The samples are prepared inside a laminar flow hood, in a dust-free chamber, where they are cleaned with ultrasound and isopropanol for approximately three hours. After thorough cleaning, the sample is mounted on the sample holder shown in Figure 2.4 right, which is inserted into the first pre-chamber (load-lock) with an internal pressure reaching 10^{-7} Torr, thanks to a rotary pump and a turbomolecular pump. From here, the sample is moved to a second pre-chamber with a pressure of 10^{-9} Torr, where it is heated overnight with a current of 0.2 A to desorb impurities present on the surface. From here, the sample is moved into the chamber through a tube with a pressure of 10^{-9} Torr and transfer arms controlled by a system of external magnetic manipulators. The epitaxial growth chamber is made of a cylindrical body of low-carbon steel and nickel. This chamber is equipped with an external water cooling system, which helps reduce the desorption of adsorbed impurities during the process on the inner walls during the deposition phases. The evacuation system of the chamber consists of a rotary pump and a dual-stage turbomolecular pump, enabling the achievement of residual vacuum pressures on the order of 10^{-10} Torr. Achieving such extremely low pressures is essential to prevent substrate contamination and ensure the growth of high-quality materials. The pressure inside the chamber is measured using a thermionic head for ultra high vacuum regimes and a capacitive vacuum gauge for low vacuum regimes. The chamber is equipped with two external accesses; the first is intended for the introduction of samples into the transfer tube; the second, managed by electropneumatic valves, accommodates the gas transport lines coming from the tanks, equipped with flow meters for regulating the gas flow. A rotary pump and a turbomolecular pump evacuate the section of the line preceding the entry of the reactive gases into the chamber. A computerized control system equipped with control software in the graphical language "G" (LabView) manages the input flows of the different gasses and the switching of the electrovalves to adjust the gas mixture used for the deposition of the various layers in a multilayer heterostructure and the pressure in the chamber, allowing the growth of those layers. The sample holder is connected to a pin that heats the substrate via the Joule effect by passing an electric current from the pin to the opposite end of the substrate, which is in electrical contact with the system's mass. The desired temperature is controlled by an optical pyrometer through transparent windows that maintain the ultra-high vacuum.

2.2 Atomic force microscopy (AFM)

Atomic force microscopy (AFM) is a non-destructive technique capable of providing information about the sample's morphology. Normally, it does not require sample preparation processes and can be used both in air and in liquid.

In AFM, a cantilever carries a sharp tip at its free end, and this tip is moved across the sample by a piezoelectric scanner that enables positioning with sub-nanometer precision. When the tip interacts with the surface, it causes a deflection of the cantilever on which a laser is pointed. The reflected beam is collected by a position sensitive photodetector, allowing the three-dimensional morphology of the sample's surface to be reconstructed. A feedback system acts on the piezoelectric actuators that move the tip, maintaining either a constant interaction force with the surface in contact mode or a constant oscillation amplitude in non-contact mode. This allows the sample's surface morphology to be reproduced with high precision.

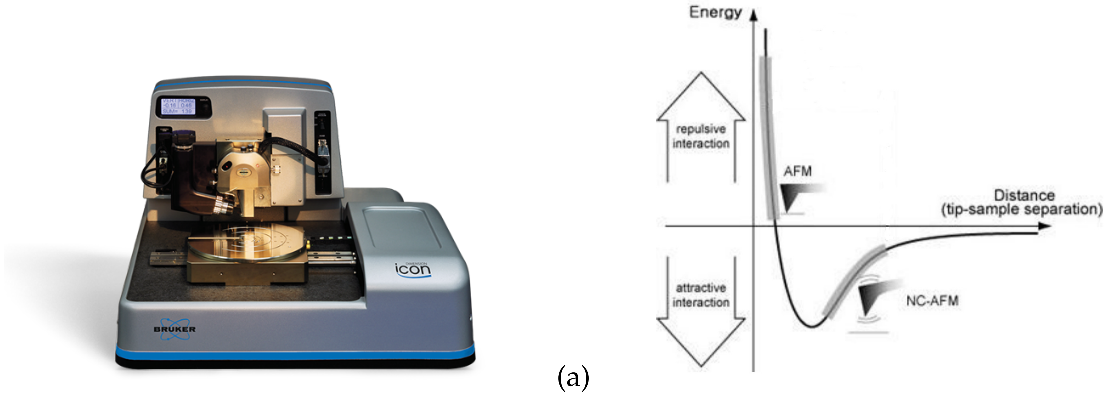

(a) (b)

Figure 2.5: *a) Atomic force microscope available at the LIME laboratories of Roma Tre and at IHP microelectronics, used in this thesis [43]. b) Force exerted between tip and sample as a function of distance for the various modes of the AFM.*

The tip-sample interactions depend on the repulsive forces between the atomic nuclei and the attractive forces between the valence electrons of one and the nuclei of the other (Van der Waals forces). If the distance between the tip and the sample is very small, the repulsive force predominates. When the AFM operates in contact mode, changes in the sample height cause variations in the cantilever deflection and the reflection angle of the laser reaching the detector, which in turn triggers the piezoelectric actuator to restore the correct tip-sample force condition (Figure 2.5b AFM mode).

When the tip is still at a certain distance from the surface, attractive van der Waals forces dominate, producing a small cantilever deflection that is detected via the change in the laser reflection angle. This operating regime corresponds to the non-contact mode (Figure 2.5b NC-AFM mode). To obtain high spatial resolution, the cantilever is driven to oscillate at (or near) its resonance frequency, and the tip-sample interaction induces changes in the amplitude and phase of the oscillation. If the cantilever is driven at its resonance frequency as in non-contact mode but its oscillation amplitude is large enough for the tip to intermittently touch the surface, the system operates in intermittent-contact (tapping) mode. In this regime, strong adhesive and capillary forces can also contribute to the tip-sample interaction.

In this thesis, a Bruker AFM in intermittent mode is used with a high-resolution non-contact cantilever, operating at approximately 300 kHz with different tips that have a nominal curvature radius of between 2 and 8 nm.

2.3 X-ray diffraction (XRD)

X-ray diffraction (XRD) is an essential non-destructive analysis technique for the study of the crystallographic structure of materials, since it allows the structural characteristics to be correlated with chemical-physical properties. The phenomenon of diffraction is based on the elastic scattering of X-rays by the periodic distribution of electrons in the crystal [44]. The condition for constructive interference is satisfied when the scattering vector $Q = K - K_0$, where K and K_0 represent, respectively, the wave vectors of the diffuse and the incident beam, coincides with a vector of the reciprocal lattice H_{hkl}. This condition is equivalent to Bragg's law:

$$n\lambda = 2d_{hkl}\sin\theta, \tag{2.9}$$

where n is the diffraction order, h, k, l are the Miller indices of the crystalline planes, θ is the diffraction angle defined as the angle between the incident beam and the diffracting planes, as shown in Fig. 2.6b-c, d_{hkl} is the interplanar distance, and λ is the wavelength of the incident radiation.

In the context of epitaxial films and heterostructures, high-resolution X-ray diffraction (HRXRD) plays an essential role in the accurate determination of structural parameters, such as strain, the relaxation of the lattice, and the stoichiometry of a binary alloy. Measurements can be performed either by laboratory diffractometers equipped with a thermionic or field-emission source, most commonly a Cu rotating anode using the CuK$_\alpha$ emission line, or by using synchrotron radiation, which provides greater brilliance, better coherence, and the possibility of selecting photon energy.

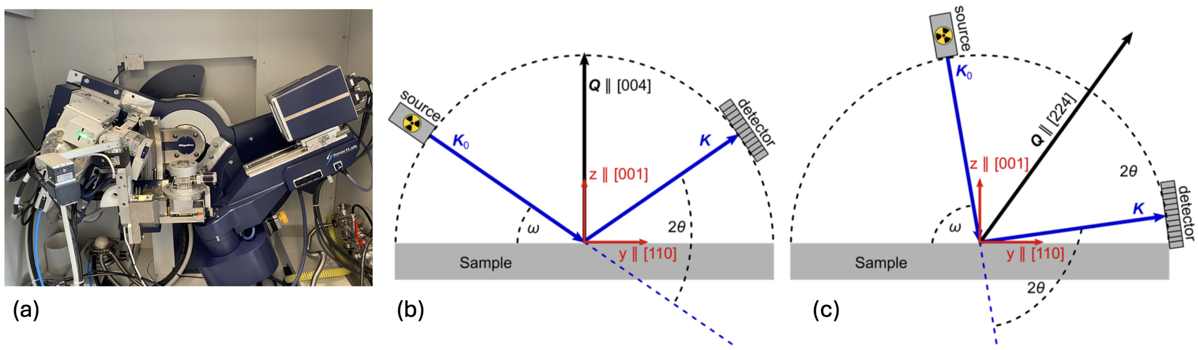

Figure 2.6: *(a) Rigaku smartlab present at IHP micorelectronics. (b) and (c) RSM scheme in the 2 configurations, respectively (004) and (224) [44].*

A key tool in HRXRD analysis is represented by the *Reciprocal Space Maps* (RSM), which allow us to precisely characterize the strain state of the epitaxial films. An RSM is obtained through a series of $\omega - 2\theta$ scans performed around a Bragg reflection along different directions of the scattering vector Q and provides a two-dimensional representation of the diffraction intensity in reciprocal space. From this representation, it is possible to distinguish the in-plane component ($q_\parallel$) and the out-of-plane component ($q_\perp$) of the vector Q. For samples with the standard (001) surface orientation, the symmetric (004) reflection and an asymmetric reflection, such as (224), are typically analyzed. In the case of silicon, both reflections have $q_\perp = 4/a_{\mathrm{Si}} = 7.365\,\mathrm{nm}^{-1}$ (with $l = 4$), while reflection (224) allows us to determine $q_\parallel = \sqrt{8}/a_{\mathrm{Si}} = 5.208\,\mathrm{nm}^{-1}$, which being $h^2 + k^2 = 8$. Initially, the Si(004) peak from the substrate is used as a reference, from which any deviation in the incident ($\Delta\omega$) and scattered ($\Delta\theta$) angles is obtained with respect to the theoretical parameters, so as to correct the map and, consequently, the SiGe and Ge peak positions measured.

After correcting the RSM using the substrate peak, the precise values of $q_\parallel$ and $q_\perp$ for the epitaxial film can be determined. From these, the lattice parameters parallel and perpendicular to the substrate surface are calculated as:

$$a_\parallel = \frac{\sqrt{h^2 + k^2}}{q_\parallel}, \qquad a_\perp = \frac{l}{q_\perp}, \tag{2.10}$$

where $q_\parallel$ and $q_\perp$ represent the components of the diffraction vector parallel and perpendicular to the surface, and h, k, l are the Miller indices of the planes under consideration. In the specific case of the (224) and (004) reflections of a film on a (001) substrate, one obtains

$$a_\parallel = \frac{\sqrt{8}}{q_\parallel}, \qquad a_\perp = \frac{4}{q_\perp}. \tag{2.11}$$

Considering an epitaxial film subjected to tetragonal strain with zero stress along the growth axis, the elastic relationship between $a_\parallel$, $a_\perp$ and the relaxed lattice parameter $a_0(x)$ of $Si_{1-x}Ge_x$ can be expressed, after algebraic manipulation, as a cubic equation in x:

$$Ax^3 + Bx^2 + Cx + D = 0, \tag{2.12}$$

where the coefficients A, B, C, D depend on the measured lattice parameters $a_\parallel$ and $a_\perp$ and on the elastic constants of the alloy. The real solution of this cubic equation, obtained using Cardano's formula, provides the Ge molar fraction x in the film. Once x has been determined, the relaxed parameter $a_0(x)$ is calculated by means of Dismukes' empirical law [45]:

$$a_0(x) = 5.431 + 0.200\,x + 0.027\,x^2 \tag{2.13}$$

which takes into account the slight non-linearity of the variation of the lattice parameter with composition.

The crystalline quality of the material is finally deduced from the shape and width at half height, referred to as Full Width at Half Maximum (FWHM), of the diffracted peaks, which provide indications of the density of dislocations and crystalline defects.

The HRXRD measurements presented in this work were performed at the Materials Research department of IHP Microelectronics laboratories, using a Rigaku SmartLab diffractometer equipped with a rotary and an area detector in linear focus geometry, equipped with a channel-cut collimator Ge(400)×2. It is also possible to perform in-situ measurements at temperature using an Anton Paar DHS 1100 heating stage, operating in a nitrogen atmosphere and covering a range of 25-1100 °C, and an Anton Paar DCS 500 cooling stage, which allows measurements between -200 and 500 °C under vacuum conditions.

2.4 Fourier-transform infrared spectroscopy (FTIR)

Fourier Transform Infrared Spectroscopy (FTIR) is an experimental technique that analyzes the changes experienced by infrared radiation following its interaction with a sample. It is based on the acquisition of the interferogram, which represents the intensity of the signal in the time domain, from which the spectrum is obtained using a Fourier transform [46].

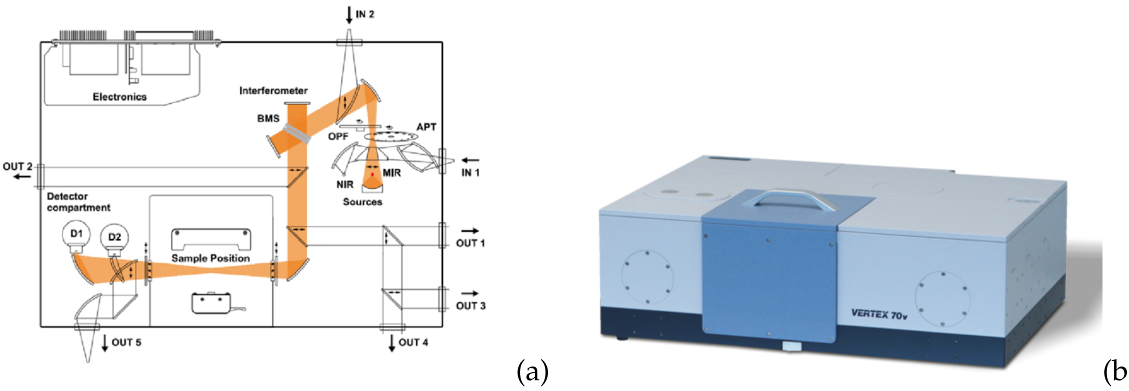

(a) (b)

Figure 2.7: *(a) Bruker Vertex v70 spectrometer scheme. (b) Vertex v70 spectrometer viewed from the outside.*

The most commonly used experimental apparatus is the Michelson interferometer, which exploits the phenomenon of optical interference to generate interference between two beams of light: one reflected by a fixed mirror and the other by a movable mirror.

The incident beam is split by a *beam splitter*, and the two beams, after being reflected, recombine, producing constructive or destructive interferences depending on the optical path difference. When the difference is zero (zero path difference, ZPD), all the waves interfere constructively, generating the maximum signal called *centerburst*.

The resulting interferogram $I(\omega)$ can be expressed as:

$$I(\omega) = \int B(\varepsilon)\cos(2\pi\varepsilon\omega)\,d\varepsilon \tag{2.14}$$

and the spectrum $B(\varepsilon)$ is obtained through the inverse Fourier transform:

$$B(\varepsilon) = \int I(\omega)\cos(2\pi\varepsilon\omega)\,d\omega \tag{2.15}$$

When a sample is placed in the optical path, the light is absorbed at frequencies corresponding to its specific excitations. This results in a reduction of the transmitted spectrum at the frequencies absorbed by the sample. In a real spectrum, various peaks may appear, which are related to the optics that the light traverses during its passage through the interferometer, but these are independent of the sample itself. To avoid incorrect interpretations, it is common to record a reference signal to obtain absolute transmittance spectra, which are defined as the ratio between the signal transmitted by the sample and the reference signal, thus providing information exclusively about the sample. FTIR spectroscopy can be conducted in transmission or reflectance mode. In the first case, the infrared radiation passes through the sample and the transmittance is given by the ratio:

$$T(\varepsilon) = \frac{I_T(\varepsilon)}{I_{T0}(\varepsilon)} \tag{2.16}$$

In the second case, the intensity of the reflected beam is measured, and the reflectance is obtained:

$$R(\varepsilon) = \frac{I_R(\varepsilon)}{I_{R0}(\varepsilon)} \tag{2.17}$$

In general, the relation must hold true:

$$R(\varepsilon) + T(\varepsilon) + S(\varepsilon) + A(\varepsilon) = 1 \tag{2.18}$$

where S represents the diffuse component and A the absorbed one. The described FTIR measurements were carried out using the Bruker Vertex v70 spectrometer, shown in Figure 2.7, a high-performance interferometer capable of covering a wide spectral range (from 6000 cm^{-1} to 50 cm^{-1}) in a single acquisition. The instrument operates under vacuum conditions ($<$ 2 mbar) to minimize absorption due to atmospheric H_2O and CO_2, and uses a broadband DTGS (*Deuterated Triglycine Sulfate*) detector, whose electrical response is proportional to the temperature variation induced by the incident IR radiation.

2.5 Schrödinger-Poisson solver

An in-depth understanding of the transport and optical properties of Ge/SiGe heterostructures has been obtained through simulations carried out using a self-consistent multivalley code that solves the Schrödinger-Poisson equation in the parabolic envelope function approximation. It is based on the multivalley $k \cdot p$ model and simulates the electronic states of $\text{Si}_{1-x}\text{Ge}_x$ alloys grown on a $\text{Si}_{1-y}\text{Ge}_y$ substrate, and thus, with different strain and at various temperatures [25]. The model allows obtaining the valence and conduction band profiles of SiGe-based heterostructures. In particular, concerning the conduction band, it enables deriving the L, Δ, and Γ profiles. The model considers the energies of the conduction band minima at the L, Δ, and Γ points of the Brillouin zone, providing a complete representation of the electronic structure. The band alignment is derived from a relation that includes the unstrained gap energies, spin-orbit contributions, hydrostatic and uniaxial strains, and average valence band levels, all calculated from pure Silicon and Germanium parameters.

In the model, donor impurities can be introduced to release electrons into the heterostructure and determine self-consistently, by solving the Schrödinger-Poisson equations, the electronic states at L, Δ_2, Δ_4, and Γ within the heterostructure and the electronic distribution in different states at various temperatures. Correlation-exchange effects among electrons confined in the L valley are also included. Figure 2.8 shows the simulation of a square quantum well, with the empty-band profile on the left and the full band configuration on the right. The structure consists of a 22 nm Ge well and a 22 nm $\text{Si}_{0.18}\text{Ge}_{0.82}$ barrier, grown

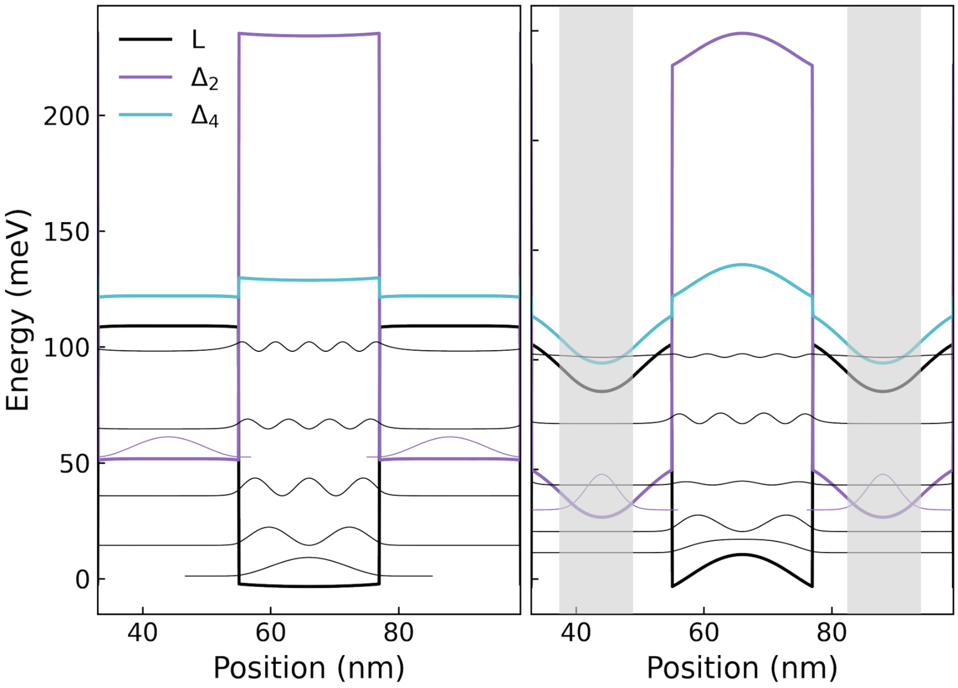

Figure 2.8: *On the left, the band structure of a square QW with 22-nm Ge well and a 22-nm* $Si_{0.18}Ge_{0.82}$ *barrier in strain compensation condition without doping within the barriers is observed, while on the right, a simulation of the same QW heterostructure is presented, but with the introduction of a doping of* $5 \cdot 10^{17} cm^{-3}$ *within the barriers. This latter configuration highlights the effects of band bending caused by charge transfer.*

on a strain-compensated virtual substrate: the barriers experience tensile strain, while the well is under compressive strain. By comparing the two configurations, it is evident that in the full band case, the conduction bands exhibit a pronounced bending and, in particular, a lowering of the Δ_2 valley. This behavior arises from the Hartree potential generated by the electric field established between the electrons occupying the barrier states and those localized near the center of the quantum well. The physical mechanism underlying this effect is discussed in detail in Chapter 5. Uniaxial deformation can remove the degeneracy of states, such as at Δ, by modifying the energies of the Δ_2 and Δ_4 states. A bending of the L, Δ_2 and Δ_4 bands profile is observed, attributable to transfer doping effects, as detailed in Chapter 1.5.5. An important result derived from the model is that the confinement potential profile at the conduction band minimum at L is directly proportional to the Ge content in the alloy. This implies that, to achieve a parabolic quantum well, it is essential to have a parabolic compositional profile of Ge. In summary, the model generates conduction band profiles, electronic states, and the corresponding wave functions. It also allows for the calculation of intersubband absorption energies, taking into account the depolarization shift and oscillator strengths, and thus simulates absorption spectra. Therefore, it is a valuable tool for designing heterostructures and modeling them to interpret experimental absorption data. The concentration profile of the QW used for simulations is then converted into growth process parameters suitable for obtaining a composition profile accurate at the sub nm level.

2.6 Sample growth and structural characterization

The growth of our samples was achieved using the previously described chemical vapor deposition (CVD) technique; the sketch is shown in Figure 2.4. A crucial aspect for high crystalline quality in the active layer region is the optimization of the virtual substrate (VS). To obtain $Si_{1-y}Ge_y$ virtual substrates on Si(001), we used the "reverse step grading" procedure, starting from the deposition of a relaxed Ge layer, then reducing the Ge content in steps until reaching the desired final concentration. Initially, the substrate, whose sketch is shown in Figure 2.9, was heated overnight to remove physisorbed impurities from the surface; subsequently, it was transferred into a chamber, and the first phase of treatment involves a high temperature to eliminate native oxide and any carbon and hydrogen residues present on the surface, in a hydrogen atmosphere at a pressure of 4 mTorr. After this cleaning phase, which lasts 10 minutes at a temperature of 1135 °C, silicon deposition is carried out to ensure crystalline quality and surface planarity. Subsequently, the deposition of the first Ge layer is performed. The growth of a pure Ge buffer occurs at a fixed germanium flow of 2.04 sccm. The process starts at a low temperature (310-335 °C) and a pressure of 4 mTorr, where kinetic effects due to thermodynamic non-equilibrium conditions and the presence of hydrogen that saturates free bonds hinder the movement of GeH_x species and prevent the formation of islands, despite the presence of strong lattice mismatch. This allows for the deposition of planar films, as the system relaxes through the formation of misfit dislocations.

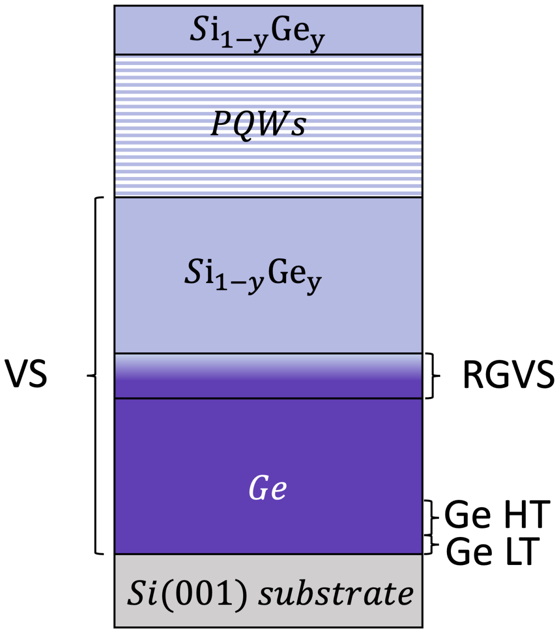

Figure 2.9: *Schematic of the structure of the samples used in this thesis, illustrating the different stages of the epitaxial growth process. The samples are fabricated on a Si(001) substrate, on which a Ge layer is grown that is divided into a low-temperature section (Ge LT) and a high-temperature section (Ge HT), followed by $Si_{1-y}Ge_y$ layers associated with the RGVS and VS phases. The structure includes PQWs with compressively strained $Si_{1-x}Ge_x$ wells, confined by tensile $Si_{0.18}Ge_{0.82}$ barriers.*

Once this phase is completed, during which a planar growth of a few nm begins, the growth temperature is increased to higher values to continue with the deposition of the germanium buffer up to a temperature of 688 °C for 30 minutes; this serves to improve the crystalline quality of the Ge film and to increase the initial growth rate to obtain a germanium layer about $\sim 500nm$ thick. Immediately after this step, the first annealing is initiated at 778°C for about 20 minutes at a pressure of 0.2 mTorr of germane gas; this helps to start facilitating the glide of dislocations within the Ge buffer. Subsequently, the pressure is set to 4 mTorr and the temperature to 550°C for about an hour, growing about 1 μm of germanium buffer. Again, an annealing occurs under the same conditions as the previous one for 10 minutes, and so on, until reaching a total Ge thickness of $\sim 3\mu m$. This thickness is chosen because it allows the virtual substrate to relax the lattice mismatch effectively while maintaining a low density of threading dislocations, providing a high-quality base for the subsequent growth of quantum well structures [9]. The deposition process is then finished with a last annealing before proceeding. In order to grow good quality QWs, they must be strain-compensated, meaning that the Ge concentration in the VS should match the average Ge concentration of the overlying Stack, as previously explained in the Section 2.1. This is to avoid plastic relaxation within them. We achieve this through the reverse grading described above. Thus, we descend in several steps, maintaining the same germanium flux and introducing the silane flux at each step at a temperature of 455°C, until reaching the required concentration y for the VS. The final concentration y depends on the design of the active region of the sample to be deposited. In most of the studied samples, it was around 90% germanium. Once the desired concentration is reached, we start the program "LabView" to grow 2 μm of SiGe VS and then the QWs stack. In Figure 2.10 the AFM, XRD and Etch pit count/Scanning Electron Microscopy (SEM) analysis of a $Si_{0.10}Ge_{0.90}$ VS is reported. Figure 2.10a shows an AFM image of a VS. Here, the presence of the typical cross-hatch pattern (CHP) is observed, which is mainly due to the plastic relaxation that occurs in heteroepitaxial films with lattice mismatch in the VS [47]. The effects of the CHP do not affect the structures, as the surface undulation on the plane is on the order of μm, while along the z direction it is on the order of nm. This means that the QWs grow coherently on the surface and are not influenced in their confinement properties.

The second characterization carried out is the structural characterization by X-ray diffraction (XRD). Specifically, reciprocal lattice maps (RSM) were acquired in the (004) and (224) directions at the Material Research IHP Microelectronics department laboratory. These analyses allow us to assess the strain, the composition of the various layers present in the sample, and the period of the QWs. We can compare Figure 2.10b, which shows a RSM acquired around the asymmetric (224) reflection of the VS. In this map, the axis coordinates represent the components of the scattering vector: the horizontal axis corresponds to the in-plane component $Q_{\parallel}$ or Q_x, while the vertical axis corresponds to the out-of-plane component $Q_{\perp}$ or Q_z. The most intense peak corresponds to the Si substrate, which serves as a reference. The peak related to the Ge buffer appears shifted with respect to Si due to its larger lattice parameter. Its position with respect to the *relaxation line*, which connects the

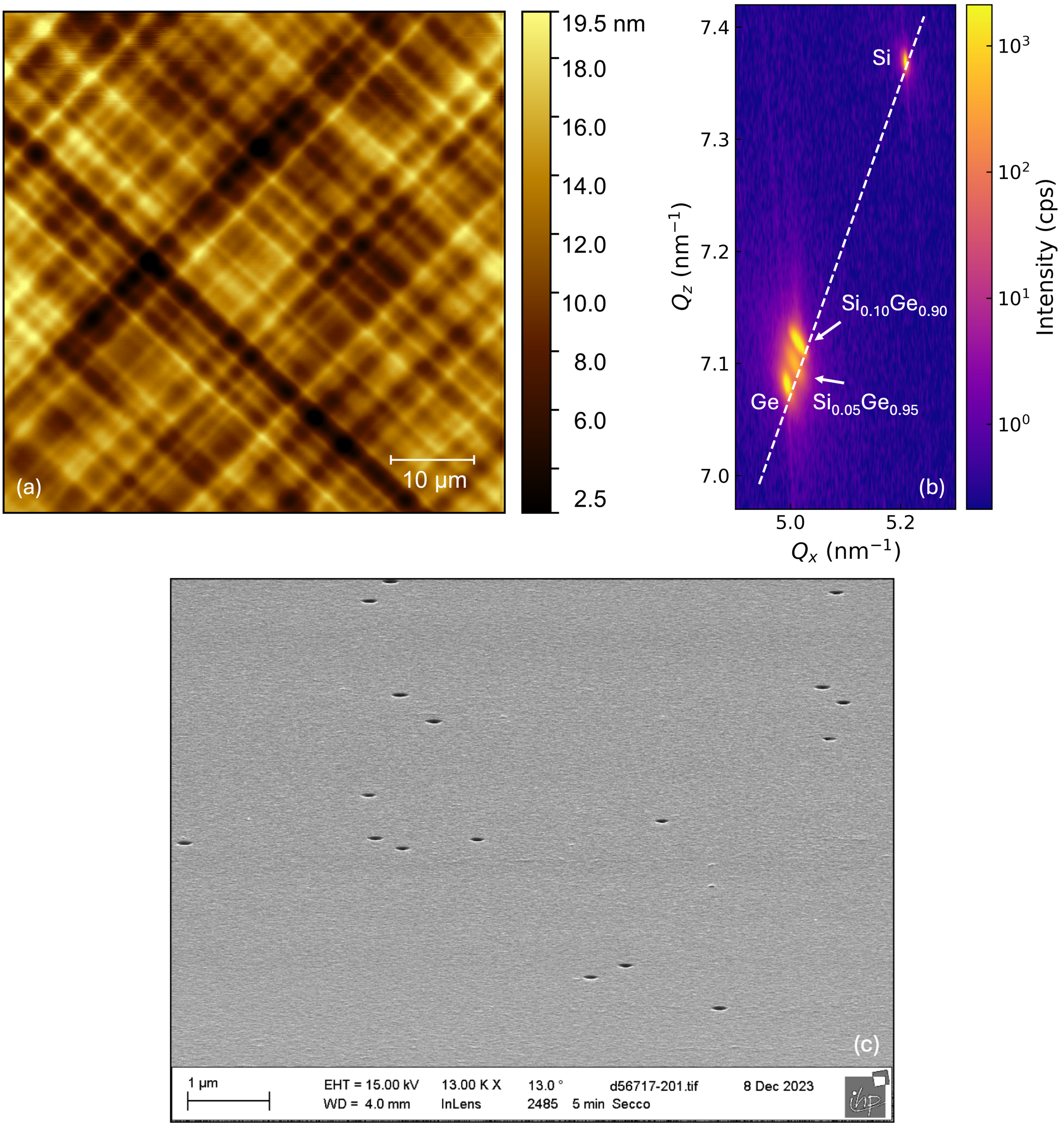

Figure 2.10: *(a) AFM image 60 μm x 60 μm of a VS showing the Cross-Hatch Pattern (CHP). (b) Reciprocal space map (RSM) along the (224) direction of a VS, with logarithmic intensity (cps) showing the diffraction peaks corresponding to Si, Ge, $Si_{0.10}Ge_{0.90}$, and $Si_{0.05}Ge_{0.95}$. (c) SEM image used for the estimation of the threading dislocation density (TDD) of VS with density of about* $2 \cdot 10^6 cm^{-2}$.

origin to the Si spot and indicates fully relaxed cubic materials, makes it possible to quantify the residual strain state; in our case, a biaxial strain of –0.14% is observed. The peaks located midway between Si and Ge indicate the SiGe alloy. The VS peak of $Si_{0.1}Ge_{0.9}$ is present. There is also a weaker peak between $Si_{0.1}Ge_{0.9}$ and Ge, due to the 95% RG. In Figure 2.10c presents a SEM image acquired after an etching process. These type of images were used to quantify the threading dislocations (TD). This procedure made it possible to obtain a good epitaxial layer (VS) with a TD density of about $2 \cdot 10^6$ cm^{-2}. The growth process of the stack is managed

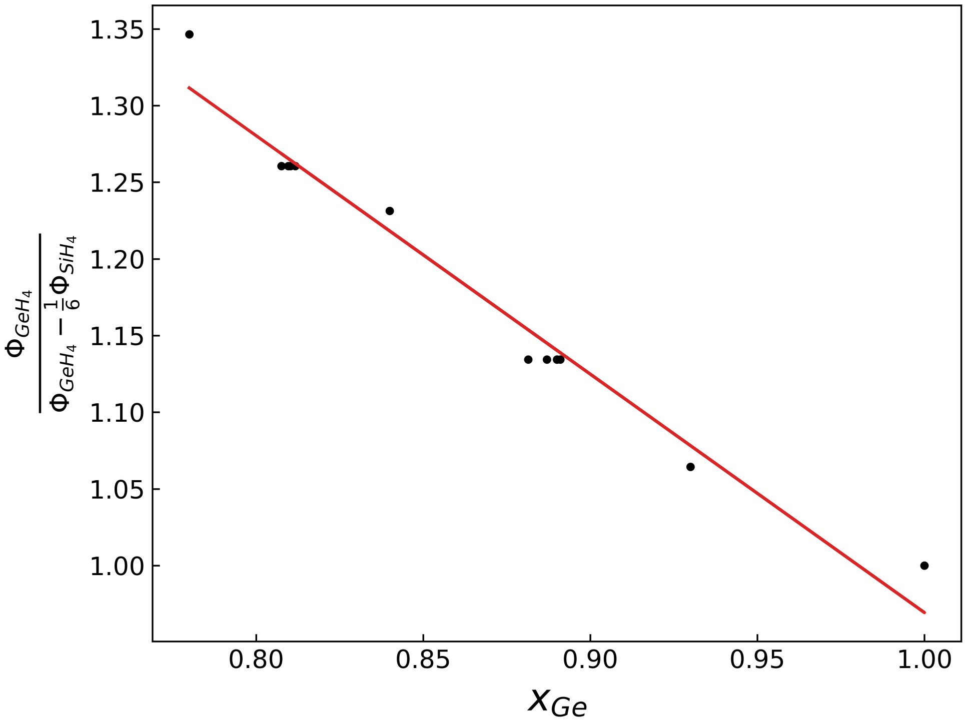

Figure 2.11: *Linear relationship between the ratio of* GeH_4 *and* SiH_4 *fluxes used during growth and the Ge concentration measured by XRD.*

through a control file in `.txt` format, consisting of a series of columns that sequentially specify the process parameters. Each column corresponds to a flow or an operational command of the CVD reactor, such as the opening or closing of valves for phosphine, silane, or germane flows. The control program interprets the file and sends real-time signals to the flow meters and electropneumatic valves, thus determining the temporal activation sequence of the different precursors and the reproduction of the established design for the structure. Since the reactor pressure control valve is kept in a fixed position, the operating pressure is determined by the flows of the introduced gases. Under these conditions, the process is calibrated by appropriately adjusting the flows of each precursor, in order to achieve the desired growth conditions. To this end, dedicated calibration samples have been created, used to accurately determine the relationships between nominal flows and the growth rates of the different constitutive layers of the structure. The samples were grown while keeping the GeH_4 flow constant and varying the SiH_4 flow to control the alloy composition. At a pressure of about 1 mTorr, the ratio between the flows $\phi(GeH_4)/(\phi(GeH_4) - \frac{1}{6}\phi(SiH_4))$ exhibits a linear trend, providing the relation that links the germanium concentration to the required silane flow. Figure 2.11 shows this relation as a function of the Ge concentration. This procedure has allowed for the optimization and reproducibility of deposition conditions for the final growth of the active part of the device. The precursor gas used for doping the samples is phosphine (PH_3). In Figure 2.12, an AFM image after the deposition of the MQWs is shown, demonstrating how the CHP remains unchanged after the growth of the stack, with an RMS roughness value of $3nm$ in both images.

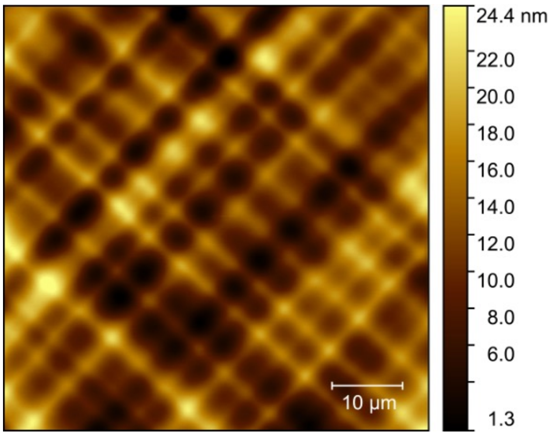

Figure 2.12: *AFM image 60 µm x 60 µm of a PQWs showing the CHP.*

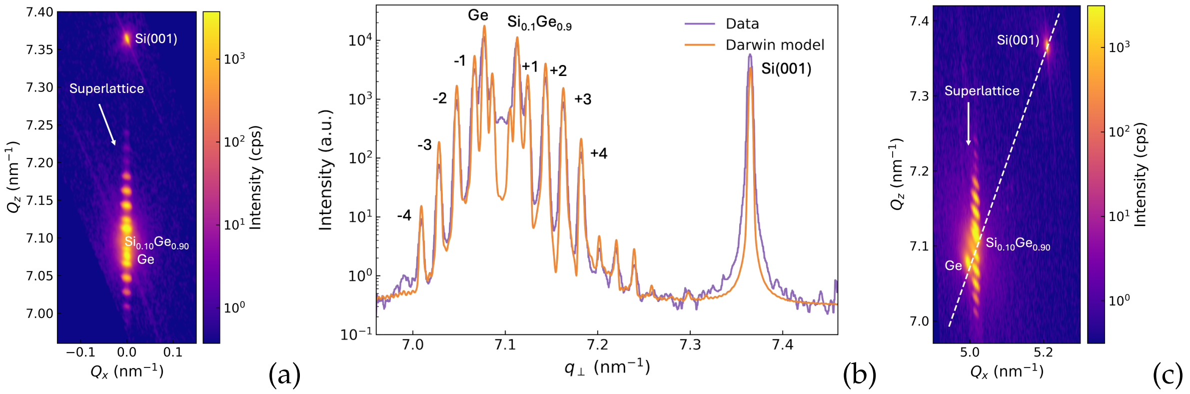

Figure 2.13: *XRD analysis of parabolic quantum wells (PQWs). (a) RSM along the symmetric (004) direction, showing the formation of the superlattice (SL), characterized by a zero-order peak (SL_0), associated with the average composition of the periodic structure, and by a series of satellite peaks (SL_{-1}, SL_{+1}, etc.) whose spacing is inversely proportional to the superlattice period. The vertical alignment of the SL peaks with respect to the virtual substrate (VS) peak indicates that the entire MQW stack has grown pseudomorphically, maintaining the in-plane lattice parameter. (b) Rocking curve estract from RMS(004), compared with the simulation based on the Darwin model, used to accurately extract the thickness of the wells and barriers. (c) RSM map along the asymmetric (224) direction, useful for evaluating the degree of relaxation and the strain distribution in the different layers, where the same peaks as in (004) are shown.*

The XRD analysis shown in Figure 2.13 makes it possible to observe the formation of a superlattice (SL). The diffraction spectrum is characterized by a zero-order peak (SL_0), associated with the average composition of the periodic structure, surrounded by a series of satellite peaks (SL_{-1}, SL_{+1}, etc.). The spacing between these satellite peaks is inversely proportional to the superlattice period. Furthermore, the vertical alignment of the satellite peaks with respect to the VS peak in the RSM map shows that the entire MQW stack has grown pseudomorphically with respect to the underlying virtual substrate, maintaining the same in-plane lattice parameter without plastic relaxation. By means of simulations based on the Darwin model [48], the experimental rocking curve shown in Figure 2.13b can be fitted to accurately determine the well thickness, the barrier thickness, and the alloy composition.

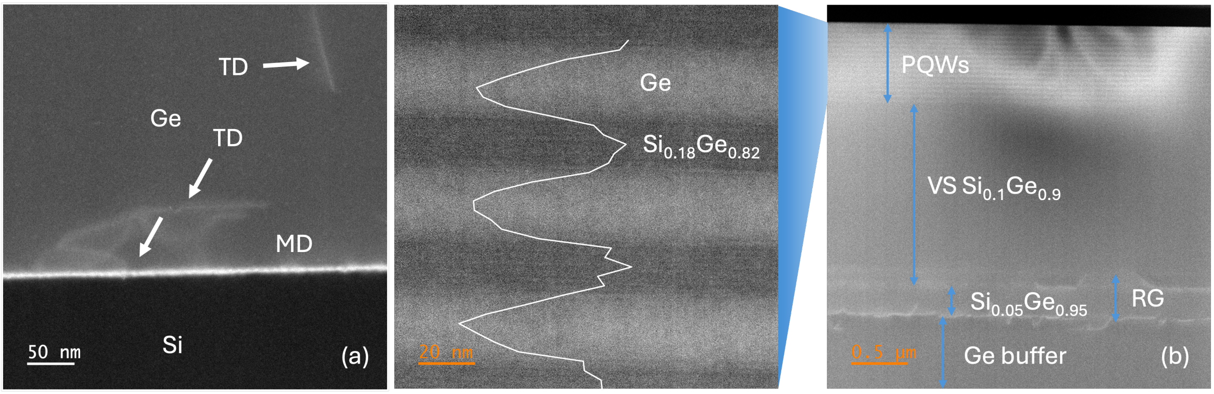

Figure 2.14: *STEM images: (a) Interface between the Si(001) substrate and the Ge buffer, highlighting threading dislocations (TD) and a misfit dislocation (MD). (b) Detail of the Ge/*$Si_{0.18}Ge_{0.82}$ *interface, the white line represents the parabolic profile extrapolated from the STEM image. (c) Overview of the Ge buffer of the SiGe virtual substrate and of the PQWs stack.*

In order to delve into the structural quality of the samples and, in particular, the profile of the QWs, a microstructural characterization was carried out using scanning transmission electron microscopy (STEM). The measurements were conducted at the CNR in Catania. High-resolution STEM images allow for precise assessment of the QW profile and local chemical composition analysis of the layers through combined spectroscopic techniques, such as EDX. These methods are particularly useful since XRD provides only averaged information over the entire sample volume. In Figure 2.16a, a STEM image of the interface between the Si substrate and the Ge buffer is shown. The contrast in the image arises from the difference in atomic number between Si and Ge, which produces a Z-contrast in HAADF-STEM: the Ge region appears clearer, while the Si region appears darker, and both the TD and MD are manifested as white-contrast features. At the interface, the presence of misfit dislocations (MDs) can be clearly observed as periodic distortions in the lattice fringes, while the arrows highlight the threading dislocations (TDs) propagating toward the surface. Figure 2.16b, on the other hand, shows the region between the Ge buffer and the PQWs, highlighting the sequence of different layers. The magnification shown in the inset allows for a detailed analysis of the defect-free QWs zone. From the intensity profile extracted from the image, it is observed that the QWs exhibit a parabolic trend, confirming the ability of the growth process to achieve the desired profile precisely.

2.7 Optical characterization

The optical characterization was carried out using FTIR measurements with the aim of determining the energy of ISB transitions in the PQWs. Specifically, FTIR transmission measurements were performed on samples grown on a silicon substrate and metallized on the top with Au/Ti to modify the boundary conditions of the interface, transforming it into an antinode for fields directed along the z-axis, thereby ensuring maximum coupling of the

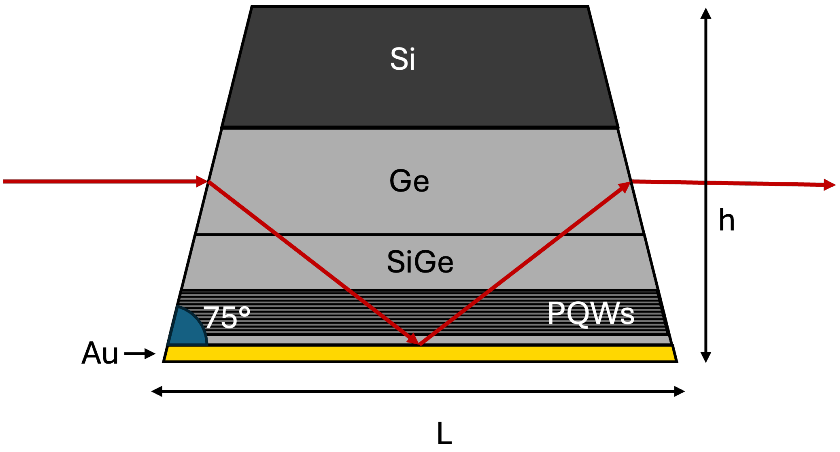

Figure 2.15: *Sample scketch used for dichroic transmission measurements of the PQWs. The structure consists of a Si(001) substrate, a Ge buffer, SiGe barriers, and parabolic quantum wells (PQWs), covered by a SiGe layer and Au/Ti metallization. The latter modifies the boundary conditions, turning the interface into an antinode for TM fields along the z axis and maximizing the coupling with intersubband transitions. The FTIR beam impinges at an angle of about 75°, close to the Brewster angle of Si, and travels along a L $\sim$ 2 mm waveguide that allows a single reflection in the active region.*

TM mode with the ISB transitions in this configuration, as shown in the sketch in Figure 2.15. The measurements are conducted inside a cryostat at various temperatures, ranging from 10 K to 300 K, with a beam entry angle of approximately 75° very close to the Brewster angle of Si (73.7°). The guide length of about 2 mm allows for a single reflection in the active region. Longer guides allow for signal amplification by increasing the number of reflections.

The measurements were carried out by acquiring in two polarization configurations: the transverse magnetic component TM (electric field along the growth direction z) and the electric component TE (electric field along the $x - y$ plane), shown in Figure 2.16. Shows the different signals in the two configurations, including the acoustic and optical phonons of silicon, the LO phonons of silicon, and the various minima of the TM and TE components, which are found to be out of phase. The sample consists of 25 PQWs of a 61 nm thick well with a period of 76 nm and a doping level of $3.7 \cdot 10^{11} cm^{-2}$. It is observed that the only signal present exclusively on the TM component is identified by the ISBT signal. To eliminate undesired contributions from the measurement system (polarizer, optics, parasitic reflections, etc.) and isolate the signal due exclusively to the MQWs, the ratio $\frac{T_{TM}}{T_{TE}}$ was calculated. This procedure is justified by the fact that most of the unwanted spectral contributions are distributed isotropically in the two polarizations, while the response of the MQWs is anisotropic and manifests only in the TM component, which is related to intersubband transitions.

Due to the various reflections on the interfaces of the different layers of the sample, from the substrate to the gold layer, the experimental spectrum also shows periodic oscillations due to interference effects, as shown in 2.17a. To extract the contribution of the MQW, it is therefore necessary to remove this background contribution. This operation was carried

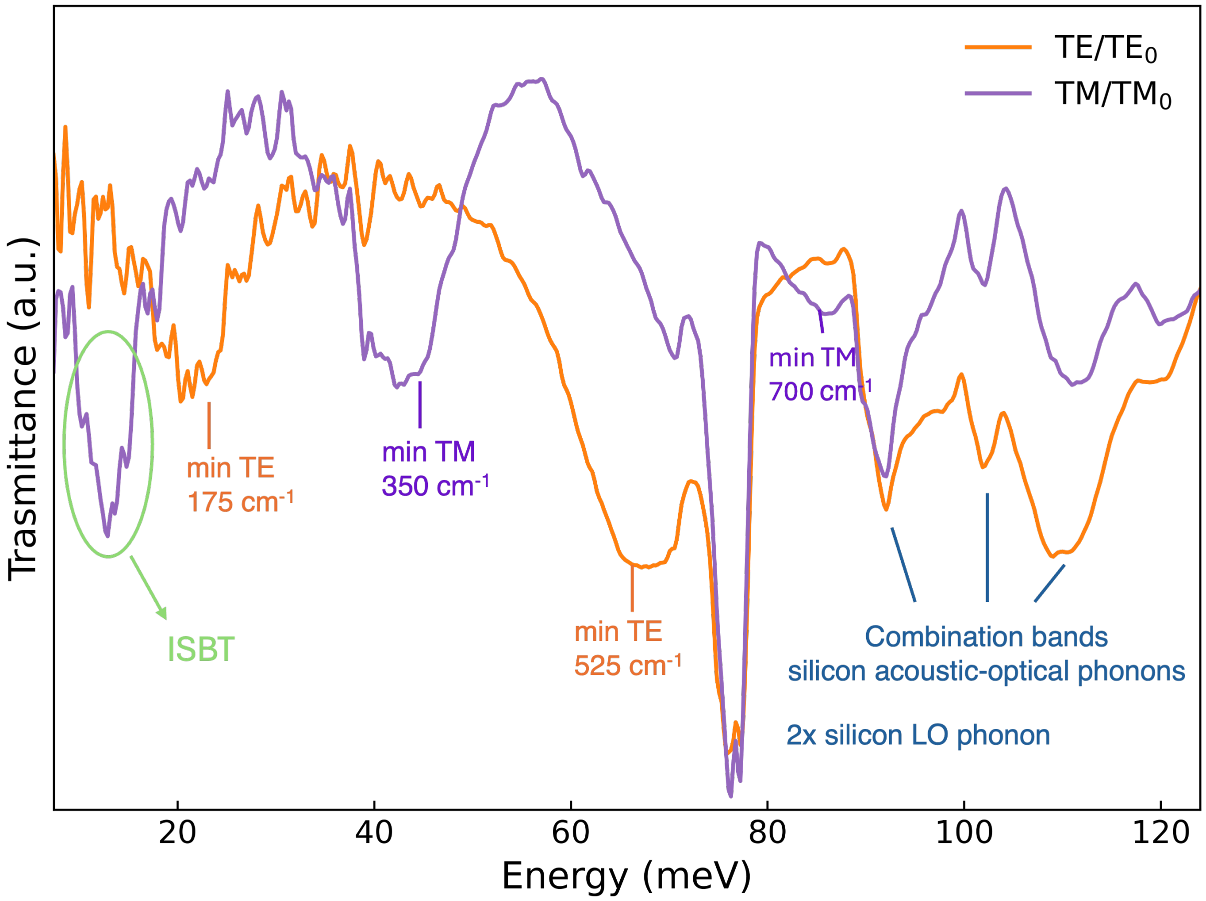

Figure 2.16: *Transmittance spectrum for TE and TM polarizations in a Ge/SiGe structure with PQWs, having a well width, $a = 61$ nm. The minimum in the TM component around 12 meV highlights the ISBT.*

out by modeling the background, where the Fabry-Pérot (FP) components are given by the Airy functions associated with the transmittance of the two polarizations TM and TE and constructing an equation for the background for the dichroic transmittance:

$$y(x) = \frac{b - FP(x) - Drude(x)}{b - FP(x - \delta\phi)} \cdot a + c \tag{2.19}$$

where ϕ is the phase difference between the Airy functions. The Drude term is given by $Drude(x) = \frac{\omega_p}{x^2+\gamma^2/4}$ and a; b and c are additional parameters that allow us to adjust the vertical position and amplitude. The FP term is given:

$$\text{FP}(x) = \frac{1}{1 + f\sin^2(\delta x)}, \quad \text{with } \delta = \frac{2\pi}{\lambda} 2nl\cos\theta \tag{2.20}$$

where θ is the angle of incidence of the light, f is the finesse coefficient related to the quality of the reflective surface, n is the refractive index of the material.

The function was subsequently fitted to the experimental data, allowing for the subtraction of the background and the isolation of the minimum in transmittance associated with absorption related to the ISBT. In Figure 2.17b, the dichroic transmittance curves for PQWs are illustrated once the background subtraction has been performed. Once the correct

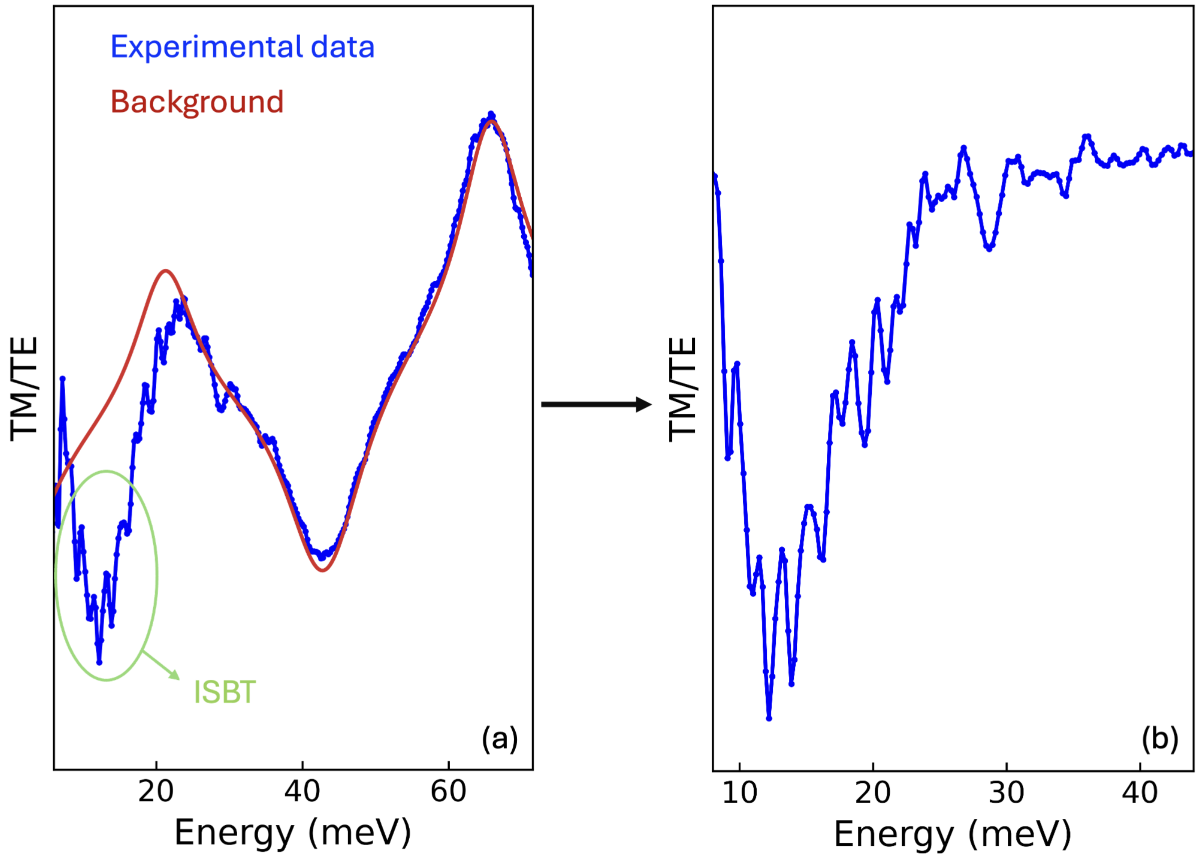

Figure 2.17: *Spectrum TM/TE of the same sample in Figure 2.16: (a) of a spectrum in blue and the corresponding background in red; (b) spectrum after background subtraction.*

spectrum was isolated, it was possible to derive the absorption coefficient, α_{2D} (Figure 2.18).

$$\alpha_{2D} = -\frac{\ln[T(E)]\cos\theta}{CMN_w \sin^2\theta}, \tag{2.21}$$

where N_w is the number of QWs comprised in the structure, M is the number of reflections, and C is the amplifying factor of the z-component of the electric field due to the surface metal deposition. This latter parameter is estimated to be C=1.5 for the samples investigated in this work. From the absorption coefficient, the two-dimensional carrier density n_{2D} was determined, considering the proportionality between the peak area and the latter:

$$\int \alpha_{2D}(E) = n_{2D}\frac{\pi\hbar e^2}{2\epsilon_0 \eta c m^*}, \tag{2.22}$$

The absorption peak of the PQW, shown in Figure 2.18a, derived from the dichroic transmission measurements in Figure 2.17b, was fitted using a Lorentz function (continuous line), from which the characteristic parameters were extracted: the peak position from which the energy of the ISBT is derived, the peak area which is proportional to the transferred doping (n_{2D}), and the full width at half maximum (FWHM) of the absorption peak. From these parameters, it was possible to experimentally determine the value of n_{2D} for each analyzed sample. In Figure 2.18b, the absorption spectra measured at different temperatures are

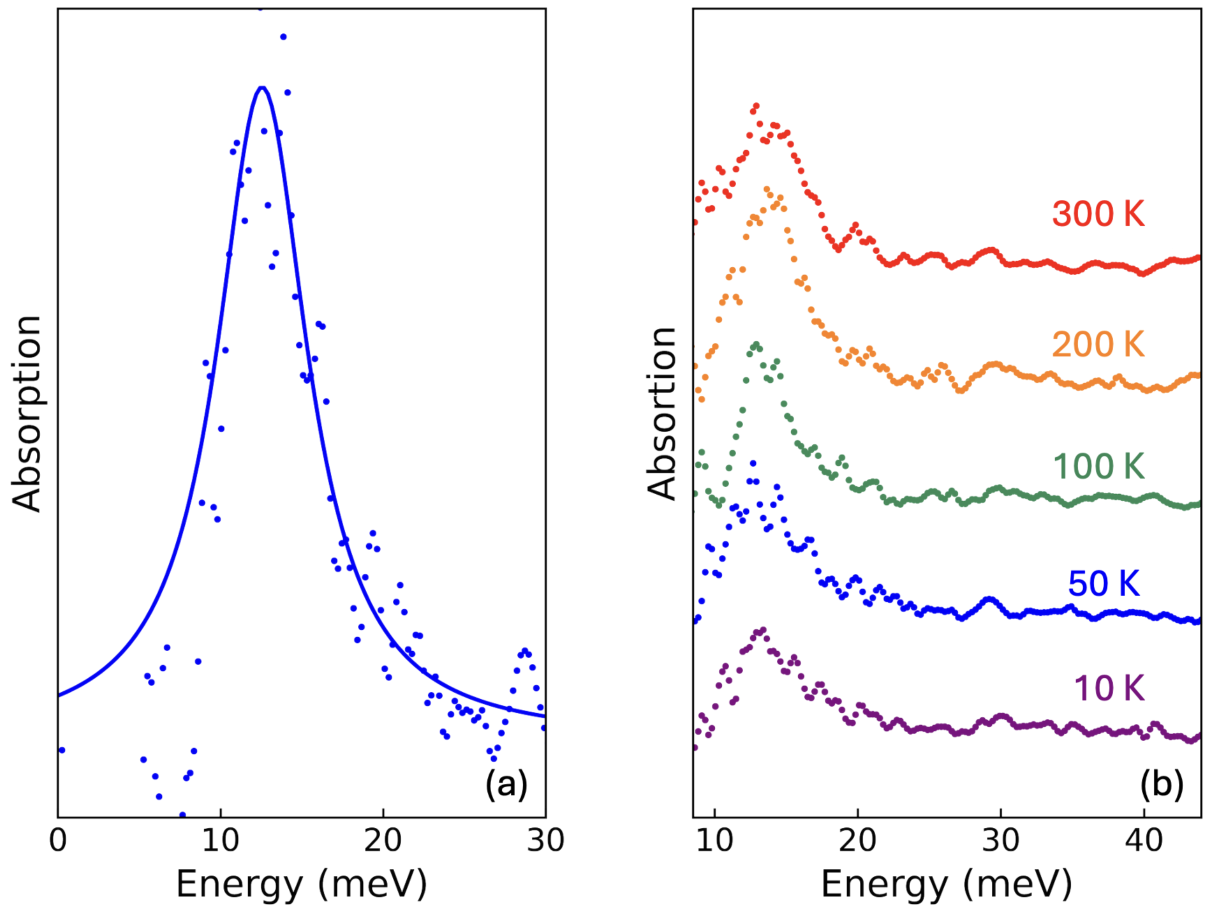

Figure 2.18: *Absorption as a function of energy after background removal of the same sample of 2.17: (a) at 50 K and (b) at different temperature.*

presented. All spectra exhibit a single peak located at the same transition energy, as expected for PQWs. In PQWs, the absorption peak does not shift with temperature thanks to Kohn's theorem: the levels are equally spaced and the collective frequency remains unchanged even if the subband population varies. In rectangular QWs, on the other hand, this no longer holds and the peak can shift. As shown in Fig. 3 of M. Seta et al. (2012) [49], a redshift is indeed observed in an MQW between 10 and 80 K. This observation indicates that both the structural design and the epitaxial growth procedure were successfully implemented. The second type of configuration used for FTIR measurements is the reflection configuration. This approach was employed to observe the characteristic splitting of the ultra-strong coupling regime. To this end, it was necessary to create a bottom mirror and proceed with the fabrication of optical microcavity arrays (see Figure 2.19), which allow achieving photonic resonance.

The reflectivity measurements of the microcavities were carried out using the Bruker Vertex 70v FTIR spectrometer available in the laboratories of La Sapienza University. The spectrometer operated under vacuum conditions and was connected to a helium-flow cryostat that allowed stable operation in the temperature range between 10 and 300 K. In order to enable the analysis of the patch array, the system was equipped with an optical insert with

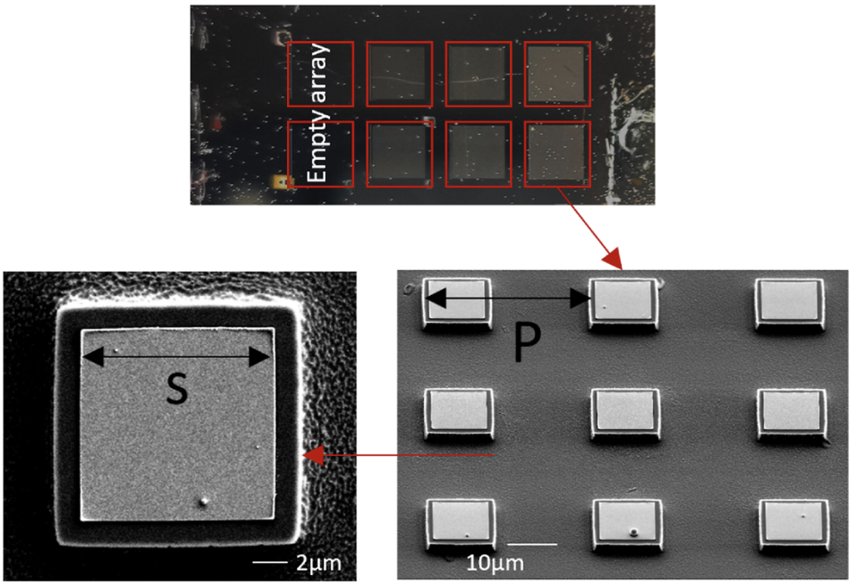

Figure 2.19: *Optical microscope view of the 1 × 2 cm epitaxial chip (top), divided into six 2 × 2 mm² fields, each containing cavities with different widths s. On the right, a magnified view of a patch cavity array with a period P = 3s, where the semiconductor ground plane can be distinguished from the square gold patches. On the left, a close-up of a single patch cavity with width s = 11 µm. The fabrication was carried out by collaborators of the IFN-CNR of Rome Tor Vergata.This figure is shown in the second article [33] reproduced in Chapter 4.*

a high numerical aperture, based on a pair of ellipsoidal mirrors. As a reference, a region of the same sample was used in which the structure had been etched down to the heavily doped VS. For each microcavity array, a reflectivity spectrum $R_{\mathrm{cav}}(\omega)$ was thus acquired, while the reference $R_{\mathrm{Ge}^{n++}}(\omega)$ was measured under the same experimental conditions. The analysis consists of normalizing the two measurements by calculating the ratio

$$\tilde{R}(\omega) = \frac{R_{\mathrm{cav}}(\omega)}{R_{\mathrm{Ge}^{n++}}(\omega)}.$$

This step is mandatory to eliminate almost all contributions not associated with the cavity resonances, such as spurious reflections from the signal, slow modulations of the source intensity, and, in general, the response of the substrate and the optics. The practical effect of this normalization is to clearly highlight the resonant structure arising from the interaction between the cavity and the intersubband transition of the parabolic quantum well. The extraction of the polaritonic mode frequencies was performed using a parabolic background with one or two Lorentzian functions. Figure 2.20, shows the dichroic transmittance (purple curve) of a PQW sample with a 76 nm period and an ISBT at approximately 3 THz, together with the reflectivity spectra measured on patch microcavity arrays fabricated on undoped and doped PQW samples of the same design, whose resonance energy is matched to the ISBTs.

Once the central frequencies of the Lorentzian peaks have been extracted, denoted by ω_{UP} and ω_{LP} for the two polaritonic branches, the experimental dispersion is obtained by repeating the entire procedure for all the geometries considered, as reported in Chapter 4.

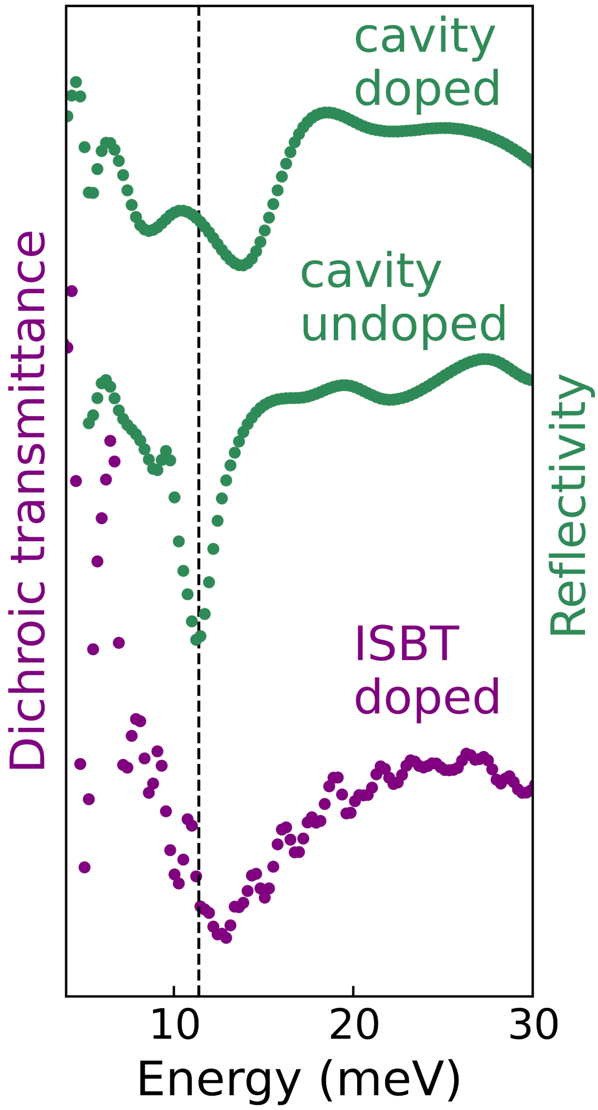

Figure 2.20: *Dichroic trasmittance and Reflectivity as a function of energy for a sample with the same design of figure 2.17. In purple, the ISBT is shown. In green, the reflectivity measurements performed on the same sample are reported, but using the mirrors of an undoped cavity, tuned to the same energy as the ISBT. When the doped cavity is resonant at the same energy as the undoped cavity, a splitting of the resonance peak (cavity doped) is observed.*

3

HIGH-QUALITY CMOS COMPATIBLE N-TYPE SIGE PARABOLIC QUANTUM WELLS FOR INTERSUBBAND PHOTONICS AT 2.5-5 THZ

As we have discussed, Intersubband transitions (ISBTs) in semiconductor quantum wells enable the realization of efficient emitters, detectors, and modulators operating in the infrared and THz spectral regions. In this article published on Nanophotonics [32], we have demonstrated the fabrication of high-quality n-type Ge-rich SiGe parabolic quantum wells (PQWs) exhibiting intersubband transition energies in the range of 2-2.5 THz. Among the different quantum well profiles, parabolic quantum wells hold a special role. Their confinement potential along the growth direction mimics that of a harmonic oscillator, resulting in a ladder of equally spaced quantized energy levels and, consequently, a single well-defined resonance frequency for ISBTs. As a matter of fact, as discussed in Section 1.5.5, in modulation-doped PQWs, electron-electron interactions are suppressed in accordance with Kohn's theorem, making the resonance frequency essentially independent of carrier density and temperature. This property allows PQWs to overcome one of the key limitations of square QWs, whose ISBT energies typically shift with thermal fluctuations and doping.

The epitaxial growth of n-type high-Ge content SiGe PQWs on Si substrates presents significantly greater challenges compared to their III-V counterparts. Specifically, precise compositional grading is hindered by Ge surface segregation and Si-Ge intermixing effects occurring during growth, while sharp doping profiles are difficult to achieve due to the tendency of donor atoms, such as phosphorus, to float toward the growth front. These technological hurdles have historically limited the quality of group-IV PQWs. For instance, previous attempts by Ballabio et al., utilizing plasma-enhanced chemical vapor deposition (PECVD), resulted in structures with strong deviations from the target parabolic profile [50]. Achieving a precise compositional grading is made difficult by the surface segregation of Ge and by interdiffusion processes, which hinder the accurate definition of the parabolic potential. At the same time, the tendency of phosphorus to migrate toward the growth front generates diffusion tails of about 3.5 nm, shifting the donor distribution with respect to the center of the barriers. [51]. Demonstrating high-quality, coherently strained SiGe-based PQWs, therefore, represents a significant milestone for the full exploitation of this material system.

In this work, we report the realization of continuously graded Ge/SiGe PQWs grown by UHV-CVD on Si(001). A systematic study of their structural and optical properties is presented, covering PQWs with different widths and doping levels and targeting transition energies down to 10 meV. Structural characterization, with HR-XRD, SIMS and STEM, demonstrates that UHV-CVD enables precise control of the parabolic confinement potential through the precise tuning of the Ge content profile that reproduces the target profiles with high fidelity. Another important result achieved is the control over the doping profile, with SIMS measurements evidencing that P atoms are confined in the central part of the barriers.

Fourier-transform infrared (FTIR) spectroscopy reveals a single, well-defined absorption peak with a remarkably small full width at half maximum (FWHM): approximately 2 meV at low temperature and 5 meV at room temperature. The resonance energy scales with the inverse of the well width, covering the 2.5-5 THz spectral range, and is nearly independent of temperature and doping, in excellent agreement with theoretical expectations for an ideal parabolic potential.

In this project, I focused on the epitaxial growth of the PQWs and the analysis of the FTIR absorption spectra. The FTIR measurements were performed at Sapienza University in collaboration with Dr. Venanzi and Dr. Berkmann. For these measurements, the samples were shaped into a prism geometry, which enabled efficient coupling of the incident radiation into the multilayer structure. TM and TE transmission spectra were acquired to isolate the contribution of the intersubband transitions from the overall optical response of the samples.

I personally took part in the measurements and subsequently analyzed the acquired spectra following the procedure described in Section 2.7, in order to extract the n_{2D} associated with the ISBTs.

This combined structural and optical investigation confirms both the high structural quality of the fabricated wells, and their true parabolic electronic confinement, as evidenced by the temperature-invariant intersubband resonance predicted by Kohn's theorem.

A comparison with previous works on Ge/SiGe intersubband devices highlights the relevance of these results. Earlier demonstrations based on square wells typically showed larger linewidths (around 4 meV). In contrast, the continuously graded PQWs realized here exhibits a faithful parabolic potential and a single, sharp resonance with FWHM as low as 2 meV, substantially narrower than in earlier group-IV implementations. Moreover, the negligible dependence of the transition energy on temperature and doping, consistent with Kohn's theorem, marks a clear improvement relative to previously reported SiGe systems. These results, therefore, position the present structures among the most advanced group-IV platforms for THz intersubband optoelectronics.

Overall, this study demonstrates the feasibility of fabricating CMOS-compatible n-type SiGe parabolic quantum wells with excellent structural and optical properties, establishing a solid foundation for the development of next-generation THz optoelectronic devices integrated into silicon technology.

Research Article

Elena Campagna, Enrico Talamas Simola, Tommaso Venanzi, Fritz Berkmann, Cedric Corley-Wiciak, Giuseppe Nicotra, Leonetta Baldassarre, Giovanni Capellini, Luciana Di Gaspare, Michele Virgilio, Michele Ortolani* and Monica De Seta

High-quality CMOS compatible n-type SiGe parabolic quantum wells for intersubband photonics at 2.5–5 THz

https://doi.org/10.1515/nanoph-2023-0704
Received October 16, 2023; accepted December 13, 2023;

Abstract: A parabolic potential that confines charge carriers along the growth direction of quantum wells semiconductor systems is characterized by a single resonance frequency, associated to intersubband transitions. Motivated by fascinating quantum optics applications leveraging on this property, we use the technologically relevant SiGe material system to design, grow, and characterize n-type doped parabolic quantum wells realized by continuously grading Ge-rich $Si_{1-x}Ge_x$ alloys, deposited on silicon wafers. An extensive structural analysis highlights the capability of the ultra-high-vacuum chemical vapor deposition technique here used to precisely control the quadratic confining potential and the target doping profile. The absorption spectrum, measured by means of Fourier transform infrared spectroscopy, revealed a single peak with a full width at half maximum at low and room temperature of about 2 and 5 meV, respectively, associated to degenerate intersubband transitions. The energy of the absorption resonance scales with the inverse of the well width, covering the 2.5–5 THz spectral range, and is almost independent of temperature and doping, as predicted for a parabolic confining potential. On the basis of these results, we discuss the perspective observation of THz strong light–matter coupling in this silicon compatible material system, leveraging on intersubband transitions embedded in all-semiconductor microcavities.

Keywords: heterostructures; germanium; terahertz; strong coupling; parabolic potential

1 Introduction

Intersubband transitions (ISBTs) in quantum wells (QWs) have garnered significant attention due to their relevance across a wide spectrum of applications. These transitions between quantized energy levels within the well have unlocked a wealth of opportunities for designing novel electronic and photonic devices with unprecedented performance. In the realm of infrared and terahertz photonics, they enable the development of efficient detectors, modulators, and emitters [1]–[3]. ISBTs are also at the heart of quantum cascade lasers (QCLs), a groundbreaking

---

Present address: Cedric Corley-Wiciak, ESRF – European Synchrotron Radiation Facility, 71, avenue des Martyrs, CS 40220, 38043 Grenoble Cedex 9, France.

***Corresponding author: Michele Ortolani**, Center for Life Nano & Neuro Science, Istituto Italiano di Tecnologia, Viale Regina Elena 291, 00161 Rome, Italy; and Department of Physics, “Sapienza” Università di Roma, Piazzale Aldo Moro 2, 00185 Rome, Italy, E-mail: michele.ortolani@roma1.infn.it. https://orcid.org/0000-0002-7203-5355

Elena Campagna, **Enrico Talamas Simola**, **Luciana Di Gaspare and Monica De Seta**, Dipartimento di Scienze, Università; degli Studi Roma Tre, Viale G. Marconi 446, Roma 00146, Italy,
E-mail: elena.campagna@uniroma3.it (E. Campagna),
enrico.talamassimola@uniroma3.it (E. Talamas Simola).
https://orcid.org/0000-0001-7121-8806 (E. Campagna).
https://orcid.org/0000-0001-5468-6712 (E. Talamas Simola)

Tommaso Venanzi, Center for Life Nano & Neuro Science, Istituto Italiano di Tecnologia, Viale Regina Elena 291, 00161 Rome, Italy,
E-mail: tommaso.venanzi@uniroma1.it

Fritz Berkmann and Leonetta Baldassarre, Department of Physics, “Sapienza” Università di Roma, Piazzale Aldo Moro 2, 00185 Rome, Italy,
E-mail: fritz.berkmann@uniroma1.it (F. Berkmann)

Cedric Corley-Wiciak, IHP-Leibniz Institut für Innovative Mikroelektronik, Im Technologiepark 25, Frankfurt (Oder) 15236, Germany,
E-mail: cedric.corley@esrf.fr

Giuseppe Nicotra, Istituto per la Microelettronica e Microsistemi (CNR-IMM), VIII Strada 5, Catania 95121, Italy

Giovanni Capellini, Dipartimento di Scienze, Università; degli Studi Roma Tre, Viale G. Marconi 446, Roma 00146, Italy; and IHP-Leibniz Institut für Innovative Mikroelektronik, Im Technologiepark 25, Frankfurt (Oder) 15236, Germany

Michele Virgilio, Dipartimento di Fisica “E. Fermi”, Università; di Pisa, Largo Pontecorvo 3, Pisa 56127, Italy, E-mail: michele.virgilio@unipi.it

technology that has revolutionized the generation of coherent mid/far-infrared radiation [4]–[6].

Among the quantum well profiles, parabolic quantum wells (PQWs) feature a unique harmonic oscillator-like carrier confinement potential along the growth direction. This results in the formation of a ladder-like energy spectrum within the well, with equally spaced quantized energy levels. Furthermore, in modulation-doped parabolic QWs, i.e., QWs with dopant atoms located outside the parabolic potential region, the electron–electron interaction cancels out and, following Kohn's theorem, the ISB optical resonance frequency ω_0 becomes independent of the carrier density and of their distribution in the different subbands [7]. Consequently, the absorption spectrum of PQWs is virtually temperature independent. This characteristic can be exploited to overcome the thermal charge fluctuation limitations of THz optoelectronic devices based on, i.e., rectangular QWs [5].

ISBTs in a QW system represent the solid-state equivalent of the ideal two-level atomic system but with the advantage of the tunability of the associated quantum transition by a suitable band engineering. In particular, the transition energy can be tuned at the resonance frequency of an optical cavity, a platform that has been used to explore the strong light–matter coupling regimes [8]–[11]. The coupling strength can be further externally tuned by leveraging on doping, field-effect [12], Stark-effect [13], magnetic field [10], [14], or optical-field tunability [15]. Indeed, the rate of energy exchange between light and matter excitations in the cavity, usually expressed in terms of the Rabi frequency Ω_R, can be varied acting on the carrier density in the QW, while the ISB transition frequency ω_0 can be freely selected in the mid-infrared and terahertz ranges through the semiconductor heterostructure design. In this way, it is possible to obtain different regimes of the light–matter coupling in individual subwavelength-sized microcavities, often evaluated by the ratio $\eta = \frac{\Omega_R}{\omega_0}$, spanning from the weak regime $\eta < 0.05$ to the (ultra)-strong regime for $\eta > 0.1$ [16]. The intriguing possibilities of controlling and manipulating these mixed light and matter quantum states paved the way for the development of novel devices such as polariton lasers, ultrafast modulators, and quantum information processors [15], [17].

Thanks to their inherent single-valued absorption spectrum and temperature independence, ISBTs in PQWs enclosed in an optical cavity has led to the realization of the ultra-strong light–matter coupling at room temperature and at THz frequencies [18]. Notably, all reported studies on PQWs are based on III–V compound semiconductors, in which the parabolic potential has been achieved first by digitally alloying GaAs and $Al_{0.15}Ga_{0.85}As$ layers [11], and, only in the last few years, by implementing continuously graded $Al_{1-x}Ga_xAs$ quantum wells [19].

In recent years, group-IV QWs have emerged as a promising alternative to the III–V ones, offering a material platform for advanced electronic, photonic, and quantum functionalities, compatible with the well-established silicon technology base. Various applications ranging from photonics [20] to quantum computing [21] and microelectronics [22] have been proposed. In this context, Ge-rich $Si_{1-x}Ge_x$ QWs ($x > 0.80$) formed in the conduction band of n-type multilayers are particularly promising for the development of photonic devices operating in the THz range thanks to their relatively low confinement mass ($\sim 0.13\ m_0$) and simpler subband structure with respect to p-type SiGe systems [23], [24].

These characteristics suggest that n-type Ge-rich SiGe PQWs embedded into microcavities may also be used to achieve the strong coupling regime at THz frequencies also in group IV based structures, provided that high-quality samples can be satisfactorily realized with the existing epitaxial techniques. As a matter of fact, the epitaxial growth of n-type high Ge content SiGe QWs on Si substrates is more challenging than that of their III–V counterparts, mainly because of the large (4.2 %) mismatch existing between the Ge and Si lattice parameter, eventually leading to the plastic relaxation of the QW structures if not correctly managed. Furthermore, the control over the QW compositional profile is complicated by the tendency of Ge atoms to segregate on top of the growing surface and by the Si–Ge intermixing effect occurring during the growth. Also the realization of a sharp doping profile is problematic, due to the well-known tendency of donor atoms to "float" on Ge during the growth [25]. Indeed, only the recent improvements in the heteroepitaxial process of this material system have allowed a high degree of control over these physical effects [26]–[28], as witness by the observation in 2021 of ISB electroluminescence in the THz range from n-type Ge/SiGe QCL structures [29].

In view of the above observations, the demonstration of high-quality SiGe based PQWs represents another important milestone toward the full exploitation of this technologically relevant material system. A first attempt in this direction has been made in Ref. [30] where the authors reported on a set of Ge-rich SiGe PQWs. However, the investigated samples were undoped and the structural data highlighted strong deviations from the target parabolic profile. Genuine parabolic confining potential in n-type SiGe multilayer systems have been obtained only in 2021, using the same reactor here adopted: we have presented the experimental evidence of conduction-band intersubband transition energies around 20 meV, resulting from compositional graded $Si_{1-x}Ge_x$ parabolic quantum wells [31]. To consolidate and extend this result, here we report on a comprehensive study of the structural and optical properties of compositional graded $Si_{1-x}Ge_x$ PQWs having different well width and doping levels. The experimental features have been benchmarked against numerical ISB absorption data obtained by a multivalley self-consistent Schrödinger–Poisson solver. To highlight the unique properties of the harmonic confining potential, we have here designed PQW profiles corresponding to lower energy ISBTs with respect to those of Ref. [31], thus targeting an energy range down to 10 meV where the ISB spectral properties of square QWs are more sensible to thermal effects.

Our results demonstrate that UHV-CVD permits the realization of a stack of identical compositional graded $Si_{1-x}Ge_x$ PQWs with high reproducibility of the growth along the stack and in different samples. The high quality of these samples allowed the observation of narrow ISB absorption peaks and the tuning of the ISB absorption energy in the range between 10 and 20 meV (2.5–5 THz). Due to their parabolic confining potential, the measured absorption energy results to be temperature independent and rescales linearly with the inverse of the well width W.

These achievements are promising for the perspective use of compositional graded $Si_{1-x}Ge_x$ PQWs for the development of CMOS compatible novel optoelectronic devices operating in the THz range.

2 Methods

Samples were grown by means of UHV-CVD in a cold-wall reactor employing ultrapure germane and silane without the use of carrier gases at a pressure $p \sim 1$ mTorr. The parabolic compositional profile $Si_{1-x}Ge_{1-x}$ with x in the 0.8–1 range is obtained by keeping the GeH_4 gas flow constant and gradually varying the SiH_4 flow by means of calibrated mass flow controllers (the SiH_4/GeH4 flux ratio R_{flux} have been varied from $R_{\text{flux}} = 0$ during the pure Ge deposition to $R_{\text{flux}} = 1.24$ for $x = 0.82$). The sample active region typically consisted of alternating several identical PQWs and SiGe barriers. The growth temperature for this active stack was set at 460° and the average growth rate was 6 nm/min. N-type modulation doping was achieved by codepositing phosphine to a thickness of 3–5 nm in the center of the SiGe barriers.

The active layer stack was deposited on top of a reverse graded (RG) virtual substrate (VS), consisting of a relaxed Ge film grown directly on the Si substrate using a multi-temperature approach, and a relaxed $Si_{1-y}Ge_y$ buffer layer [32]. The final composition y of the SiGe buffer matched the average composition of the active stack to ensure the strain compensation condition and avoid the plastic relaxation of the active region.

The structural characterization of the samples was conducted using high resolution scanning transmission electron microscopy (STEM), X-ray diffraction (XRD), and time-of-flight secondary ion mass spectroscopy (ToF-SIMS). STEM measurements have been realized with a FEI Titan microscope (FEI Company, Hillsboro, Oregon, USA) operating at 200 kV. It was equipped with aberration-corrected magnetic lenses to obtain electron probes with a diameter in the range of 1–2 Å and beam currents of 200 pA. A CEOS CESCOR corrector was used to achieve a resolution of 0.8 Å. Images were recorded using a high-angle annular dark field (HAADF) detector (FEI Company, Hillsboro, Oregon, USA). XRD measurements were performed at room temperature using a Rigaku SmartLab instrument with a rotating anode and line-focus geometry, featuring a Ge(400) × 2 channel-cut beam collimator. Tof-SIMS compositional profiles were acquired in a ToF-SIMS V from IONTOF. The depth profiles were acquired using 0.5–1 keV a Cs^+ ion beam.

Fourier-transform infrared (FTIR) spectroscopy was performed in a side-illuminated single-pass waveguide configuration with a Bruker Vertex 70v spectrometer (Bruker, Ettlingen, Germany) equipped with a helium-flow cryostat (Janis Research company, Woburn, Massachusetts (USA)). The lateral facets of our 2.5 mm long samples were cut at a 70° angle relative to the growth plane, and the top surface close to the QW stack was coated with a metal bilayer (Ti/Au 10 nm/80 nm) [25], to align the electric field of the radiation propagating through the active region almost parallel to the ISB dipole moment (i.e., TM polarized). The dichroic transmission spectra $T(\omega) = T_{\text{TM}}(\omega)/T_{\text{TE}}(\omega)$ were measured, ensuring that polarization-independent spectral features unrelated to ISB transitions were suppressed.

The electronic band structure, electron wave-functions, and ISBT absorption spectra of the investigated samples have been calculated self-consistently, relying on a multivalley effective mass Schrödinger–Poisson solver. A detailed description of the model can be found in Ref. [33].

3 Results and discussion

3.1 Sample design and structural characterization

In biaxially strained high Ge content Si_{1-x} Ge_x alloys ($x > 0.8$), L, Δ_2, and Δ_4 conduction valley minima feature very similar energies whose precise value depends on the Ge content x and on the strain status [34]. By using a multivalley self-consistent code in the parabolic $k{\cdot}p$ envelope function approximation, we have calculated the three conduction band edges $E_c^{L,\Delta_2,\Delta_4}(x)$ as a function of the Ge content x in the 0.8–1 range, assuming that the in-plane lattice parameter is coherent to that of a relaxed $Si_{0.1}$ $Ge_{0.9}$ VS to account for the need of a strain compensation strategy when growing Ge-rich multi-quantum well samples. In Figure 1(a), the L and Δ point band edges as a function of x in the Ge-rich alloys are reported showing that for $x > 0.85$ the conduction band minimum is at L. Consequently, in compositional graded Ge-rich Si_{1-x} Ge_x quantum wells where the Ge content $x = x(z)$ is changed along the growth direction z, the potential $V(z)$ felt by electrons in the well is determined by the L conduction minimum profile $E_c^L(x(z))$

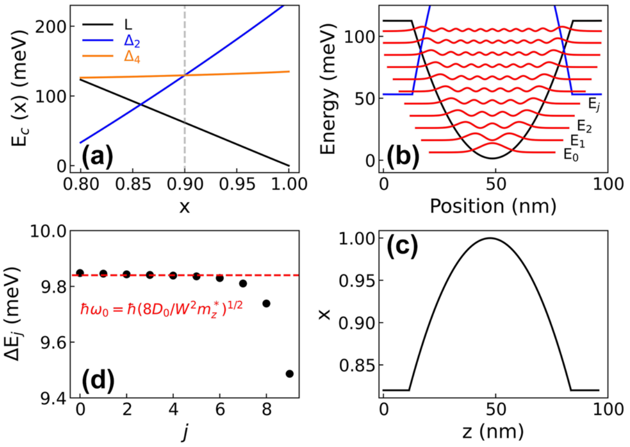

Figure 1: Bandstructure calculations. (a) Conduction band energy at the L, Δ_2, and Δ_4 valley edges as a function of the Ge content x in the alloy at 10 K. The energies are referred to the $E_c^L(1)$ value, set to 0. In the calculation, the in-plane lattice parameter was set equal to that of a relaxed $Si_{0.1}$ $Ge_{0.9}$ VS to account for the need of a strain compensation strategy when growing Ge-rich multi-quantum well samples. In this condition, the Si_{1-x} Ge_x alloy is tensile strained for $x < 0.9$ and compressively strained for $x > 0.9$. Notice that the in-plane tensile strain shifts upward the Δ_2 edge with respect to the Δ_4 one, while the opposite holds for compressive strain. Conversely, the energy of L valleys, being controlled by the hydrostatic component of the strain tensor only, keeps their fourfold degeneracy. (b) Potential $V(z) = E_c^L(x(z))$ (black line) for a PQW having the graded compositional profile shown in panel (c); energy levels E_j and squared wavefunctions of the quantized states (red lines) are also reported. The edge profile at Δ_2, $E_c^{\Delta_2}(x(z))$ (blue line) is also displayed. (c) Ge content x in a PQW as a function of the position along the growth direction z. (d) Energy spacing of subsequent levels $\Delta E_j = E_{j+1} - E_j$.

[34]. The maximum achievable band-offset at L in the range $x = [0.8, 1]$ is 126 meV and in this range $E_c^L(x)$ exhibits a linear behavior. We point out that in our modeling, $E_c^L(x)$ includes nonlinear terms, quadratic contributions being for instance related to the product of the L-point deformation potential with the strain field, since both these two quantities depend linearly on x. Nevertheless, Figure 1(a) indicates that those terms are practically negligible. This is confirmed by the inspection of Figure 1(b) where the potential $V(z) = E_c^L(x(z))$ calculated assuming the parabolic compositional profile of Figure 1(c) (well width $W = 72$ nm and $Si_{0.18}Ge_{0.82}$ barrier layers as in most of our samples) features a quadratic behavior with a depth $D_0 = 112$ meV. It follows, as highlighted in Figure 1(d), that the calculated energy spacing of subsequent levels $\Delta E_j = E_j - E_{j-1}$ is practically constant up to $j = 7$, in good agreement with the spacing expected in an infinite parabolic potential $\hbar\omega_0 = \hbar(8D_0/W^2\ m_z{}^*)^{1/2}$ where $m_z{}^* = 0.13 m_0$ is the electron effective confining mass along the growth direction z. As a final remark, Figure 1(b) shows that the Δ_2 edge profile features a reversed parabolic shape with a minimum in the barrier region where the relative Δ_2 subband states are confined. We point out that in Ge-rich doped QWs, the coupling of Δ_2 states in the barriers with the populated L ones in the wells is negligible, as discussed in Ref. [35].

To investigate the properties of SiGe parabolic quantum wells, we have deposited a series of samples (see Table 1) having a parabolic compositional graded $Si_{1-x(z)}$ $Ge_{x(z)}$ profile ($0.82 < x < 1$), with different well width W and doping levels n_{2D}.

The well width W has been varied in the range 76–46 nm to achieve transition energies in the range 10–20 meV (2.5–5 THz). We deposited a stack of $N_{QW} =$ 20–25 identical wells for an overall thickness of the active region of ~1.5–2 μm. These values have been selected envisioning the embedding of the parabolic QW stacks into microcavities to test the strong coupling limit [36]. As for the doping, we varied the phosphorus concentration in the central part of the barrier in order to tune the electron sheet densities n_{2D} in the $[1 \times 10^{11} - 5 \times 10^{11}]$ cm^{-2} range.

The complete multilayered structure deposited on the Si(001) substrate is sketched in Figure 2(a) and the STEM image acquired on sample 2452 is shown in Figure 2(b). A reverse graded SiGe VS with a final Ge content $y = 0.91$ has been deposited in all the samples. To reach this final Ge content y, two 150 nm thick layers with increasing Si content have been deposited on the Ge buffer layer, as evidenced by the SIMS Ge content profile of the graded region of the virtual substrate and of the first 4 PQWs reported in Figure 2(c). To fulfill the strain-compensation conditions, the thickness of the SiGe barriers in the active region has been varied in order to maintain the average Ge content x_{av} close to 0.91. In our growth conditions, misfit and threading dislocations resulting from plastic relaxation of the Ge buffer and of the SiGe layers are mostly confined in the bottom part of the RG-VS, i.e., in its graded region [27]. The threading dislocation density in the topmost part of the sample has been quantified by Secco etching pit count measurements performed on similar samples [27], being $\sim 3 \times 10^6$ cm^{-2}, a state of the art value for high Ge content SiGe heterostructures deposited on Si substrates.

In Figure 2(d), the P and Ge SIMS content profiles of 4 periods of the active region of a sample featuring $p_{nom} =$ 60 nm and nominally doped with a concentration of phosphorus atoms $N_{3D} = 1 \times 10^{18}$ cm^{-3} in the central 5 nm of the SiGe barriers are reported. The measurements demonstrate that in our growth conditions dopants remain well confined in the barriers with only a slight shift upwards of the P distribution with respect to the barrier center. This is a very important and not trivial achievement due to the P atoms tendency to float on Ge during the growth that could have

Table 1: Structural and optical parameters of the investigated PQW samples. The number N_{QW} of the deposited PQWs, the nominal values of the well width W, the multilayer stack period p_{nom}, the Ge content x_{bar} in the barrier, and the electron sheet density n_{2D} as well as experimental values of the multilayer stack period p_{XRD} and the average Ge content $x_{av}{}^{XRD}$ in the active region as obtained by the XRD data are reported. Experimental values of the absorption energy $\hbar\omega_{abs}$, the FWHM of the absorption peak, and the sheet density $n_{2D}{}^{*}$ as evaluated from the FTIR data acquired at 100 K are also stated.

Sample #	N_{QW}	W (nm)	p_{nom} (nm)	x_{bar} (%)	n_{2D} (cm^{-2})	P_{XRD} (nm)	x_{av}^{XRD} (%)	$\hbar\omega_{abs}$ (meV)	FWHM (meV)	n_{2D}^{*} (cm^{-2})
2452	21	76	90	82	–	88	92.0			
2454	21	74	92	82	2.5×10^{11}	93	91.8			
2456	21	74	92	82	2.5×10^{11}	91	91.7			
2455	21	74	92	82	2.5×10^{11}	92	91.8	10.0	3.0	1.5×10^{11}
2458	21	72	91	82	2.5×10^{11}	90	91.7	10.7	2.1	1.2×10^{11}
2459	21	72	91	82	5×10^{11}	91	91.5	11.8	5.0	3×10^{11}
2460	25	61	76	82	3.7×10^{11}	79	91.2	13.2	5.0	2.8×10^{11}
2354	20	46	62	82	8×10^{11}	62	91.2	19.0	6.2	3.5×10^{11}
2433	25	66	77	84	2.5×10^{11}	78	92.7	10.7	2.3	1.5×10^{11}
2420	25	66	77	84	5×10^{11}	76	92.9	11.8	5.5	3×10^{11}

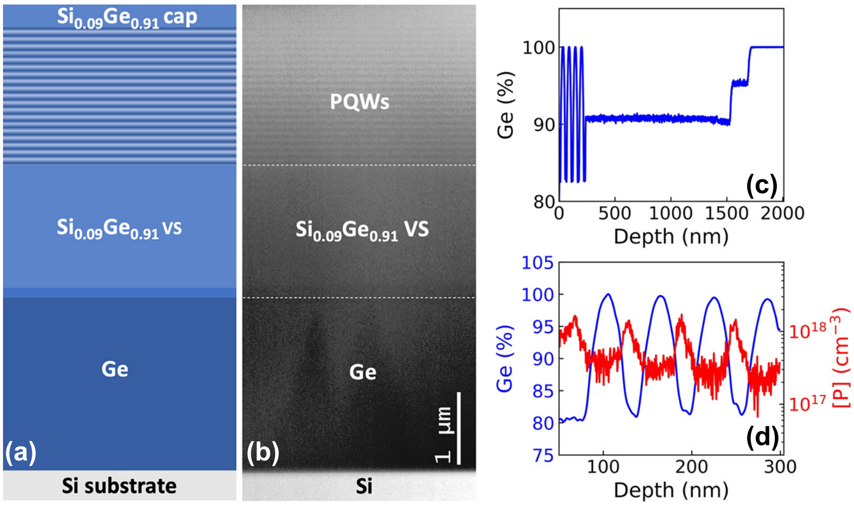

Figure 2: Structural characterization. (a) Sketch of the deposited multilayered structure. (b) STEM image of the 2452 PQW sample. (c) SIMS Ge content profile showing the RG VS region and the first 4 PQWs of the stack. (d) SIMS P and Ge content profiles of 4 periods acquired on a PQW sample with $p_{nom} = 60$ nm. The central 5 nm of the SiGe barriers are doped with a nominal P concentration $N_{3D} = 1 \times 10^{18}$ cm^{-3}.

conflicted with the need of confining donor atoms in the barriers to exploit the unique characteristic of the compensation of electron correlation effects in parabolic QWs.

The structural characterization of the samples has been performed by means of high-resolution STEM and XRD measurements. The data acquired on sample 2452, having a nominal period in the multi-quantum well stack p_{nom} = 90 nm, are reported in Figure 3. In panel (a), the STEM image of 5 periods of the active region of the sample is shown. The resulting intensity profile is in excellent agreement with the parabolic fit, demonstrating the capability of our UHV-CVD reactor in controlling at the nm scale the continuous grading of the SiGe alloy compositional profile. This achievement represents a significant step forward with respect to the previous attempt of growing graded $Si_{1-x}Ge_x$ PQW samples by plasma-enhanced CVD reported in Ref. [30]. The 224 XRD reciprocal space map around asymmetric reflections of the layers is displayed in Figure 3(b). The positions of the VS spots associated to the Ge and the $Si_{0.09}Ge_{0.91}$ layers reveal the presence at room temperature of a tensile strain of about +0.15 %, which can be ascribed to the difference between the coefficients of thermal expansion in Ge and Si [37], [38]. Multiple orders of superlattice (SL) satellites, resulting from the PQW periodicity, that are perfectly vertically aligned to the $Si0_{0.09}Ge_{0.91}$ spot are present in the map, indicating that the entire PQW stack is coherent with the in-plane lattice parameter of the underlying VS. In Figure 3(c), we show the XRD $\vartheta/2\vartheta$ curves around the 004 Ge and 004 Si Bragg peaks together with a simulation curve calculated using the parabolic fit of the STEM image as input for the well compositional profile. The sharp superlattice peaks confirm the high crystalline quality and

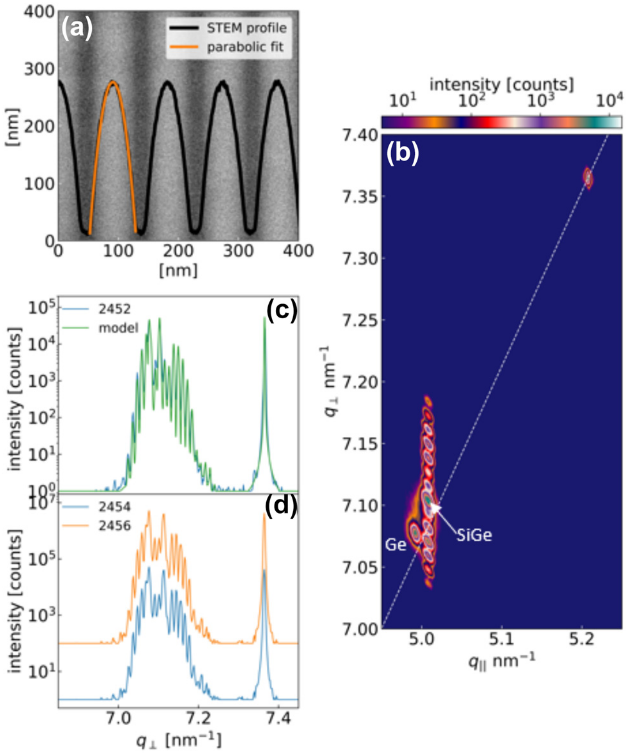

Figure 3: Measure of parabolic concentration profile. (a) STEM image of sample 2452. The intensity profile and its parabolic fit are superimposed on the image. (b) Reciprocal space map of asymmetric 224 reflections of sample 2452. The dashed white line represents the reference values for relaxed $Si_{1-x}Ge_x$ alloys. (c) 004 XRD $\vartheta/2\vartheta$ curve of sample 2452 (blue curve) and dynamical simulation of the curve (green line) calculated assuming the well compositional profile resulting from the parabolic fit of the STEM data reported in (a). (d) 004 XRD rocking curves of samples 2454 and 2456 deposited using identical conditions.

the regular periodicity of the PQWs in the stack. Moreover, the good agreement between XRD data and simulations confirms the parabolic symmetry of the compositional profile over a relatively large area of the sample (~4 mm^2). Finally, the likeness of the XRD $\vartheta/2\vartheta$ curves acquired on two nominally identical samples and reported in Figure 3(d) demonstrates the reproducibility in our reactor of the growth of different samples.

The MQW stack period and the average Ge content in the stack measured by XRD on all the investigated samples are reported in Table 1. A very good agreement with respect to the nominal values has been found demonstrating once more the control acquired in the deposition process.

3.2 Optical properties of doped $Si_{1-x}Ge_x$ PQWs

Intersubband transition absorption spectra have been measured on a subset of the doped samples of Table 1. The linear dichroic spectra have been acquired at different temperatures in the energy range where intersubband transitions are expected from numerical calculations. Although in this region several absorption lines are observed in the *TM* and *TE* spectra, the dichroic transmission signal is characterized in all the investigated samples by a single pronounced dip, which is due to a reduced transmission of the TM mode and which monotonically blue-shifts upon decreasing the well width (see Figure 4). Following the procedure reported in Ref. [33], the dimensionless single well absorption coefficient $\alpha_{2D}(E)$ has been determined and the central absorption energy $\hbar\omega_{abs}$, the full width half maximum FWHM of the absorption peak, and the electron sheet density $n_{2D}{}^*$ are

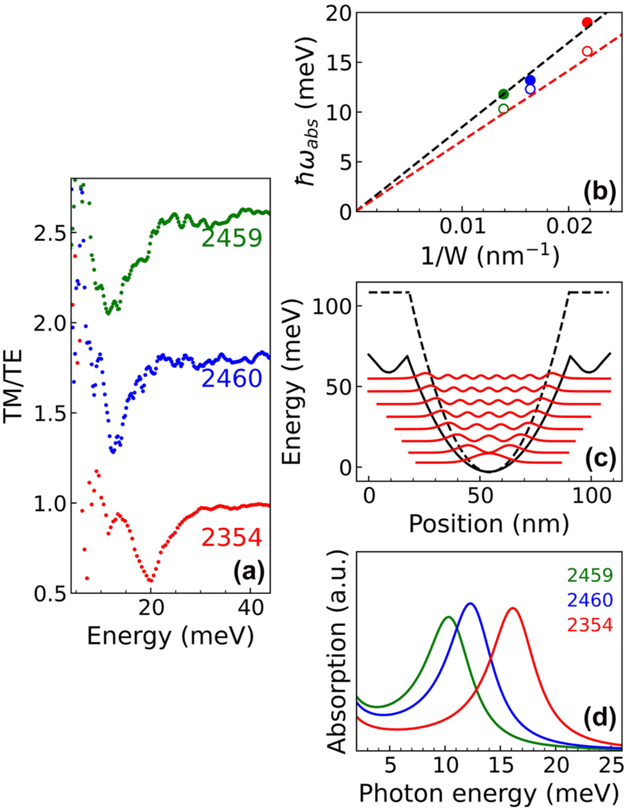

Figure 4: Terahertz spectroscopy measurements. (a) Dichroic transmission spectra acquired at 100 K of samples 2459, 2460, and 2354 having an electron sheet density ~3×10^{11} cm^{-2} and well width 72 nm, 61 nm, and 46 nm, respectively. (b) Experimental (full circles) and theoretical (open circles) absorption energies as a function of W^{-1}. Black dashed line represents the linear fit of the experimental data and the red dashed line the parabolic bare energy behavior $\hbar\omega_0(W) = \hbar(8\mathbf{D_0}/m_z{}^*)^{1/2}/W$. (c) Potential $V(z)$ (continuous black line) for sample 2459 along the growth direction; energy levels E_j and squared wavefunctions of the quantized states are also reported; the potential calculated for an undoped PQWs with the same shape is displayed as a dashed black line. The two potential curves have been aligned in energy at their minimum: (d) Theoretical absorption spectra for the samples in panel (a).

extracted by fitting the resulting $\alpha_{2D}(E)$ spectrum with a Lorentzian curve. The values estimated from the experimental data acquired at 100 K on all the measured samples are reported in Table 1.

We point out that the absolute values of both nominal (n_{2D}) and measured ($n_{2D}{}^{*}$) sheet densities are affected by a relative error of ∼30 %, due to the difficulties of a precise calibration of the N_{3D} phosphorus concentration confined in very thin doped layers, and to the uncertainty in the evaluation of the single well absorbance from the FTIR dichroic spectra acquired in multilayered samples with the side-illuminated single-pass waveguide configuration [1]. However, since the same doping procedure and FTIR data analysis have been used systematically, the *relative* variations of both n_{2D} and $n_{2D}{}^{*}$ among different samples are much more accurate. Despite these uncertainties, the fact that $n_{2D}{}^{*}$ values are always lower than the n_{2D} ones may be due to the small energy difference between donor levels originating from the Δ_2 edge states confined in the tensile strained SiGe barriers and the fundamental L subband state in the well, which can limit the effectiveness of the transfer doping mechanism [33]. Interestingly, the largest difference between n_{2D} and $n_{2D}{}^{*}$ is observed in sample 2354 which, having the thickest barrier, features the lowest energy difference between the fundamental L subband state and the Δ_2 donor level.

The low temperature dichroic transmission spectra of samples 2459, 2460, and 2354 having different well width and comparable electron sheet densities in the well $n_{2D}{}^{*} \sim 3 \times 10^{11}$ cm^{-2} are reported in Figure 4(a). As expected, the transmission dip energy blue-shifts by decreasing the well width W. As shown in Figure 4(b), the dependence of the measured absorption energy $h\omega_{abs}$ (full circles) on $1/W$ follows the typical linear behavior foreseen for electron ISBTs in a harmonic potential. The electronic band structure and the absorption spectra of the samples have been calculated self-consistently. In modulation doped samples, the electrostatic (Hartree) charge effects influence the L band profile decreasing the depth of the effective potential felt by electrons as shown in Figure 4(c), where the effective potential profile, the electron energy levels, and the square modulus of the wavefunctions calculated for sample 2459 at 10 K are reported. The bare potential calculated for an undoped PQW with the same compositional profile is also reported for comparison. The simulated absorption spectra of the three samples are displayed in Figure 4(d). Estimated absorption energies in Figure 4(b) (open symbol) have been calculated correcting the subband transition energy, obtained considering the Hartree potential, to account for the depolarization shift effect, following Ref. [39]. Minor contributions stemming from band nonparabolicity and other many-body effects have been neglected. The shrinking of the energy level separation due to the Hartree potential is compensated by the depolarization shift so that the calculated absorption energies result in good agreement with the bare harmonic energy $\hbar\omega_0$ (red dashed line). However, the theoretical energies are slightly smaller with respect to the experimental data suggesting that the ratio D_0/m_z could be slightly underestimated in our simulations.

In Figure 5 the dichroic transmission spectra as a function of temperature of samples 2433 and 2420 having the same well profile but different doping ((a) $n_{2D}{}^{*} \sim 1.5 \times 10^{11}$ cm^{-2}, (b) $n_{2D}{}^{*} \sim 3 \times 10^{11}$ cm^{-2}) are reported. The transmission dips in these two samples are practically at same energy, the one featuring the larger carrier density being blueshift by 1 meV only. Remarkably, we find that in each sample the absorption energy is almost temperature independent despite in this THz range the subband population strongly depends on T. As already pointed out, this is a unique “fingerprint” of parabolic quantum wells, whose absorption energy is independent on the distribution of electron in subbands. This contrasts with terahertz ISB absorption in square QWs, where the lineshape and peak absorption energy vary with temperature [40]. Consistently, we have observed a significant variation of the ISB absorption spectrum with temperature when the PQWs is directly doped in the well, since in this case the cancellation of electron correlation effects does not occur [31].

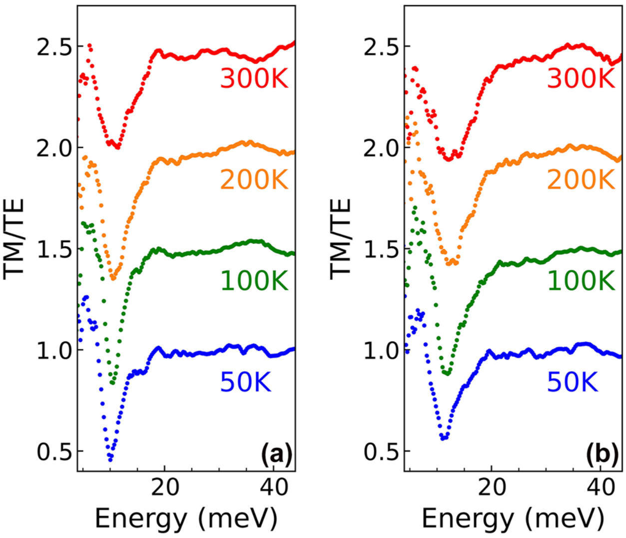

Figure 5: Dichroic transmission spectra acquired at different temperatures for two samples with the same well profile but different doping. (a) Sample 2433 with $n_{2D}{}^{*} \sim 1.5 \times 10^{11}$ cm^{-2}. (b) Sample 2420 with $n_{2D}{}^{*} \sim 3 \times 10^{11}$ cm^{-2}.

The main difference between the spectra of the two samples of Figure 5 is the increased linewidth observed at higher doping: in sample 2433 ($n_{2D}{}^* \sim 1.5 \times 10^{11}$ cm^{-2}), a narrow FWHM of about 2.3 meV has been measured at 100 K, increasing to 5 meV at 300 K. On the contrary, sample 2420 ($n_{2D}{}^* \sim 3 \times 10^{11}$ cm^{-2}) shows a FWHM ∼ 5.5 meV, almost constant with temperature. As shown in Table 1 where the FWHM at 100 K of all the investigated samples are reported, FWHMs ∼ 2 meV and ∼ 5 meV are typical values for these doping levels, independently on the well width and absorption energy. The observed increase of the linewidth as a function of the electron sheet density is in good agreement with previous results obtained in rectangular quantum wells. Interestingly, we notice that the values here reported at low doping are sensitively smaller with respect to those previously measured in rectangular Ge/SiGe QWs [41] typically featuring FWHM slightly larger than 4 meV. This effect may be attributed to a reduction of the scattering associated to the interface roughness occurring in systems without sharp interfaces.

The linewidth analysis, we performed with square QWs samples in [41] highlighted the presence of a non-negligible contribution of about 1–2 meV to the total width, attributed to structural crystal defects brought about by the fraction of treading defects which, overcoming the RG-VS region, penetrates in the QWs one. Although the crystalline quality of the SiGe heteroepitaxy in our reactor has been significantly improved in the last few years [27], the same mechanism can affect the lineshape of the PQW spectra here investigated, resulting in larger low temperature FWHM values with respect to III–V ones [19]. Considering the superior capability of achieving a sharp delta-like donor profile in III–V heteroepitaxy, also the spatial broadening of the P concentration along the growth direction, associated to the surface kinetics of donor atoms in the SiGe environment, can contribute to the enlargement of the absorption peak. We point out here that, in order to achieve a high filling factor of quantum wells in the stack, barrier thicknesses <18 nm have been deposited in our samples. We believe that the narrowness of the absorption resonance of $Si_{1-x}Ge_x$ PQW samples could be improved by depositing thicker barriers and decreasing the growth temperature during the phosphine codeposition step, so to increase the spacer layer thickness between the doped region and the well [40]. Finally, we notice that in III–V QWs, a larger temperature dependence of the linewidth has been observed, so that the two material systems exhibit more similar value of the FWHM/E_{abs} ratio at room temperature [31].

The absorption spectra of our PQWs represent a promising starting point to achieve and investigate strong radiation-matter coupling in this technologically relevant material system. Following Ref. [8], [42], [43], in a photon cavity of thickness L_{cav} with a stack of N_{QW} PQWs doped with an electron sheet density n_{2D}, the intersubband polariton energy splitting $E_{\text{up-down}}$ at the matching condition $\omega_0 = \omega_{cav}$ is:

$$E_{\text{up - down}} == 2\hbar\Omega_R = \hbar\sqrt{\frac{e^2 f N_{QWn_{2D}}}{\varepsilon\varepsilon_0 m_z^* L_{\text{cav}}}}.$$

Therefore, using an oscillator strength value $f = 1$, $L_{\text{cav}} = 2$ μm and $N_{\text{QW}} = 25$, $n_{2D} = 2 \times 10^{11}$ cm^{-2}, as in our samples, we estimate an ISB polariton energy splitting $E_{\text{up-down}} \sim 5$ meV and a strength ratio $\eta = \frac{\Omega_R}{\omega_0} \sim 0.2$ at 2.5 THz, well within the ultra-strong coupling regime. This estimated splitting value, which is larger than the measured FWHM, make feasible the future demonstration of ISB polaritons in Ge-rich PQWs.

Different approaches have been pursued to realize optical cavities aimed at the observation of the strong coupling regime with ISBTs. Most of them rely on lithographic patterning of metal structures directly on the epitaxial wafer, with or without etching the surrounding material. It is well known that the most important constraint in the comparison of different cavity designs is related to the dipole orientation, which requires a radiative electric field with polarization orthogonal to the quantum well plane. A second important parameter is the cavity volume that must be small, possibly subwavelength sized. To meet these requirements, the active region is usually placed within nondispersive metal–insulator–metal (MIM) microresonators, which are typically fabricated with the substrate-transfer technique. Among them, we mention the one-dimensional periodic grating [36], the capacitor-inductor cavities of Ref. [11], [18], [44], and the patch-antenna cavity discussed in Ref. [43], where the extension of the cavity in the vertical direction is accompanied by a small volume and a totally vertical and homogeneous electric field. The implementation of the substrate transfer technique is more complicated in SiGe epitaxial layers with respect to III–V materials, because of the difficulties related to the material-selective etching processes and owing to the lattice strain (thermal and epitaxial) featured by SiGe heterostructures. Planar microcavities relying, e.g., on deep-etched split-ring resonators, previously realized for III–V materials [45], are not efficient in the SiGe case due to the presence of the thick Ge virtual substrate with high dielectric constant that traps most of the electromagnetic energy density in an inactive layer. The solution may come again from epitaxy: while noble metals such as gold or aluminum have almost always been used for the cavity mirrors, in the THz range it is also possible to employ epitaxially grown, heavily doped degenerate semiconductors as substitutes for the metal layers. Indeed, the complex dielectric function of n-Ge with $n > 10^{19}$ cm^{-3}, measured in [46], indicates that a reflectivity $R \sim 1$ can be achieved up to the mid-IR. For example, a plasma edge at 30 THz has been observed in epitaxial n-Ge with activated electron densities $\sim 2 \times 10^{19}$ cm^{-3} and used to produce all-semiconductor nanoantennas [47]. We thus suggest that THz ISB polariton with SiGe PQWs can be demonstrated avoiding the substrate-transfer procedure and leveraging on a plasmonic-conductor ground plane below the quantum well stack, realized P-doping at $\sim 2 \times 10^{19}$ cm^{-3} the $Si_{0.09}Ge_{0.91}$ VS layer.

4 Conclusions

High quality n-doped Ge-rich $Si_{1-x}Ge_x$ graded PQW samples have been designed, grown, and structurally and optically characterized. The SIMS, XRD, and STEM analysis demonstrate the high degree of control at the nanometer scale of the employed UHV-CVD reactor over the deposited compositional profile and the high reproducibility of the growth over the whole active region of the multilayered structure.

The intersubband absorption spectra display a sharp single-value resonance in the 2.5–5 THz range, fairly independent from doping and temperature, and inversely proportional to the well width, as expected for an harmonic potential. The observed absorption features are in good agreement with numerical calculations, evidencing that the significative shrinking of the energy levels due to the Hartree potential is compensated mainly by the energy blue-shift induced by the depolarization effect. A coupling strength ratio $\eta = \frac{\Omega_R}{\omega_0} \sim 0.2$ at $\omega_0 = 2.5$ THz, i.e., well within the ultra-strong coupling regime, has been estimated. We thus believe that SiGe parabolic quantum well, combined with THz optical cavities, can enable the exploration of the ultra-strong light–matter coupling limit in a silicon-based, CMOS foundry-compatible material platform, possibly operating at room temperature, opening new routes for the exploitation of these exotic quantum states in novel mainstream electronic devices.

Research funding: Regione Lazio, program POR FESR 2014–2020, project no. A0375-2020-36579, by the Rome Technopole Foundation (CUP F83B22000040006), by Grant of Excellence Departments, MUR (ARTICOLO 1, COMMI 314–337 LEGGE 232/2016) to Department of Science, Roma Tre University, and by Italian Ministerial grant PRIN 2022 “Strong light-matter coupling manipulation in SiGe quantum wells at terahertz frequencies” CUP F53D23001190006.

Author contributions: All authors have accepted responsibility for the entire content of this manuscript and approved its submission.

Conflict of interest: Authors state no conflicts of interest.

Informed consent: Informed consent was obtained from all individuals included in this study.

Ethical approval: The conducted research is not related to either human or animals use.

Data availability: The datasets generated and/or analyzed during the current study are available from the corresponding author upon reasonable request.

References

[1] M. Helm, “Chapter 1 the basic physics of intersubband transitions,” *Semicond. Semimetals*, vol. 62, pp. 1—99, 1999.

[2] H. Schneider and H. C. Liu, “Quantum well infrared photodetectors: physics and applications,” in *Springer Series in Optical Sciences, No. 126*, Berlin, New York, Springer, 2007.

[3] D. Palaferri, *et al*., “Patch antenna terahertz photodetectors,” *Appl. Phys. Lett.*, vol. 106, no. 16, p. 161102, 2015.

[4] J. Faist, F. Capasso, D. L. Sivco, C. Sirtori, A. L. Hutchinson, and A. Y. Cho, “Quantum cascade laser,” *Science*, vol. 264, no. 5158, pp. 553—556, 1994.

[5] M. S. Vitiello, G. Scalari, B. Williams, and P. De Natale, “Quantum cascade lasers: 20 years of challenges,” *Opt. Express*, vol. 23, no. 4, p. 5167, 2015.

[6] J. Faist, *Quantum Cascade Lasers*, 1st ed. Oxford, United Kingdom, Oxford University Press, 2013.

[7] W. Kohn, “Cyclotron resonance and de Haas-van Alphen oscillations of an interacting electron gas,” *Phys. Rev.*, vol. 123, no. 4, pp. 1242—1244, 1961.

[8] C. Ciuti, G. Bastard, and I. Carusotto, “Quantum vacuum properties of the intersubband cavity polariton field,” *Phys. Rev. B*, vol. 72, no. 11, p. 115303, 2005.

[9] D. Dini, R. Köhler, A. Tredicucci, G. Biasiol, and L. Sorba, “Microcavity polariton splitting of intersubband transitions,” *Phys. Rev. Lett.*, vol. 90, no. 11, p. 116401, 2003.

[10] P. Forn-Díaz, L. Lamata, E. Rico, J. Kono, and E. Solano, “Ultrastrong coupling regimes of light-matter interaction,” *Rev. Mod. Phys.*, vol. 91, no. 2, p. 025005, 2019.

[11] M. Geiser, F. Castellano, G. Scalari, M. Beck, L. Nevou, and J. Faist, “Ultrastrong coupling regime and plasmon polaritons in parabolic semiconductor quantum wells,” *Phys. Rev. Lett.*, vol. 108, no. 10, p. 106402, 2012.

[12] A. A. Anappara, A. Tredicucci, G. Biasiol, and L. Sorba, “Electrical control of polariton coupling in intersubband microcavities,” *Appl. Phys. Lett.*, vol. 87, no. 5, p. 051105, 2005.

[13] A. A. Anappara, A. Tredicucci, F. Beltram, G. Biasiol, and L. Sorba, “Tunnel-assisted manipulation of intersubband polaritons in asymmetric coupled quantum wells,” *Appl. Phys. Lett.*, vol. 89, no. 17, p. 171109, 2006.

[14] S. Rajabali, *et al*., “An ultrastrongly coupled single terahertz meta-atom,” *Nat. Commun.*, vol. 13, no. 1, p. 2528, 2022.

[15] J. Raab, *et al*., “Ultrafast terahertz saturable absorbers using tailored intersubband polaritons,” *Nat. Commun.*, vol. 11, no. 1, p. 4290, 2020.

[16] M. Malerba, *et al*., “Detection of strong light—matter interaction in a single nanocavity with a thermal transducer,” *ACS Nano*, vol. 16, no. 12, pp. 20141—20150, 2022.

[17] R. Colombelli and J.-M. Manceau, “Perspectives for intersubband polariton lasers,” *Phys. Rev. X*, vol. 5, no. 1, p. 011031, 2015.

[18] P. Goulain, C. Deimert, M. Jeannin, “THz ultra-strong light—matter coupling up to 200 K with continuously-graded parabolic quantum wells,” *Adv. Opt. Mater.*, vol. 11, no. 9, p. 2202724, 2023.

[19] C. Deimert, *et al*., “Realization of harmonic oscillator arrays with graded semiconductor quantum wells,” *Phys. Rev. Lett.*, vol. 125, no. 9, p. 097403, 2020.

[20] I. A. Fischer, *et al*., “On-chip infrared photonics with Si-Ge-heterostructures: what is next?” *APL Photonics*, vol. 7, no. 5, p. 050901, 2022.

[21] G. Scappucci, *et al*., “The germanium quantum information route,” *Nat. Rev. Mater.*, vol. 6, no. 10, pp. 926—943, 2020.

[22] Y. Bogumilowicz, *et al*., “High Ge content Si/SiGe heterostructures for microelectronics and optoelectronics purposes,” *Proc. — Electrochem. Soc.*, vol. 7, pp. 665—679, 2004.

[23] D. J. Paul, “The progress towards terahertz quantum cascade lasers on silicon substrates: progress towards THz QCLs on Si substrates,” *Laser Photonics Rev.*, vol. 4, no. 5, pp. 610—632, 2010.

[24] T. Grange, *et al*., “Room temperature operation of *n* -type Ge/SiGe terahertz quantum cascade lasers predicted by non-equilibrium Green’s functions,” *Appl. Phys. Lett.*, vol. 114, no. 11, p. 111102, 2019.

[25] K. Ismail, J. O. Chu, K. L. Saenger, B. S. Meyerson, and W. Rausch, “Modulation-doped *n* -type Si/SiGe with inverted interface,” *Appl. Phys. Lett.*, vol. 65, no. 10, pp. 1248—1250, 1994.

[26] C. Ciano, *et al*., “Control of electron-state coupling in asymmetric Ge/Si—Ge quantum wells,” *Phys. Rev. Appl.*, vol. 11, no. 1, p. 014003 2019.

[27] E. T. Simola, *et al*., “Subnanometer control of the heteroepitaxial growth of multimicrometer-thick Ge/Si-Ge quantum cascade structures,” *Phys. Rev. Appl.*, vol. 19, no. 1, p. 014011, 2023.

[28] T. Grange, *et al*., “Atomic-scale insights into semiconductor heterostructures: from experimental three-dimensional analysis of the interface to a generalized theory of interfacial roughness scattering,” *Phys. Rev. Appl.*, vol. 13, no. 4, p. 044062, 2020.

[29] D. Stark, *et al*., “THz intersubband electroluminescence from n-type Ge/SiGe quantum cascade structures,” *Appl. Phys. Lett.*, vol. 118, no. 10, p. 101101, 2021.

[30] A. Ballabio, *et al*., “Ge/SiGe parabolic quantum wells,” *J. Phys. D: Appl. Phys.*, vol. 52, no. 41, p. 415105, 2019.

[31] M. Montanari, *et al*., “THz intersubband absorption in n-type Si1— *x* Ge *x* parabolic quantum wells,” *Appl. Phys. Lett.*, vol. 118, no. 16, p. 163106, 2021.

[32] G. Capellini, *et al*., “Strain relaxation in high Ge content SiGe layers deposited on Si,” *J. Appl. Phys.*, vol. 107, no. 6, p. 063504, 2010.

[33] Y. Busby, *et al*., “Near- and far-infrared absorption and electronic structure of Ge-SiGe multiple quantum wells,” *Phys. Rev. B*, vol. 82, no. 20, p. 205317, 2010.

[34] M. Virgilio and G. Grosso, “Type-I alignment and direct fundamental gap in SiGe based heterostructures,” *J. Phys.: Condens. Matter*, vol. 18, no. 3, pp. 1021—1031, 2006.

[35] M. Ortolani, *et al*., “Long intersubband relaxation times in n-type germanium quantum Wells,” *Appl. Phys. Lett.*, vol. 99, no. 20, p. 201101, 2011.

[36] Y. Todorov, *et al*., “Optical properties of metal-dielectric-metal microcavities in the THz frequency range,” *Opt. Express*, vol. 18, no. 13, p. 13886, 2010.

[37] G. Capellini, M. De Seta, P. Zaumseil, G. Kozlowski, and T. Schroeder, “High temperature x ray diffraction measurements on Ge/Si(001) heterostructures: a study on the residual tensile strain,” *J. Appl. Phys.*, vol. 111, no. 7, p. 073518, 2012.

[38] C. L. Manganelli, *et al*., “Temperature dependence of strain—phonon coefficient in epitaxial Ge/Si(001): a comprehensive analysis,” *J. Raman Spectrosc.*, vol. 51, no. 6, pp. 989—996, 2020.

[39] W. P. Chen, Y. J. Chen, and E. Burstein, “Interface EM modes of a “surface quantized” plasma layer on a semiconductor surface,” *Surf. Sci.*, vol. 58, no. 1, pp. 263—265, 1976.

[40] M. De Seta, *et al*., “Narrow intersubband transitions in n-type Ge/SiGe multi-quantum wells: control of the terahertz absorption energy trough the temperature dependent depolarization shift,” *Nanotechnology*, vol. 23, no. 46, p. 465708, 2012.

[41] M. Virgilio, D. Sabbagh, M. Ortolani, L. Di Gaspare, G. Capellini, and M. De Seta, “Physical mechanisms of intersubband-absorption linewidth broadening in s -Ge/SiGe quantum wells,” *Phys. Rev. B*, vol. 90, no. 15, p. 155420, 2014.

[42] M. Geiser, *et al*., “Strong light-matter coupling at terahertz frequencies at room temperature in electronic LC resonators,” *Appl. Phys. Lett.*, vol. 97, no. 19, p. 191107, 2010.

[43] Y. Todorov, *et al*., “Polaritonic spectroscopy of intersubband transitions,” *Phys. Rev. B*, vol. 86, no. 12, p. 125314, 2012.

[44] L. Masini, *et al*., “Continuous-wave laser operation of a dipole antenna terahertz microresonator,” *Light: Sci. Appl.*, vol. 6, no. 10, pp. e17054, 2017.

[45] D. Dietze, A. M. Andrews, P. Klang, G. Strasser, K. Unterrainer, and J. Darmo, “Ultrastrong coupling of intersubband plasmons and terahertz metamaterials,” *Appl. Phys. Lett.*, vol. 103, no. 20, p. 201106, 2013.

[46] J. Frigerio, *et al*., “Tunability of the dielectric function of heavily doped germanium thin films for mid-infrared plasmonics,” *Phys. Rev. B*, vol. 94, no. 8, p. 085202, 2016.

[47] L. Baldassarre, *et al*., “Midinfrared plasmon-enhanced spectroscopy with germanium antennas on silicon substrates,” *Nano Lett.*, vol. 15, no. 11, pp. 7225—7231, 2015.

4

ULTRASTRONG COUPLING OF $\mathrm{SI}_{1-x}\mathrm{GE}_x$ PARABOLIC QUANTUM WELLS TO TERAHERTZ MICROCAVITIES

The control and manipulation of quantum states through their interaction with light is an area of research of growing importance because of its potential technological applications [5]. A central aspect of this field is the observation of the *strong coupling* regime between light and matter in semiconductor devices [6]. This regime, as discussed in Section 1.6, emerges when a quantum two-level system with transition energy $\hbar\omega_0$ is placed inside an optical cavity with a resonant photonic mode with frequency ω_c. From an experimental point of view, strong coupling is identified through the observation of the dispersion of the polaritonic bands as a function of the detuning, $\omega_0 - \omega_c$. The characteristic *anticrossing* behavior between light and matter resonances makes it possible to quantify the coupling strength by measuring the frequency separation between the upper and lower polaritonic bands, which is equal to twice the Rabi frequency ($2\Omega_R$) at zero detuning.

Semiconductor microcavities fabricated by lithography are particularly advantageous due to their reproducibility, scalability, and potential operability at room temperature. Traditionally, strong coupling in the THz domain has been achieved using two-dimensional electron gasses (2DEGs) embedded in metal-insulator-metal optical cavities, whose schematic representation is shown in the Figure 1.16, based on III-V compound semiconductors [31]. The intersubband transitions (ISBTs) in 2DEGs exhibit a collectively enhanced light-matter interaction, such that the normalized coupling ratio, Ω_R/ω_0, scales with the two-dimensional electron density, n_{2D}. The *ultrastrong coupling* regime is achieved when $\Omega_R/\omega_0 > 0.1$.

The goal of this research was to explore the possibility of reaching the ultrastrong coupling regime between the states of the conduction subbands in $\mathrm{Ge/Si}_{1-x}\mathrm{Ge}_x$ heterostructures coupled to cavities operating in the THz domain. For this purpose, hybrid metal-plasmonic THz patch-antenna microcavities were used [31]. A fundamental step toward full compatibility with silicon technology consists of replacing the bottom metal mirror with a heavily doped semiconductor (n^{++}-SiGe), which acts as a plasmonic mirror [52].

The complex dielectric function of the doped semiconductor film, $\varepsilon(\omega) = \varepsilon_1(\omega) + i\varepsilon_2(\omega)$, is described by the Drude-Lorentz model. However, in the case of high doping, the behavior becomes metallic; such as that employed for the SiGe layer, the response can be effectively approximated by the Drude model. In this approximation, the influence of interband transitions is included, as they contribute to the background optical response of the crystal lattice. This leads to an effective high-frequency dielectric constant, ε_∞^* [52].

The behavior of the doped semiconductor is characterized by two plasma frequencies: the unscreened, ω_p, and the screened plasma, ω^*, frequencies. The first term, ω_p is defined as:

$$\omega_p = \sqrt{\frac{n_p e^2}{\varepsilon_0 m^*}} \tag{4.1}$$

where n_p is the carrier density, and m^* is the effective mass. Instead, the screened plasma frequency represents the maximum frequency at which the material exhibits metallic behavior, more precisely when $\text{Re}[\varepsilon(\omega)] = 0$, thus defining the material's *plasma edge*. Taking into account both the dielectric screening, ε_∞^*, and the Drude scattering rate γ_D, ω^* can be calculated more accurately as:

$$\omega^* = \sqrt{\frac{\omega_p^2}{\varepsilon_\infty^*} - \gamma_D^2} \tag{4.2}$$

This approach simplifies the fabrication process and makes it possible to integrate the mirror directly into the material during epitaxial growth. The microcavities were then defined by ion etching, while the top mirror was obtained by depositing a thin gold layer on the surface of the samples. The result is an integrated system that includes microcavities fabricated through an efficient process designed to overcome the technological challenges typical of the materials employed.

In my thesis work, I focused on optimizing the back mirror of the THz cavity by replacing the metallic mirror with highly doped SiGe. To this end, a series of Si(100)/Ge/SiGe samples was grown, as described in Section 2.1, with the last 2 μm of SiGe heavily doped to act as a plasmonic mirror. The layout of these samples is shown in Figure 4.1a, while the different doping values are listed in Table 4.1. Note that the n_p values given in the table represent the activated donors, which do not necessarily coincide with the nominal concentration of donors introduced during growth due to phosphorus segregation phenomena and other effects that reduce their activation, especially at high doping levels. First, room-temperature reflectivity measurements were performed on a series of virtual substrates characterized by different P contents to determine the doping level required to obtain the desired ω^*, which is necessary for the strong-coupling experiment. Figure 4.1b shows the changes in the reflectivity of substrates with different P concentrations. For wavelength $\lambda < 750$, the metallic component increases with increasing P content; the values of ω_p and ω^* are reported in table 4.1.

n_p [cm^{-3}]	ω_p [THz]	ω^* [THz]
$2.8 \cdot 10^{18}$	31.2	7.8
$7.5 \cdot 10^{18}$	72.2	18.0
$1.4 \cdot 10^{19}$	96.0	24.0

Table 4.1: *Values of ω^* and ω_p for different P concentrations in the VS.*

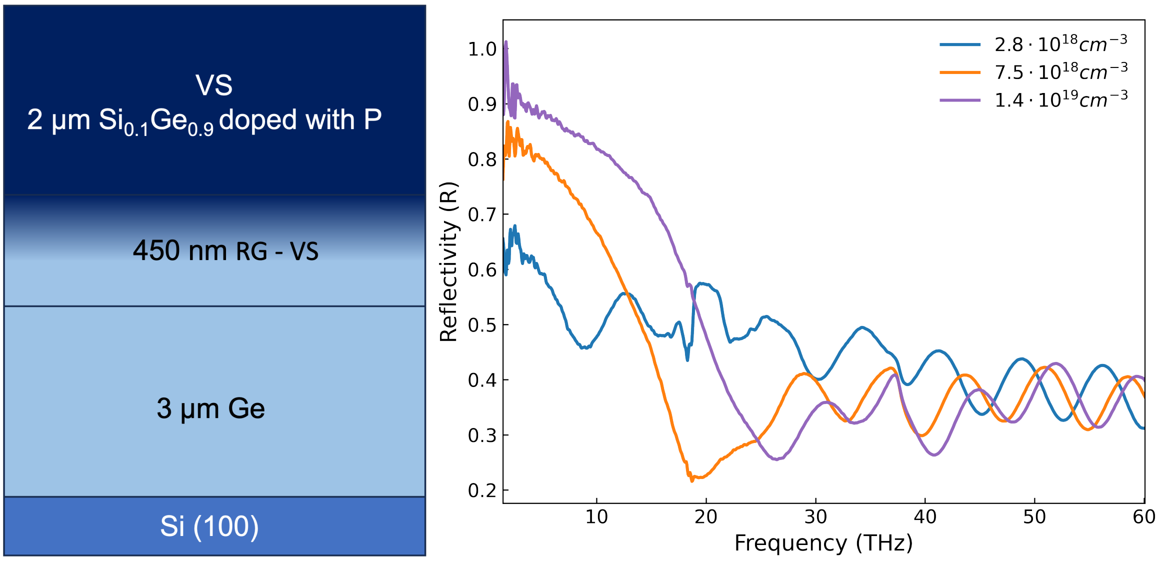

Figure 4.1: *(a) Schematic representation of the VS of heavily doped SiGe to function as a plasmonic mirror. (b) Variation of the substrate reflectivity as a function of the doping level in the SiGe layer. As the donor concentration increases, the plasma frequency shifts toward higher energies, allowing the layer to be used as a metallic mirror inside the microcavity.*

To demonstrate the formation of ISB polaritons, a sample consisting of parabolic quantum wells in $Si_{1-x}Ge_x$ was used, with well thicknesses of 61 nm and 16 nm barriers, nominally n-type doped with a concentration $n_{3D} = 8 \cdot 10^{17}$ cm^{-3} in the central part of each barrier and characterized by an ISB transition at 3 THz. The structure was grown on a doped layer with a concentration of $N_d = 1.0 \cdot 10^{19}$ cm^{-3} and a thickness of 2 μm. The cavities were fabricated at the CNR Institute of Photonics and Nanotechnology.

The experimental results demonstrate the achievement of the ultrastrong coupling regime. An anticrossing was observed around 3 THz, with a $\Omega_R = 0.68 \pm 0.05$ THz and a normalized ratio $\Omega_R/\omega_0 \simeq 0.2$, which confirms entry into the ultrastrong regime. The coupling remains stable up to room temperature, with an almost constant ratio $\Omega_R/\omega_0 \sim 0.2$ between 10 K and 300 K. This thermal stability is attributed to the weak electron-phonon interaction typical of the nonpolar lattices of group-IV (SiGe) semiconductors, in sharp contrast to III-V materials. The reduction in the Q-factor with increasing temperature is due to the broadening of the ISBT line, caused by enhanced electron-phonon scattering, and to the increase in losses in the doped SiGe mirror, which becomes more dissipative. Taken together, these effects broaden the polaritonic branches, while the energy of the ISBT remains essentially unchanged.

These results open new perspectives for the use of the $\mathrm{Si}_{1-x}\mathrm{Ge}_x$ platform, both in the fundamental study of ultrastrong light-matter coupling and in the development of ultrafast modulators and saturable absorbers operating in the THz range. The CMOS compatibility of SiGe PQWs and the size of the patch antennas suitable for modern microelectronic processes make it realistic to integrate quantum photonic devices with silicon-based electronic circuits.

Ultrastrong Coupling of $Si_{1-x}Ge_x$ Parabolic Quantum Wells to Terahertz Microcavities

Fritz Berkmann[1], Tommaso Venanzi[1], Leonetta Baldassarre[1], Elena Campagna[2], Enrico Talamas Simola[2], Luciana Di Gaspare[2], Cedric Corley-Wiciak[3,4], Giovanni Capellini[2,3], Giuseppe Nicotra[5], Gianfranco Sfuncia[5], Andrea Notargiacomo[6], Ennio Giovine[6], Sara Cibella[6], Michele Virgilio[7], Giacomo Scalari[8], Monica De Seta[2], and Michele Ortolani[*1]

[1]*Department of Physics, Sapienza University of Rome, Rome, Italy*
[2]*Department of Science, Roma Tre University, Rome, Italy*
[3]*IHP - Leibniz-Institut für innovative Mikroelektronik, Frankfurt(Oder), Germany*
[4]*European Synchrotron Radiation Facility, Grenoble Cedex 9, France*
[5]*Institute for Microelectronics and Microsystems IMM-CNR, Catania, Italy*
[6]*Institute for Photonics and Nanotechnologies IFN-CNR, Rome, Italy*
[7]*Department of Physics, University of Pisa, Pisa, Italy*
[8]*Institute of Quantum Electronics, Eidgenössische Technische Hochschule Zürich, Switzerland*

Keywords: *Strong Coupling, Parabolic Quantum wells, SiGe Epitaxy, THz Spectroscopy, Light-Matter interaction*

Abstract

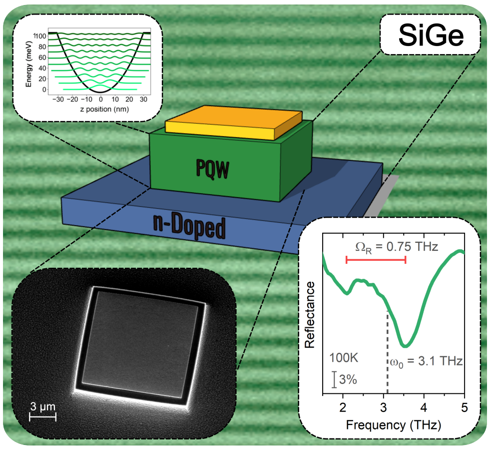

Control and manipulation of quantum states by light is increasingly important for both fundamental research and applications.This can be achieved through the strong coupling between light and semiconductor devices, typically observed at THz frequencies in 2D electron gases embedded in lithographic optical cavities. Here we explore the possibility of achieving ultrastrong coupling between conduction sub-band states in $Si_{1-x}Ge_x$ heterostructures and THz cavity photons fabricated with a potentially silicon-CMOS-compliant process. We developed $Si_{1-x}Ge_x$ parabolic quantum wells with transition at $\omega_0 = 3.1$ THz and hybrid metal-plasmonic THz patch-antenna microcavities resonating between 2 and 5 THz depending on the antenna length. In this first demonstration we achieved anti-crossing around 3 THz with spectroscopically measured Rabi frequency $\Omega_R \simeq 0.7$ THz ($\Omega_R/\omega_0 \simeq 0.2$ i.e. ultrastrong coupling). The present group-IV semiconductor material platform can be extended to the 5-12 THz range, where these semiconductors are transparent, as opposed to the III-V compound semiconductors plagued by strong THz optical phonon absorption. Moreover, the intersubband transition in

---

[*] Email: michele.ortolani@roma1.infn.it

parabolic quantum wells hosted by the non-polar $Si_{1-x}Ge_x$ crystal lattice is robust against carrier density and temperature variations, making the strength of the coupling only weakly temperature-dependent from 10 to 300 K. These results pave the way for the employment of the $Si_{1-x}Ge_x$ material platform to perform fundamental research in ultrastrong light-matter coupling, fully exploiting the plasmonic character of the cavity mirror, as well as in ultrafast modulators and saturable absorbers for THz laser research.

Introduction

The strong coupling regime of the light-matter interaction has been recently reported in many different physical systems [1] and electromagnetic frequency ranges from the microwaves [2, 3], to the terahertz [4, 5, 6, 7], the infrared [8, 9] and the visible [10, 11]. Strong coupling appears when a quantum system, showing a spectrally isolated "matter" resonance, modeled with a two-level system with transition energy $\hbar\omega_0$, is embedded into an electromagnetic cavity featuring its own "light" resonance at frequency ω_c. Experimentally, the strong coupling regime is detected through the spectroscopic observation of polariton band dispersion as a function of detuning $(\omega_0 - \omega_c)$ controlled by the cavity length [9, 6, 7, 12], by an external field [13, 14, 15, 4], or by temperature T [16]. Anti-crossing behavior of light and "matter" resonances is then observed, and the light-matter coupling strength can be quantitatively assessed by measuring the frequency difference between the upper and lower polariton bands at zero detuning, corresponding to twice the Rabi frequency Ω_R of the ideal two-level system [17]. Perspective applications of this phenomenon rely on the mixed light-matter nature of polaritons, which would eventually allow the control of quantum light through degrees of freedom that are typically employed to control quantum matter, such as electron or spin currents, and electric or magnetic fields. In this respect, lithographic semiconductor microcavities that feature high reproducibility, scalability of the production, and possible room-T operation [7, 6, 18, 19, 20] may be favored over more exotic materials and configurations. The use of foundry-compatible epitaxial semiconductor layers is also a clearly desirable feature for applications. This is even more desirable if the material is silicon-based and/or compatible with silicon foundry technology. Especially a material compatibility with the CMOS processes and post-processing, such as in Ge and for SiGe alloys is of great advantage [21].

Indeed, semiconductor quantum wells (QWs) supported by epitaxial semiconductor heterostructures have been consistently used in the realization of strong-coupling system due to the possibility of designing two-level-like resonances with ω_0 in the mid-IR and THz ranges and strong transition dipole moment μ_{12} set by the highly confined 2D (two-dimensional) electron density n_{2D}, to be employed as the "matter" oscillator. The cyclotron resonance of a 2D electron gas (2DEG) confined in a QW can be strongly coupled to a 2D metasurface of metallic split-ring resonators acting as cavities [14, 4]. In general, 2DEG resonances benefit from collective coupling enhancement because the 2DEG acts as a single quantum system [22], therefore the normalized coupling-strength ratio Ω_R/ω_0 scales with $\sqrt{n_{2D}}$, as outlined in the seminal paper from Dicke [23]. Furthermore, n_{2D} can be increased by remote (modulation) doping without increasing the QW volume or the energy loss. Another type of QW resonances, not requiring a magnetic field, however with lower quality factor than cyclotron resonances, are intersubband transitions (ISBTs) between quantum-confined states in the well (sub-bands). After the initial demonstration in a dielectric cavity [24], the use of sub-wavelength metal-bound microcavities and the progressive scaling of ω_0 towards THz frequencies led to intriguing demonstrations of ultrastrong light-matter coupling, where $\Omega_R/\omega_0 > 0.1$ [17, 19]. The collective nature of ISBTs, effectively constituting a plasmon [22], has been theoretically described using the dipolar gauge [25], showing interesting interplay between the strong coupling and the depolarization shift that poses as well some limitations to the normalized coupling strength [26, 7].

Theoretically, the light-matter coupling constant Ω_R is given by the matter transition rate due to the excitation by cavity vacuum field fluctuations. If one assumes a homogeneous average vacuum field strength E_{vac} in a cavity filled with a lossless medium with dielectric constant ε, one can write [1, 17, 27]:

$$\Omega_R = \frac{\mu_{12}E_{vac}}{\hbar} = \frac{\mu_{12}}{\hbar}\sqrt{\frac{\hbar\omega_0}{2\varepsilon_0\varepsilon V_m}} = \sqrt{\frac{f_{12}e^2}{\varepsilon_0\varepsilon m^*}\frac{N_{QW}}{L}n_{2D}} \tag{1}$$

where we have first written E_{vac} in terms of the ratio of the transition energy $\hbar\omega_0$ over the cavity modal volume ϵV_m, and then we have further specified μ_{12} in the relevant case of a 2DEG at zero temperature embedded in a planar cavity of length L using the oscillator strength f_{12}, the electron effective mass m^*, and the fundamental charge e. The integer number $N_{QW} \geq 1$ comprises the stacking of many identical epitaxial layers with identical 2DEGs in the same cavity with homogeneous field, assuming total filling of the cavity with QWs. It turns out that ISBTs with high μ_{12} due to high n_{2D}, embedded in microcavities with nanometric L (and therefore V_m) hence very high E_{vac}, provide light-matter coupling values Ω_R/ω_0 among the largest of all physical systems [1]. In previous work on the strong coupling of ISBTs to cavities, the focus was mostly on the cavity design, trying to minimize V_m [18, 28, 29], or to obtain a cavity field perfectly parallel to the dipole moment of ISBTs (orthogonal to the epitaxial plane), which has been achieved in patch antennas with a metallic ground plane [6, 30, 31], in double-metal gratings [9] and in fully etched metal-insulator-metal (MIM) cavities [32]. A two-level "matter" oscillator spectrum is provided by QWs with parabolic confinement potential (PQWs) that mirrors a quantum harmonic oscillator, in which empty-band excited states are equidistant in energy [33, 34]. Therein, the Kohn's theorem guarantees that the Hartree interaction term is exactly canceled out by the many-body corrections, therefore the ISBT energy does not depend any more on the electron population. Strong coupling at THz frequencies has been observed in III-V compound-semiconductor PQWs grown by many small steps of digital alloying [7], and, more recently, in extremely high-quality III-V PQWs[34] obtained by continuous variation of the alloy composition[19] .

In this work we further develop $Si_{1-x}Ge_x$ PQWs with continuously graded alloy profile [35, 36] and we embed them into suitable microcavities (fully-etched patch-antennas, or MIM resonators) to observe the strong coupling at THz frequencies in a group-IV, silicon foundry-compatible, material. One of the mirrors of MIM resonators is realized with a heavily doped semiconductor layer instead of a metallic layer to allow future fabrication in silicon foundries. Ultrastrong coupling with $\Omega_R/\omega_0 \simeq 0.2$ is achieved. The ultrastrong coupling condition is observed up to room-T, with quality factor of the polariton spectral lines almost independent on T, which is attributed to the weaker electron-phonon interaction featured by the non-polar lattice of group IV semiconductors, if compared to the polar III-V compound semiconductors. The coupling strength also has a very weak dependence on T, which is entirely attributed to the variation with T of the SiGe dielectric constant and of the electron density transferred in the wells from remote dopants, and not to intrinsic properties of the light-matter interaction. The present understanding of the strong-coupling conditions in $Si_{1-x}Ge_x$ quantum wells may be exploited in the future to obtain photonic quantum state manipulation at room-T together with microelectronics integration in silicon-based devices.

Results and discussion

In an ideal PQW, mimicking a collective quantum harmonic oscillator, the spectral weight of ISBTs is concentrated in a single absorption peak, irrespective of the Fermi energy (doping level) and the temperature [34]. The frequency position of this peak can be estimated from the bare energy distance between any two subsequent levels in the undoped parabolic well

$$\Delta E = \hbar\sqrt{\frac{8\Delta_0}{W^2 m_z^*}} \tag{2}$$

where Δ_0 is the energy difference between the minimum of the undoped PQW and its edge, where the constant-composition barrier for electrons starts on both sides of the well (barrier height, set by the maximum band offset of the heterostructure), W is the total well width of the order of tens of nanometers, and $m^*{}_z$ is the electron-confinement effective mass in the growth direction z. In Figure 1 we show the schematics of the complete heterostructure, which consists of a superlattice of 25 PQWs realized on a GeSi/Ge virtual substrate (VS) grown on silicon substrate wafers. The PQW heterostructure has been grown epitaxially by ultra-high vacuum chemical vapor deposition (UHV-CVD) using GeH_4 and SiH_4 gas precursors, without carrier gas [35]. The first layer of the VS consists of a relatively thick (3 µm) Ge buffer layer grown directly on the Si(001) wafer substrate by means of an out-of-equilibrium growth technique [37], which allows to completely relax the heteroepitaxial strain existing with the underlying Si substrate, while minimizing the density of extended defects generated during the plastic relaxation process, such as the threading dislocations [38]. A 2000-nm thick, reverse-graded concentration $\mathrm{Si}_{1-x}\mathrm{Ge}_x$ layer is then grown to achieve a lattice parameter a corresponding to that of a relaxed $\mathrm{Si}_{0.10}\mathrm{Ge}_{0.90}$ alloy. This particular composition is chosen to realize the strain compensation conditions for the PQW active layer. The PQWs are grown by continuously varying the gas precursor concentration in the CVD reactor to obtain a composition profile of ideal parabolic wells of thickness $W = 61$ nm, reaching a Ge content $x = 1$ at the center of the wells and $x = 0.82$ at the inter-well barriers of thickness $b = 16$ nm. Modulation doping with electrons of the PQWs is achieved by remote-impurity doping via PH_3 codeposition in the central region of the barriers. Modulation doping is possible because the ionized phosphorus impurity states are of higher energy than the ground state of the PQW, and thus electrons are transferred in the donor-free well region. A scanning transmission electron microscopy (STEM) image of a typical sample is shown in Figure 1(a), where one can see the high quality of the structure and the absence of extended defects. In Figure 1(b) we display a highly resolved STEM detail of the structure with the composition profile overlaid, as obtained by the calibration of the STEM intensity profile with the secondary ion mass spectroscopy (SIMS) data. The high reproducibility of the PQW epitaxial deposition process is clearly evident in Figure 1(c), where the individual SIMS-calibrated STEM intensity profiles of 10 PQWs of the stack are superimposed and plotted together with the nominal parabolic composition profile. The high accuracy obtained in the profile of each PQW can be quantified by the relative composition profile error displayed at the bottom of panel c, showing that the grown composition profile agrees with the nominal one within 1%, for all the measured PQWs. The high reproducibility of the 25-PQW superlattice (SL) is also confirmed by x-ray diffraction (XRD) data in Figure 1(d), showing sharp SL peaks and a very good agreement between the simulation of the 004 Bragg reflection XRD scan (black curve) and the experimental data (green curve). The XRD measurement also confirms the lattice matching of the VS and the PQWs. This thorough characterization of the heterostructure enabled us to properly calculate the electronic states of the PQWs. In Figure 1(e) we report the bare energy profile determined by means of a multi-valley self-consistent code in the parabolic $\mathbf{k} \cdot \mathbf{p}$ envelope function approximation[39] using the parabolic Ge composition x profile measured by SIMS/STEM as input. The resulting real potential shape (black curve in panel (e)) is very close to an ideal parabola with $\Delta_0 = 112$ meV and $W = 61$ nm. Consequently, using $m_z^* = 0.13\ m_e$ for the Ge conduction band minimum at the L-point, the associated confined electron states exhibit equally spaced energy separation $\Delta E = 12$ meV. In Figure 1(f) we report the effective energy band profile at 10 K accounting for the Hartree potential in the case of the doped well, at the doping level used in this work. Note that, although the energy level spacing decreases if compared to the undoped case, the ISBT energy $\hbar\omega_0$ is still expected at the undoped value ΔE according to the Kohn's theorem [17].

The matter resonance frequency ω_0 was then measured by performing ISBT spectroscopy with a Fourier-transform infrared spectrometer (FTIR) adapted to work in the THz range (1-

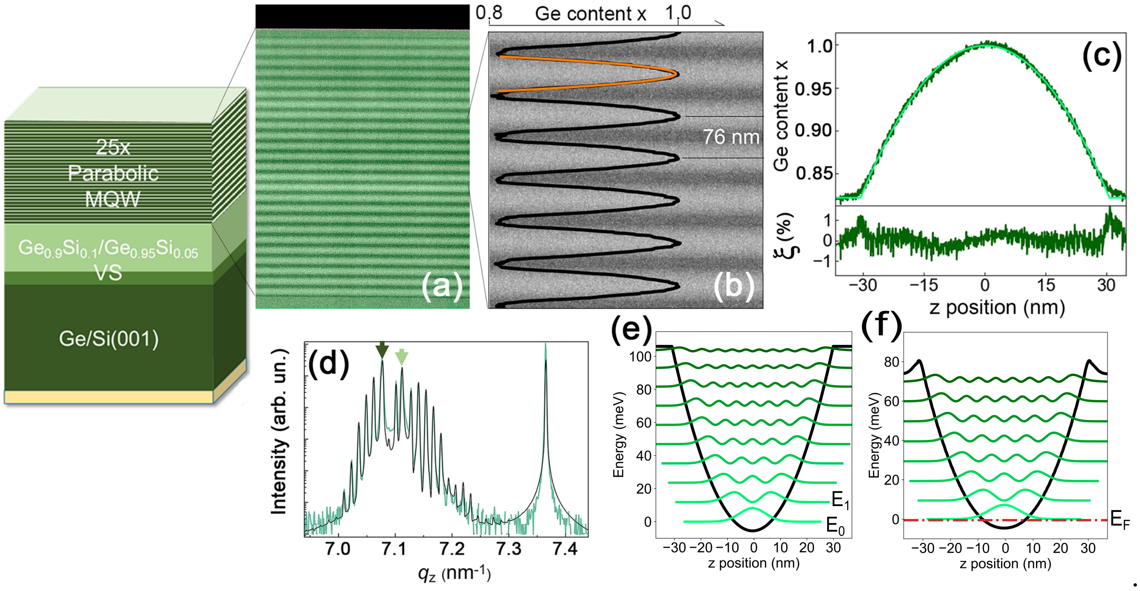

Figure 1: *Schematics of the grown heterostructure together with (a) False color dark-field STEM image of the entire PQW stack. Lighter green corresponds to higher Ge content. (b) STEM details of the PQWs stack overlaid by the composition profile obtained by SIMS-calibrated STEM. (c) Top: Superposition of ten different PQW STEM profiles (dark green) and of the nominal parabolic concentration profile (light green). Bottom: relative composition error for all the ten PQW composition profiles. (d) XRD curve across the 004 Bragg reflection of the heterostructure. With dark/light green arrows we identify the diffraction signals from the thick Ge buffer layer and* $Si_{0.1}Ge_{0.9}$ *VS, respectively. (e) Calculated confinement energy profile at the L point of the conduction band for an undoped PQW having the compositional parabolic profile shown in (c) (black) together with the square modulus of the wavefunctions, that are plotted at the energy level of the corresponding quantized state, using* $m_z^* = 0.13\ m_e$ *for electrons at the L-point of the conduction band of Ge. (f) Same as (e) for the doped PQW used in this work. The dash-dotted line represents the Fermi level for the nominal doping density. The calculations have been preformed at 10 K*

30 THz) (see setup sketch 2(b)), in vacuum and at temperatures T from 10 K to 300 K, in linear-dichroism mode, and in transmission configuration with small focal spot of the order of the wafer thickness (0.5 mm). Samples with doped PQWs were metal-coated and cut into side-coupled prism waveguides to probe the ISBT absorption in the volume occupied by the PQWs, as sketched in Figure 2(c). ISBT spectra are calculated after baseline subtraction of linear-dichroic ratios at several T and reported in Figure 2(a). A single strong transmission dip at all T is the signature of a harmonic-oscillator absorption spectrum, better described as a collective "bosonic matter" excitation [17]. From a global fitting of the data in Figure 2(a) with an exponentially modified Gaussian function (see Supporting Information for the fitting curves), we measured the center absorption frequency $\omega_0 = 3.1 \pm 0.2$ THz at all T. A numerical estimate of n_{2D} in the PQWs was obtained by solving the multi-valley self-consistent Schrödinger-Poisson equations for the actual charge transfer of electrons from remote (modulation) dopant impurities in the barriers to the wells. This calculation also allows to predict the Fermi level position for the used doping density at 10 K, reported in Figure 1(f). Due to the high density of states at the bottom of the conduction band of Ge, the Fermi level does

not considerably shift above the ground state with increasing doping, even in the present case of moderately high doping, at odds with most III-V compound semiconductor PQWs. We estimate $n_{2D} \sim 3 \times 10^{11}$ cm^{-2}, in reasonable agreement with the corresponding values estimated by the ISBT absorption spectral weight measured from Figure 2(a) [39] that however has high uncertainty levels at all Ts. The lowest linewidth is observed at 100 K, from which we estimate an energy loss parameter of the "matter" resonance $\Gamma_{\text{ISBT}} = 1.0$ THz, rising to 1.7 THz at room-T mostly due to the electron-phonon interaction. At $T < 100$ K, Γ_{ISBT} increases again, as already observed in modulation-doped rectangular Ge/$Si_{1-x}Ge_x$ QWs [40], where this effect has been attributed to the interplay between the ionized impurity density and the electron kinetic energy both varying with T as also observed in III-V compound semiconductor PQWs[41].

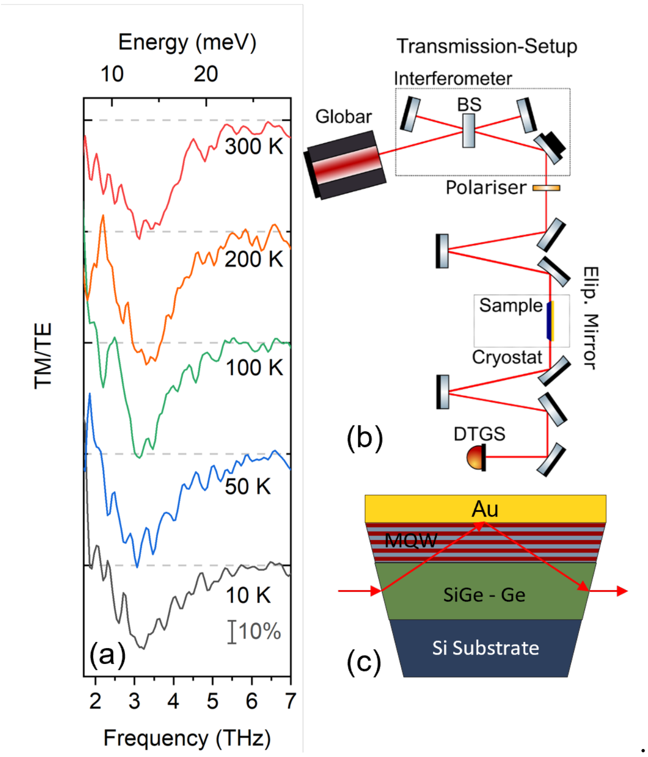

Figure 2: *FTIR spectroscopy characterization of the specific PQW structure used in this work. (a) Linear-dichroic transmission spectra at various temperatures, from T = 10 K to room-temperature. (b) Sketch of the optical beam path and (c) sketch of the sample in the prism waveguide geometry.*

For the cavity design we have chosen a square patch antenna with conducting ground plane and etched sidewalls, to improve the field confinement inside the cavity. Patch antennas have been employed successfully in mid-IR and THz strong coupling experiments with ISBTs in QWs [6, 32, 30, 31]. The optimal cavity length L for increasing the vacuum field and therefore the light-matter interaction strength, given by the distance between the conducting ground plane and the top metal patch directly evaporated on the last layer of the heterostructure, has been determined in Ref. [42] from electromagnetic (EM) simulations to be between 1.5 and 2.0 µm. Therefore, a value of $L = 1.8$ µm was chosen after performing similar EM simulations with 3D finite-element commercial software (CST microwave studio, see Methods for details) for our group-IV material system using $\varepsilon_\infty = 15.5$ for $Si_{0.10}Ge_{0.90}$ corresponding to the average Ge concentration in the active region. In the simulations of Figure 3(c-e), the square patch side s has been varied from 7 µm to 14 µm to span the cavity resonance frequency range $\omega_c = 2.0$ to 4.5 THz encompassing the $\omega_0 = 3.1$ THz determined from Figure 2: the predicted crossing is found at $s = 13$ µm for a MIM cavity (yellow curve in Figure 3(c)). A large-area periodic array is typically required for far-field optical experiments on microcavities: here, the period P of the square array of patch antennas was set to $P = 3s$ to avoid dipole coupling among neighboring patches. For example, Todorov et al.[25, 6] have studied the strong coupling in similar THz square microcavity arrays, however in the limit where the spacing between patches is smaller than s, $P < 2s$. Therein, both P and s influence the optical absorption resonance frequency, while in this work we seek a condition where the spectral position of ω_c is independent from P [28, 30, 31].

In order to make the fabrication process potentially compatible with CMOS foundries, and to eventually exploit plasmonic effects at shorter wavelengths in the future, we adopt a cavity configuration where the lower metallic mirror is replaced by an highly doped semiconductor ground plane. The ground plane was realised by heavily doping the reverse-graded $Si_{1-x}Ge_x$ virtual substrate (light green layer in Figure 1) and characterized experimentally in a separate area of one of the samples, where the PQW heterostructure was fully etched away. The dielectric function of the n^+-SiGe alloy (average composition $Si_{0.05}Ge_{0.95}$) acting as ground plane was determined by measuring its absolute reflectance in the 1-100 THz range by FTIR spectroscopy for T = 10 K and T = 300 K with a gold mirror reference (Figure 3(a)), and then applying Kramers-Kroning transformations [43]. The results are shown in Figure 3(b): the screened plasma frequency is found at 16 THz at both temperatures, which is not as high as record values for pure Ge of Refs. [43, 44] but is high enough for ground-plane operation in the range up to 12 THz (see Figure 3). One may notice the relevant value $\varepsilon' = -175$ at 3 THz at 10 K. The 3D free electron density $n = 6.5 \times 10^{18}$ cm^{-3} , estimated with the Drude model of the reflectance ($m^* = 0.13 m_e$), is well beyond the Mott transition to a degenerate semiconductor, ensuring that the ground plane will have conducting behavior at low T [43]. The calculated skin depth is around 1 µm, half the value of the doped layer thickness of 2 µm.

The measured n^+-$Si_{1-x}Ge_x$ dielectric function at 300 K was then used to simulate the hybrid metal-insulator-doped semiconductor cavities. From the simulation, the optical overlap compared to identical MIM cavities changed by less than 5% over the considered frequency range. The spectral results for the cavity with undoped PQW filling are shown in Figure 3(d). The quality factors (Figure 3(g)) are now dominated by losses in the ground plane but they are still better than the ISBT quality factor, so it is not expected that this will be the dominant loss factor in the final device with doped PQWs. The linear dependence (Figure 3(f)) of ω_c vs. s^{-1} found in MIM cavities of Figure 3(c) is confirmed, with a global redshift of $\sim$ 1.5 THz, indicating that a larger area of the ground plane is involved in the EM current patterns compared to the gold ground plane [28]. The predicted crossing is now found at $s = 10\,\mu\mathrm{m}$ for the hybrid cavity. The absolute value of the absorption decreases for longer s and lower ω_c due to increasing mismatch between the wavelength and L [45]. Finally, the strong-coupling conditions were simulated by introducing an anisotropic dielectric function for the doped PQW layer (Figure 3(h)) [46]. The dielectric function parameters are calculated from the ISBT spectra in Figure 2 and we added an optical overlap factor $f_{\mathrm{QW}} = 0.29$ that measures the cavity volume effectively occupied by the 2D-confined electrons at T = 10 K as further explained below [19]. A clear splitting of the polariton dispersion as a function of s is observed in Figure 3(e), with the lower polariton much less intense than the upper polariton, due to the above-mentioned mismatch between the wavelength and L[45]. Nevertheless, transfer of spectral weight from the upper to the lower polariton is observed, as expected, when approaching the predicted crossing. The numerical estimate of the Rabi frequency, determined from half the splitting at $10\,\mu\mathrm{m}$, is $\Omega_R = 0.55$ THz, which is comparable to both the "light" and the "matter" loss parameters around 1 THz estimated from Figure 3(d) and Figure 2(a), respectively. Knowing what to expect, we can now proceed with the experimental demonstration.

The cavity array fabrication was performed by electron-beam lithography and reactive-ion etching (see Methods for details). Two nominally identical samples featuring both the plasmonic ground plane and the doped PQW stack were used, as well as a a third identical sample with undoped PQW stack. The PQW epitaxial stack was kept identical to that of the samples analyzed in Figures 1 and 2, with the only difference of the heavy doping of the n^{+}-$\mathrm{Si}_{1-x}\mathrm{Ge}_x$ virtual substrate. Cavities with different s spanning the $7-14\,\mu\mathrm{m}$ range around the predicted crossing at $s = 10\,\mu\mathrm{m}$ were simultaneously fabricated on the same chip in the same nanofabrication process, ensuring that the cavity walls, the etching depth and the heterostructure parameters were exactly the same for all values of s. For the first sample a pitch of $P = 2s$ was used while for the second and third (undoped) sample a pitch of $P = 3s$ was used to experimentally check for possible effects of interacting cavities. Two electron microscopy images of the first sample after cavity fabrication are shown in Figure 4(c,d), also showing the experimental definition of s and P. Each array was $2 \times 2\ \mathrm{mm}^2$ in size, spaced by 1 mm. A $2 \times 2\ \mathrm{mm}^2$ area without cavities was etched down to the ground plane and used as the reflectance reference for the polariton spectroscopy experiment in the 1-6 THz range. These "empty arrays" were also used for the measurements in Figure 3(a,b).

Cavity reflectance spectra $R(\omega)$ can be considered as the opposite of absorption spectra $A(\omega) = 1 - R(\omega)$ due to the presence of the ground plane that prevents any transmittance [6, 19]. For the reflectance measurements we developed a custom-made optical insert based on tightly-focusing ellipsoidal mirrors (sketched in Figure 5(c)) that could de-magnify the FTIR spot size by 3× inside the vacuum chamber of the spectrometer. With this insert, all cavity arrays with different s could be investigated in the same cryogenic cycle, thereby ensuring

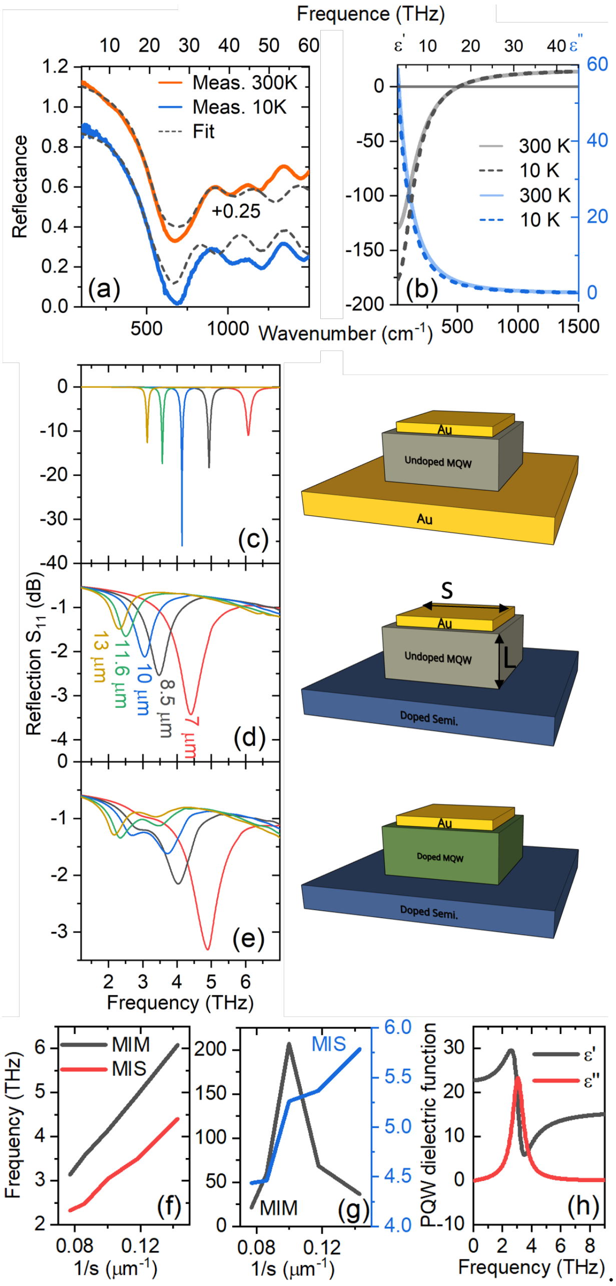

Figure 3: *(a) Normal-incidence reflectance with Drude fit and (b) the corresponding dielectric function of the heavily doped Si$_{0.1}$Ge$_{0.9}$ ground plane. (c-e) Simulated reflection spectra (S_{11} parameter) of microcavities with different gold patch side s as indicated in panel (d) for different color curves. Panel (c): ideal case of a gold ground plane; Panels (d,e): heavily doped Si$_{0.1}$Ge$_{0.9}$ ground plane with active layer made of (d) undoped and (e) doped PQWs with filling fraction $f_{QW} = 0.29$. Two polariton branches are apparent in panel (e) with avoided crossing of the intrinsic PQW resonance set at $\omega_0 = 3.1$ THz in the simulations. Note the global resonance redshift and broadening between (c) and (d), and the smaller blueshift of the upper polariton in (e) if compared to the bare cavity resonance in (d), entirely due to the ultrastrong light-matter coupling. (f) Geometry dependence of the resonance position for the MIM (c) and MIS (d) cavities. (g) Q-Factor of the MIM and MIS resonances over the inverse cavity lemgth. (h) used dialectic function for the PWQ simulation*

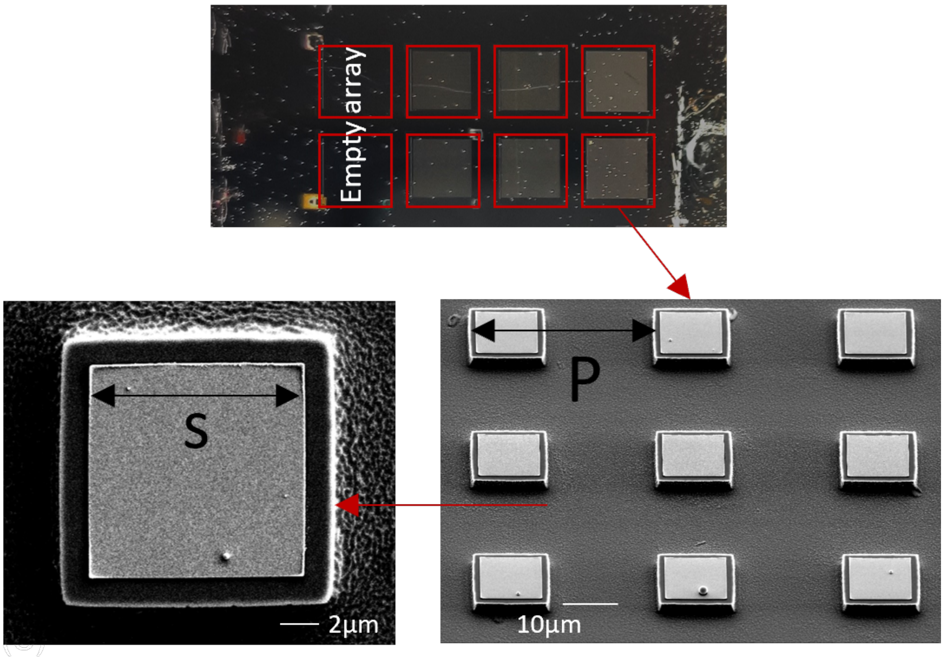

Figure 4: *Top: optical image of the* 1×2 *cm epitaxial chip: six* 2×2 *mm*^{2} *fields are visible, each of them with cavities of different s. Right: A portion of an array of patch cavities with a unit cell dimension* $P = 3s$*; note the semiconductor ground plane contrasted to the gold square patch. Left: detail of an individual patch cavity with* $s = 11\,\mu m$*, where s is the width of the metallic patch.*

identical conditions for all spectra in Figure 5(a,b). The reflection spectra of the cavity arrays filled with undoped PQW stack are reported in Figure 5(a,b) for T = 10 K (grey curves, identical in the two panels) and are consistent with the simulations in Figure 3(d). Turning to the polariton dispersion at $T = 10$ K (red curves for $P \sim 2s$ in Figure 5(a) and black curves for $P \sim 3s$ in Figure 5(b)), already at $s = 7\,\mu m$ with large detuning $\omega_c - \omega_0 \simeq 1.4$ THz, one sees a clear offset in the absorption resonance frequency of the doped-PQW samples, which is due to the upper polariton dispersion being pushed away from the bare cavity value by ultrastrong coupling. Even at $s = 7\,\mu m$ the linewidth of the upper polariton is above 1 THz, broader than that of the bare cavity resonance (Γ_c = 0.9 THz at $\omega_c = 4.5$ THz leading to a typical bare patch antenna Q-factor of 5, decreasing to $\sim$ 4 for doped PQWs). This indicates that electrons in the PQWs contribute to cavity losses. When the cavity resonance is tuned closer to ω_0 ($s > 10\,\mu m$), a splitting in the polariton dispersion is observed, with both upper and lower polariton clearly visible from $s = 11\,\mu m$ to $14\,\mu m$. Here, the linewidths of both polaritons are much broader than those of the bare cavity resonances (Q-factors below 3), approaching the limit value $\Gamma_{\mathrm{ISBT}}(10\,\mathrm{K}) = 1.4$ THz (Q-factor $\sim$ 2), indicating the strongly mixed "light-matter" nature of the cavity resonance. Bi-Lorentzian fitting of each reflectance spectrum were then performed to obtain the two experimental polariton frequencies ω_{UP} and ω_{LP} (fitting curves reported in the Supporting Information). In Figure 5(d,e) we report experimental (symbols) and simulated (segmented curves) polariton frequencies together with the bare cavity (undoped PQW) resonances. These two plots are not significantly different from each other, indicating that the absorption cross-section of single antennas is definitely smaller than $3s \times 3s$ and probably even smaller than $2s \times 2s$ [47], therefore we can confirm that we are spectroscopically studying the single-cavity properties. The minimum polariton splitting at the avoided-crossing point was used to estimate Ω_R. We calculated the average of the minimum splittings in the two samples at $s = 10\,\mu\mathrm{m}$ (expected crossing point from simulations) and it gives $\Omega_R = 0.68 \pm 0.05$ THz. Finally we compared our experimental and simulated polariton dispersions with a theoretical model for the ultrastrong light-matter coupling (dipolar-coupling Hamiltonian[17]). The continuous grey curves in Figure 5(d,e) are calculated by solving the secular equation from Ref.[48, 7, 19]

$$(\omega^2 - {\omega_0}^2)(\omega^2 - \omega_c^2) = f_{\mathrm{QW}}\omega_p^2\omega_c^2 \tag{3}$$

where $\omega_0 = 3.1$ THz is the measured ISBT from Figure 2(a), f_{QW} is the optical overlap factor (i.e. the cavity volume fraction occupied by the QWs as detailed below), $\omega_c = \frac{Ac}{s}$ is the simulated undoped-PQW cavity resonance from Figure 3(d) ($A \sim 0.1$ is a phenomenological proportionality constant and c is the light velocity in vacuum), and $\omega_p = \sqrt{\frac{f_{12}e^2 n_{2D}}{\varepsilon_0 \varepsilon m^* L_{QW}}}$ is the plasma frequency of the 2D-confined electron gas [48, 19]. The best agreement between the experimental data points and the model is obtained for a plasma frequency $\omega_p = 2.6$ THz. For ideal PQWs, f_{12} can be taken close to 1 at all T (we use $f_{12} = 0.97$ to account for the few transitions with non-confined final states). Considering the sub-band state population at $T = 10$ K, only the ground state is significantly occupied, therefore we can write $L_{\mathrm{QW}} = 21$ nm from the spatial extent of the ground-state wavefunction in Figure 1(e) and $f_{\mathrm{QW}} = L_{\mathrm{QW}}/(W + b) = 0.29$. We can now provide a global estimate from the theoretical model fitting to all data $\Omega_R = \omega_p\sqrt{f_{\mathrm{QW}}}/2 = 0.75$ THz, which quantifies the light-matter coupling strength in our system at 10 K. From the expression $\Omega_R = \sqrt{\frac{f_{12}e^2 n_{2D}}{\varepsilon_0 \varepsilon m^*(W+b)}}$, we can calculate $n_{2D} = 3.2 \times 10^{11}$ cm^{-2}, which is in good agreement with the independently measured spectral weight estimate in Figure 2 and with the Schrödinger-Poisson calculation of electron transfer from remote donors. The normalized coupling-strength ratio measured at the anti-crossing point from the theoretical polaritonic branches is $\frac{\Omega_R}{\omega_0} \simeq 0.24$, testifying the achievement of the ultrastrong coupling regime. Note that, in PQWs, Ω_R will only depend on T through n_{2D} and ω_0 is fairly T-independent, therefore the coupling regime should be almost T-independent up to room-T, as we now show.

Finally, in Figure 6 the temperature dependence of the polariton absorption spectra for one specific cavity array ($s = 12\,\mu\mathrm{m}$, $P = 2s$) was explored. Reflection spectra in Figure 6(a) were taken while heating, without displacing the spot from the cavity array. A first observation (Figure 6(b)) is the presence of the upper polariton line almost unchanged between 300 and 10 K, with only a small redshift of ω_{UP} with decreasing T (blue triangles). As a matter of fact, we observe a blueshift of the undoped cavity resonance from 300 K to 10 K (orange

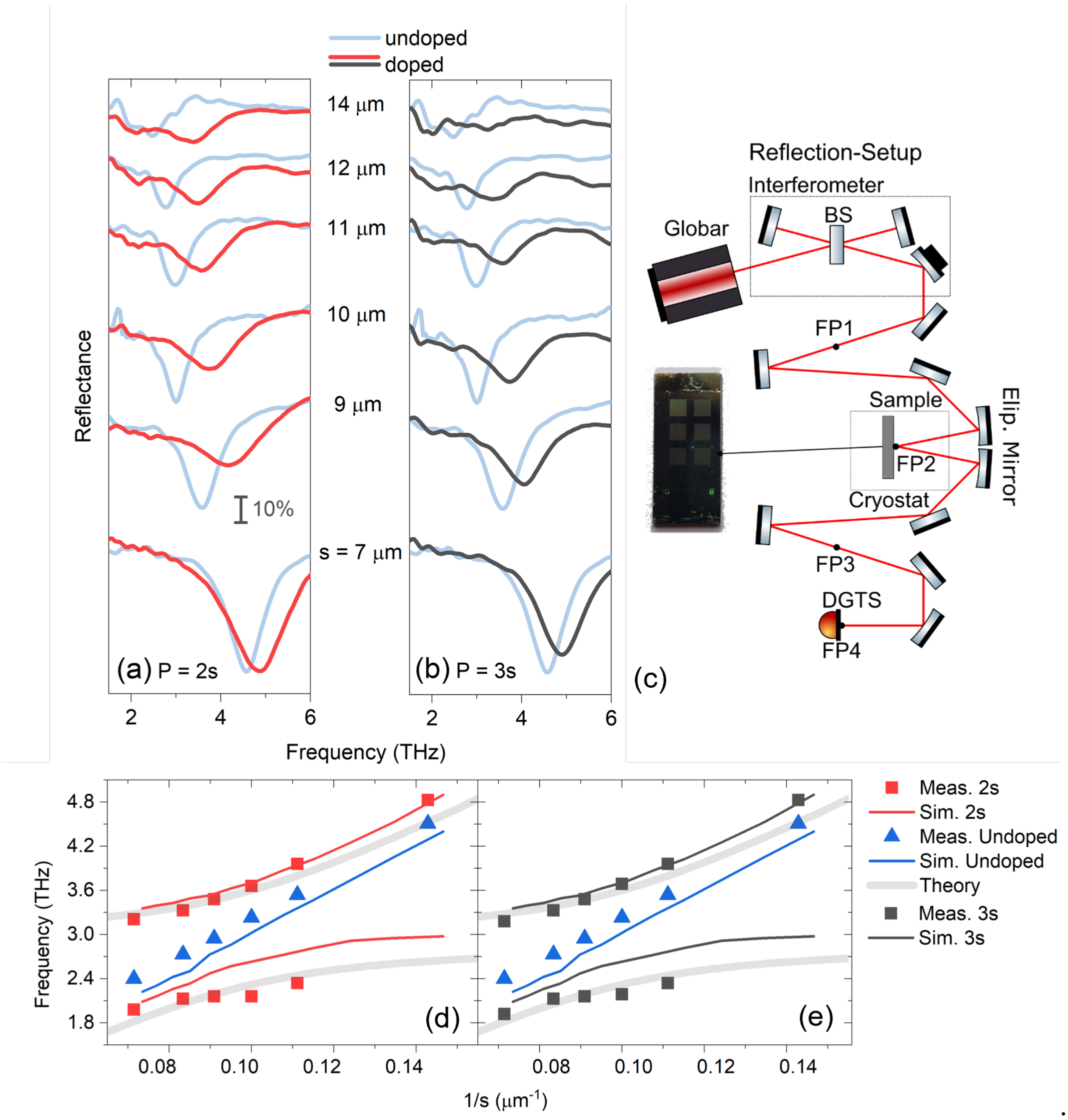

Figure 5: *(a) reflection spectra of the cavity arrays with* $P = 2s$ *(red curves), the grey curves are the reflection spectra of identical cavities fabricated on a sample with undoped PWQs. (b) Reflection spectra of cavities filled with identical doped PQWs but* $P = 3s$*. (c) sketch of the custom de-magnifying reflection setup and picture of the fabricated sample chip with all cavity arrays* (2×2 *mm*^{2})*. (d, e) polariton dispersion as determined by a bi-Lorentzian fitting of the data in panels a, b respectively. The error bar for the polariton frequencies in a single fitting routine is smaller than the symbol size.*

triangles in Figure 6(b) and dotted curves in Figure 6(a)), explained by the decrease of the dielectric constant of Ge from ~ 16 to ~ 15 triggered by the widening of the Ge bandgap. We attribute the observed deviation of ω_{UP} from the expected blueshift (dashed red line) to a decrease of n_{2D} with decreasing $T < 100$ K, now sensitively measured through Eq. 1 from the measured coupling strength $2\Omega_R(T) = \omega_{\mathrm{UP}}(T) - \omega_{\mathrm{LP}}$ (where we have assumed $\omega_{\mathrm{LP}} = 2.1$ THz constant at all T). Starting from the estimate from Eq. 3 $n_{2D} = 3.2 \times 10^{11}$ cm^{-2} at 10 K, we get $n_{2D} = 3.5 \times 10^{11}$ cm^{-2} at 100 K. A decrease of $n_{2D}(T)$ with decreasing T is theoretically explained by the T-dependence of the relative energy position of confined states in the barriers and in the PQWs, which limits the electron transfer from the dopant impurities to the PQWs at low T. The latter effect is due to the different thermal expansion coefficient of Ge and SiGe [49], which can be precisely simulated as detailed in the Methods. A second observation is the decrease of the upper polariton linewidth $\Gamma_{\mathrm{UP}}(T)$ from 300 K to 100 K, highlighted in Figure 6(c). This behavior mirrors the $\Gamma_{\mathrm{ISBT}}(T)$ seen in Figure 2, indicating that the polariton linewidth is determined by the same intrinsic material mechanisms that define the ISBT linewidth [50]. As a consequence of line broadening, the lower polariton line goes below the detection threshold of our experiment above 200 K. Even if the lower polariton disappears from the spectra of Figure 6(a) above 200 K, the strong-coupling condition is clearly maintained up to 300 K, as seen from the 1 THz-offset of ω_{UP} (continuous red spectrum in Figure 6(a)) from ω_c measured in the undoped PQW sample (dotted red spectrum). This is at odds with observations in III-V material PQWs, where both polaritons merge to ω_c around 200 K and then disappear at room-T [19]. We can conclude that, in suitably designed and grown $Si_{1-x}Ge_x$ PQWs, Ω_R can be made almost independent on T up to 300 K. We have further verified this occurrence by measuring all cavities with different s at room-T: the offset of ω_{UP} from the corresponding ω_c is clearly observed for all cavities at room-T, decreasing with increasing detuning (decreasing s) as expected, see Supporting Information.

To summarize, from the spectroscopy data in Figure 6(a) the coupling parameters plotted in Figure 6(c) were retrieved, from which an experimental demonstration of the ultrastrong-coupling condition can be obtained at all T: it can be deduced that the normalized coupling-strength ratio Ω_R/ω_0 stays around 0.2, almost T-independent from 10 K to room-T. Note that this experimental estimate agrees very well with theory fitting to raw polartion dispersion data at 10 K in Figure 5(d-e). Rabi oscillations are overdamped as $\Omega_R/\Gamma_{\mathrm{UP}} \sim 0.5$ at room-T and $\Omega_R/\Gamma_{\mathrm{UP}} \sim 0.7$ at 100 K: here we take Γ_{UP} as a reasonable estimate of polariton lifetimes, which seems to be closely related to Γ_{ISBT}. The polariton quality factor is consistently lager than unity, i.e. $\omega_{\mathrm{UP}}/\Gamma_{\mathrm{UP}} = 2.4$ at room-T and $\omega_{\mathrm{UP}}/\Gamma_{\mathrm{UP}} = 3.6$ at 100 K, which makes the present microcavities usable in THz photonics applications e.g. as amplitude modulators [51].

In conclusion, we have implemented the ultrastrong light-matter coupling between the intersubband transitions and a microcavity in electron-doped group-IV ($Si_{1-x}Ge_x$) parabolic quantum wells, which present small effective mass of electrons and regular Fermi surface geometry in the conduction band, comparable to the typical ones of n-type III-V semiconductors. This implementation provides: 1) Almost temperature-independent light-matter coupling up to room-temperature at $\omega_0 = 3.1$ THz; 2) High values of the 2D electron density hence of the coupling, as testified by $\Omega_R/\omega_0 \simeq 0.2$; 3) Compatibility with silicon photonics foundry technology, and potentially with the silicon CMOS process, because we crucially show that, in the THz range, the typical gold mirrors of microcavities can be substituted by doped-semiconductor ”plasmonic” mirrors. The present SiGe material platform will be relevant in future mainstream applications in quantum technology, where photon quantum states and integrated electronic circuits will have to interact on-chip. Due to both the CMOS compatibility

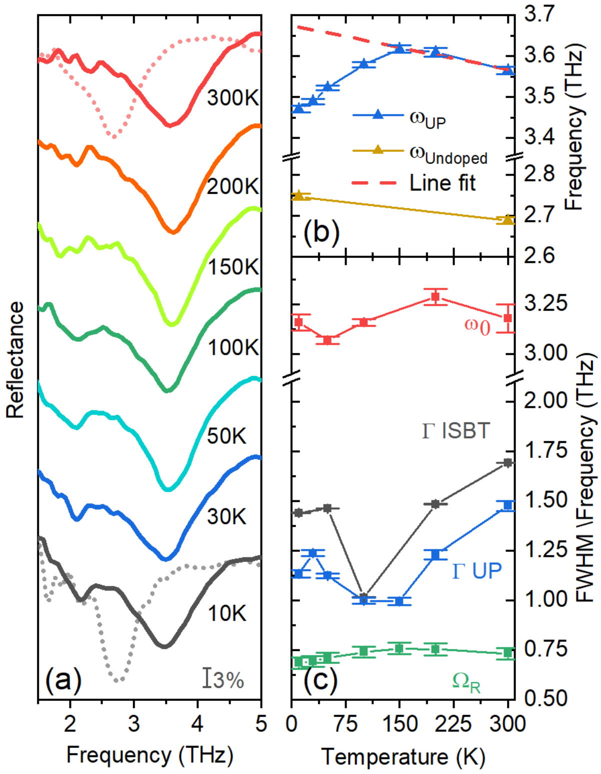

Figure 6: *(a): temperature dependence of the reflectance of ultrastrongly coupled cavities with* $s = 12\mu m$ *and* $P = 2s$ *(solid curves) and comparison with undoped cavities (dashed curves). (b): temperature dependence of the extracted upper polariton frequency compared to predictions based on the T-dependence of the dielectric constant of Ge and to the undoped sample (c): temperature dependence of: uncoupled intersubband resonance linewidth* Γ_{ISBT}*; upper polariton linewidth* Γ_{UP}*; intersubband resonance frequency* ω_0*; Rabi splitting* Ω_R*.*

of the PQW material and the rather large dimensions of the patch antennas in comparison to modern foundry processes, a further integration of the proposed system into an electrical controlled sensor or manipulator is viable. Using planarization steps all patch antennas could be electrically connected either at the 2DEG level, to read out the electron state by electrical transport measurements, and/or at the field-effect gate level, to populate or depopulate the PQW. This would not be possible with purely photonic or geometrical-plasmonic resonators [52]. In terms of progress in THz optoelectronics, the relevant outcome is that our approach can be easily extended up to 12 THz, while III-V compound semiconductors are inefficient above 5 THz due to optical phonon absorption in the reststrahlen band. In particularly, using rectangular quantum wells in similar cavities and tailoring the strong coupling condition, one should be able to develop ultrafast switches and saturable absorbers [53], to be employed in laser science in the almost unexplored 5-12 THz range.

Methods

Quantum calculations

The electronic band structure, electron wave-functions, and ISBT absorption spectra of the investigated samples have been calculated self-consistently, relying on a multi-valley effective mass Schrödinger-Poisson solver. A detailed description of the model can be found in Ref. [39]. For the T-dependence of n_{2D}, we have taken into account the presence, at energies comparable to the PQW sub-bands, of so-called Δ_2 states (situated along the $\Gamma-X$ line in k-space), confined in the barrier region. These levels limit the amount of charge transferred in the PQW sub-bands originating from the L-point band edge. Moreover, to tackle the T-dependence of the carrier density we have included in our model also the impact of the thermal strain induced by the difference in the thermal lattice expansion coefficient of Si and Ge. As a matter of fact, the thermal strain influences the energy separation between the Δ_2 and L sub-bands and provides n_{2D} monotonically decreasing with decreasing T.

Material growth

Samples were deposited by means of UHV CVD in a cold-wall reactor using ultrapure silane and germane without carrier gases. N-type doping was achieved by co-depositing phosphine. The active layer stack composed by 25 identical PQWs (thickness $W = 61$ nm) separated by $Si_{0.18}Ge_{0.82}$ barriers (thickness $b = 16$ nm) was grown on top of relaxed $Si_{1-x}Ge_x$ virtual substrate (VS) having low threading dislocation densities (TDD $= 3 \times 10^6$ cm^{-2})[54]. The VS growth on a Si(100) substrate leverages a reverse grading technique in which a Ge film is deposited directly on the Si substrate using a multi-temperature approach, followed by a compositional graded $Si_{1-x}Ge_x$ buffer layer [37]. The final Ge content in the buffer y matched the average Ge content of the active stack to ensure the strain compensation condition and avoid the plastic relaxation of the active region. In samples used to fabricate the microcavity arrays the last two micrometers of the VS were doped with a nominal P density $N_P = 1 \times 10^{19}$ cm^{-3}. The parabolic compositional profile $Si_{1-x}Ge_x$ with x in the range between $0.8 - 1$ of the wells was obtained by changing the SiH_4 gas flow and maintaining the GeH_4 one constant during the growth, using calibrated mass flow controllers. The deposition pressure varied consequently, and we estimated an average growth rate of 6 nm/min. The growth temperature for the active stack was set at 460°C. N-type modulation doping was achieved by co-depositing phosphine to a thickness of 5 nm in the center of the SiGe barriers. The nominal P density in the doped region of the barriers was 8×10^{17} cm^{-3}. The structural properties of the samples were evaluated by means STEM, XRD, and SIMS. STEM measurements have been performed using a FEI Titan microscope (FEI Company, Hillsboro, Oregon, USA) operating at 200 kV. It was equipped with aberration-corrected magnetic lenses to obtain electron probes with a diameter in the range of $1 - 2$ Å and beam currents of 200 pA. A CEOS CESCOR corrector was used to achieve a resolution of 0.8 Å . Images were recorded using a high-angle annular dark field (HAADF) detector (FEI Company, Hillsboro, Oregon, USA). Room-temperature XRD measurements were achieved by using a Rigaku SmartLab instrument with a rotating anode and line-focus geometry, featuring a Ge(400) × 2 channel-cut beam collimator. ToF-SIMS V from IONTOF was employed for the measurement of the compositional profiles. The depth profiles were acquired using $0.5 - 1$ keV a Cs^+ ion beam.

Infrared and Terahertz spectroscopy

Fourier-transform infrared (FTIR) spectroscopy was performed with a vacuum Bruker Vertex 70v spectrometer (Bruker, Ettlingen, Germany)) equipped with a helium-flow cryostat (Janis Research company, Woburn, Massachusetts (USA)), a wide-band silicon beamsplitter, a globar source and a pyroelectric detector with integrated preamplifier. For the ISBT measurements of Figure 2 performed in side-illuminated single-pass waveguide configuration, the lateral facets of our 2.5 mm long samples were cut at a 70° angle relative to the growth plane, and the top surface close to the QW stack was coated with a metal bilayer (Ti/Au 10 nm/80 nm), to align the electric field of the radiation propagating through the active region almost parallel to the ISBT dipole moment (i.e., TM polarized). The dichroic transmission spectra $T(\omega) = T_{TM}(\omega)/T_{TE}(\omega)$ were measured with a computer-controlled wire-grid polarizer, ensuring that polarization-independent spectral features unrelated to ISB transitions were suppressed. For the dielectric function determination of Figure 3, a quasi-normal incidence setup was employed, with incidence angle around 10° and a gold-coated surface as reference for determining the absolute reflectance $R(\omega)$. The latter quantity was processed via Kramers-Kronig tranformations, using a Hagen-Rubens extrapolation for $\omega \to 0$ and a Drude-Lorentz extrapolation beyond the non-transparency range above the plasma edge for $\omega \to \infty$. The resulting complex dielectric function $\tilde{\epsilon}$ is calculated from the complex reflectance $\tilde{r} = R(\omega) \cdot e^{i\phi(\omega)}$ via the standard Fresnel formulas. For the cavity measurements of Figures 5 ad 6 a high-numerical aperture reflectance setup was built using ellipsoidal mirrors with magnification factor × 3. The baseline-corrected reflectance of the cavity arrays was measured by using the bare doped-Ge ground plane as the reference. The cryostat cold finger was displaced vertically with a vacuum manipulator to change the spot position from a cavity array to another and to the reference during the same cryogenic cycle. 4096 scans at 10 kHz scanning speed and spectral resolution of 4 cm^{-1} were averaged for each cavity. Longer acquisition times did not lead to better signal-to-noise ratio below 30 cm^{-1} probably due to the $1/f$ noise of the DTGS detector.

Electromagnetic simulations

The finite element simulations have been carried out with CST microwave studio® employing the frequency domain solver. The highly doped mirror layer has been modeled with a user-defined dispersion employing the measured dielectric function data reported in Figure 3(b).

The intersubband resonance has been modeled with the dielectric function from Ref.[46] and the metal is lossy gold from CST library.

Device fabrication

In a first step the metal patches were produced via electron beam evaporation and a lift-off process using an electron beam lithography (EBL) (Raith VOYAGER) and PMMA (Poly methyl methacrylate) as resist. First 10 nm Ti were evaporated functioning as an adhesion layer directly followed by 80 nm of Au to form the top side mirror. The lift-off was performed without an ultra sonic bath to avoid damages to the mirrors. After a second EBL step the etching of the microcvavity was performed by an inductively coupled plasma - reactive ion etching (ICP-IRE) SF_6-Ar step.

Acknowledgement

The Authors would like to acknowledge detailed discussions with Raffaele Colombelli. G. Scalari acknowledges SNF project 200021–212735 for financial support. M. De Seta, M. Ortolani and S. Cibella acknowledge support from Italian MIUR grant PRIN 2022 “Strong light-matter coupling manipulation in SiGe quantum wells at terahertz frequencies” CUP F53D23001190006.

Supporting Information Available

Supporting Information for Publication contain: Fitting curves to the reflectance spectra in Figure 5; fitting curves to the TM/TE measurements in Figure 2; fitting curves to the temperature depended measurements Figure 6; Reflectance spectra at room-temperature for all values of s for both doped and undoped PQWs; detailed procedures for the determination of n_{2D} from experiment and theory.

References

[1] P. Forn-Díaz, L. Lamata, E. Rico, J. Kono, and E. Solano. “Ultrastrong coupling regimes of light-matter interaction”. In: *Rev. Mod. Phys.* 91 (2 June 2019), p. 025005. DOI: `10.1103/RevModPhys.91.025005`.

[2] X. Mi, J. V. Cady, D. M. Zajac, P. W. Deelman, and J. R. Petta. “Strong coupling of a single electron in silicon to a microwave photon”. In: *Science* 355.6321 (2017), pp. 156–158. DOI: `10.1126/science.aal2469`.

[3] Justin T. Hou and Luqiao Liu. “Strong Coupling between Microwave Photons and Nanomagnet Magnons”. In: *Phys. Rev. Lett.* 123 (10 Sept. 2019), p. 107702. DOI: `10.1103/PhysRevLett.123.107702`.

[4] Andreas Bayer, Marcel Pozimski, Simon Schambeck, Dieter Schuh, Rupert Huber, Dominique Bougeard, and Christoph Lange. "Terahertz Light–Matter Interaction beyond Unity Coupling Strength". In: *Nano Letters* 17.10 (2017). PMID: 28937772, pp. 6340–6344. DOI: `10.1021/acs.nanolett.7b03103`.

[5] Shima Rajabali, Sergej Markmann, Elsa Jöchl, Mattias Beck, Christian A. Lehner, Werner Wegscheider, Jérôme Faist, and Giacomo Scalari. "An ultrastrongly coupled single terahertz meta-atom". In: *Nature Communications* 13 (2022), p. 2528. DOI: `10.1038/s41467-022-29974-2`.

[6] Y. Todorov, A. M. Andrews, I. Sagnes, R. Colombelli, P. Klang, G. Strasser, and C. Sirtori. "Strong Light-Matter Coupling in Subwavelength Metal-Dielectric Microcavities at Terahertz Frequencies". In: *Phys. Rev. Lett.* 102 (18 May 2009), p. 186402. DOI: `10.1103/PhysRevLett.102.186402`.

[7] Markus Geiser, Fabrizio Castellano, Giacomo Scalari, Mattias Beck, Laurent Nevou, and Jérôme Faist. "Ultrastrong coupling regime and plasmon polaritons in parabolic semiconductor quantum wells". In: *Physical Review Letters* 108.10 (2012), p. 106402.

[8] Christian Huck, Jochen Vogt, Tomáš Neuman, Tadaaki Nagao, Rainer Hillenbrand, Javier Aizpurua, Annemarie Pucci, and Frank Neubrech. "Strong coupling between phonon-polaritons and plasmonic nanorods". In: *Opt. Express* 24.22 (Oct. 2016), pp. 25528–25539. DOI: `10.1364/OE.24.025528`.

[9] Erika Cortese, Ngoc-Linh Tran, Jean-Michel Manceau, Adel Bousseksou, Iacopo Carusotto, Giorgio Biasiol, Raffaele Colombelli, and Simone De Liberato. "Excitons bound by photon exchange". In: *Nature Physics* 17.1 (2021), pp. 31–35.

[10] Jeremy J. Baumberg, Javier Aizpurua, Maiken Mikkelsen, and David R. Smith. "Extreme nanophotonics from ultrathin metallic gaps". In: *Nature Materials* 7.18 (Lug 2019), pp. 668–678. DOI: `10.1364/OME.479637`.

[11] Rohit Chikkaraddy, Bart de Nijs, Felix Benz, Steven J. Barrow, Oren A. Scherman, Edina Rosta, Angela Demetriadou, Peter Fox, Ortwin Hess, and Jeremy J. Baumberg. "Single-molecule strong coupling at room temperature in plasmonic nanocavities". In: *Nature* 535 (2016), p. 127. DOI: `10.1038/nature17974`.

[12] Eric A Muller, Benjamin Pollard, Hans A Bechtel, Ronen Adato, Dordaneh Etezadi, Hatice Altug, and Markus B Raschke. "Nanoimaging and control of molecular vibrations through electromagnetically induced scattering reaching the strong coupling regime". In: *ACS photonics* 5.9 (2018), pp. 3594–3600.

[13] Aji A Anappara, Alessandro Tredicucci, Giorgio Biasiol, and Lucia Sorba. "Electrical control of polariton coupling in intersubband microcavities". In: *Applied Physics Letters* 87 (2005), p. 5.

[14] G. Scalari, C. Maissen, D. Turčinková, D. Hagenmüller, S. De Liberato, C. Ciuti, C. Reichl, D. Schuh, W. Wegscheider, M. Beck, and J. Faist. "Ultrastrong Coupling of the Cyclotron Transition of a 2D Electron Gas to a THz Metamaterial". In: *Science* 335.6074 (2012), pp. 1323–1326. DOI: `10.1126/science.1216022`.

[15] Qi Zhang, Minhan Lou, Xinwei Li, John L. Reno, Wei Pan, John D. Watson, Michael J. Manfra, and Junichiro Kono. "Collective non-perturbative coupling of 2D electrons with high-quality-factor terahertz cavity photons". In: *Nature Physics* 12.11 (NOV 2016), p. 1005. ISSN: 1745-2473. DOI: `{10.1038/NPHYS3850}`.

[16] Andrey Baydin, Manukumara Manjappa, Sobhan Subhra Mishra, Hongjing Xu, Fuyang Tay, Dasom Kim, Felix G. G. Hernandez, Paulo H. O. Rappl, Eduardo Abramof, Ranjan Singh, and Junichiro Kono. "Deep-Strong Coupling between Cavity Photons and Terahertz TO Phonons in PbTe". In: *CLEO 2023*. Optica Publishing Group, 2023, FF3D.2. DOI: `10.1364/CLEO_FS.2023.FF3D.2`.

[17] Cristiano Ciuti, Gérald Bastard, and Iacopo Carusotto. "Quantum vacuum properties of the intersubband cavity polariton field". In: *Phys. Rev. B* 72 (11 Sept. 2005), p. 115303. DOI: `10.1103/PhysRevB.72.115303`.

[18] Chih-Feng Wang, Terefe G. Habteyes, Ting Shan Luk, John F. Klem, Igal Brener, Hou-Tong Chen, and Oleg Mitrofanov. "Observation of Intersubband Polaritons in a Single Nanoantenna Using Nano-FTIR Spectroscopy". In: *Nano Letters* 19.7 (2019), pp. 4620–4626.

[19] Paul Goulain, Chris Deimert, Mathieu Jeannin, Stefano Pirotta, Wojciech Julian Pasek, Zbigniew Wasilewski, Raffaele Colombelli, and Jean-Michel Manceau. "THz Ultra-Strong Light–Matter Coupling up to 200 K with Continuously-Graded Parabolic Quantum Wells". In: *Advanced Optical Materials* 11.9 (2023), p. 2202724. DOI: `https://doi.org/10.1002/adom.202202724`.

[20] Aji A. Anappara, Simone De Liberato, Alessandro Tredicucci, Cristiano Ciuti, Giorgio Biasiol, Lucia Sorba, and Fabio Beltram. "Signatures of the ultrastrong light-matter coupling regime". In: *Phys. Rev. B* 79 (20 May 2009), p. 201303. DOI: `10.1103/PhysRevB.79.201303`.

[21] Valentin John, Francesco Borsoi, Zoltán György, Chien-An Wang, Gábor Széchenyi, Floor van Riggelen-Doelman, William I. L. Lawrie, Nico W. Hendrickx, Amir Sammak, Giordano Scappucci, András Pályi, and Menno Veldhorst. "Bichromatic Rabi Control of Semiconductor Qubits". In: *Phys. Rev. Lett.* 132 (6 Feb. 2024), p. 067001. DOI: `10.1103/PhysRevLett.132.067001`.

[22] B Askenazi, A Vasanelli, A Delteil, Y Todorov, L C Andreani, G Beaudoin, I Sagnes, and C Sirtori. "Ultra-strong light–matter coupling for designer Reststrahlen band". In: *New Journal of Physics* 16.4 (Apr. 2014), p. 043029. DOI: `10.1088/1367-2630/16/4/043029`.

[23] R. H. Dicke. “Coherence in Spontaneous Radiation Processes”. In: *Phys. Rev.* 93 (1 Jan. 1954), pp. 99–110. DOI: `10.1103/PhysRev.93.99`.

[24] Dimitri Dini, Rüdeger Köhler, Alessandro Tredicucci, Giorgio Biasiol, and Lucia Sorba. “Microcavity Polariton Splitting of Intersubband Transitions”. In: *Phys. Rev. Lett.* 90 (11 Mar. 2003), p. 116401. DOI: `10.1103/PhysRevLett.90.116401`.

[25] Yanko Todorov, Lorenzo Tosetto, Aymeric Delteil, Angela Vasanelli, C Sirtori, AM Andrews, and G Strasser. “Polaritonic spectroscopy of intersubband transitions”. In: *Physical Review B* 86.12 (2012), p. 125314.

[26] Yanko Todorov and Carlo Sirtori. “Few-Electron Ultrastrong Light-Matter Coupling in a Quantum LC Circuit”. In: *Phys. Rev. X* 4 (4 Nov. 2014), p. 041031. DOI: `10.1103/PhysRevX.4.041031`.

[27] A. Delteil, A. Vasanelli, Y. Todorov, C. Feuillet Palma, M. Renaudat St-Jean, G. Beaudoin, I. Sagnes, and C. Sirtori. “Charge-Induced Coherence between Intersubband Plasmons in a Quantum Structure”. In: *Phys. Rev. Lett.* 109 (2012), p. 246808.

[28] M. Malerba, T. Ongarello, B. Paulillo, J.-M. Manceau, G. Beaudoin, I. Sagnes, F. De Angelis, and R. Colombelli. “Towards strong light-matter coupling at the single-resonator level with sub-wavelength mid-infrared nano-antennas”. In: *Applied Physics Letters* 109.2 (July 2016), p. 021111. ISSN: 0003-6951. DOI: `10.1063/1.4958330`.

[29] Raktim Sarma, Nishant Nookala, Kevin James Reilly, Sheng Liu, Domenico de Ceglia, Luca Carletti, Michael D Goldflam, Salvatore Campione, Keshab Sapkota, Huck Green, et al. “Strong coupling in all-dielectric intersubband polaritonic metasurfaces”. In: *Nano Letters* 21.1 (2020), pp. 367–374.

[30] Raymond Gillibert, Mario Malerba, Davide Spirito, Valeria Giliberti, Lianhe Li, A. Giles Davies, Edmund H. Linfield, Leonetta Baldassarre, Raffaele Colombelli, and Michele Ortolani. “Nanospectroscopy of a single patch antenna strongly coupled to a mid-infrared intersubband transition in a quantum well”. In: *Applied Physics Letters* 117.10 (Sept. 2020), p. 101104. ISSN: 0003-6951. DOI: `10.1063/5.0018865`.

[31] Mario Malerba, Simone Sotgiu, Andrea Schirato, Leonetta Baldassarre, Raymond Gillibert, Valeria Giliberti, Mathieu Jeannin, Jean-Michel Manceau, Lianhe Li, Alexander Giles Davies, Edmund H. Linfield, Alessandro Alabastri, Michele Ortolani, and Raffaele Colombelli. “Detection of Strong Light–Matter Interaction in a Single Nanocavity with a Thermal Transducer”. In: *ACS Nano* 16.12 (2022). PMID: 36399696, pp. 20141–20150. DOI: `10.1021/acsnano.2c04452`.

[32] D Dietze, AM Andrews, P Klang, G Strasser, K Unterrainer, and J Darmo. “Ultrastrong coupling of intersubband plasmons and terahertz metamaterials”. In: *Applied Physics Letters* 103 (2013), p. 20.

[33] RC Miller, AC Gossard, DA Kleinman, and O Munteanu. “Parabolic quantum wells with the G a A s- Al x Ga 1- x As system”. In: *Physical Review B* 29.6 (1984), p. 3740.

[34] C Deimert, P Goulain, J-M Manceau, W Pasek, T Yoon, A Bousseksou, NY Kim, R Colombelli, and ZR Wasilewski. "Realization of harmonic oscillator arrays with graded semiconductor quantum wells". In: *Physical Review Letters* 125.9 (2020), p. 097403.

[35] Michele Montanari, Chiara Ciano, Luca Persichetti, Cedric Corley, Leonetta Baldassarre, Michele Ortolani, Luciana Di Gaspare, Giovanni Capellini, David Stark, Giacomo Scalari, et al. "THz intersubband absorption in n-type Si1- xGex parabolic quantum wells". In: *Applied Physics Letters* 118 (2021), p. 16.

[36] Elena Campagna, Enrico Talamas-Simola, Tommaso Venanzi, Fritz Berkmann, Cedric Corley-Wiciak, Giuseppe Nicotra, Leonetta Baldassarre, Giovanni Capellini, Luciana Di Gaspare, Michele Virgilio, Michele Ortolani, and Monica De Seta. "High-quality CMOS compatible n-type SiGe parabolic quantum wells for intersubband photonics at 2.5–5 THz". In: *Nanophotonics* 13 (2024), pp. 1793–1802. DOI: `doi:10.1515/nanoph-2023-0704`.

[37] Giovanni Capellini, Monica De Seta, Yan Busby, Marialilia Pea, Florestano Evangelisti, Giovanni Nicotra, Corrado Spinella, Michele Nardone, and Claudio Ferrari. "Strain relaxation in high Ge content SiGe layers deposited on Si". In: *Journal of Applied Physics* 107 (2010), p. 6.

[38] Oliver Skibitzki, Marvin H Zoellner, Fabrizio Rovaris, Markus Andreas Schubert, Yuji Yamamoto, Luca Persichetti, Luciana Di Gaspare, Monica De Seta, Riccardo Gatti, Francesco Montalenti, et al. "Reduction of threading dislocation density beyond the saturation limit by optimized reverse grading". In: *Physical Review Materials* 4.10 (2020), p. 103403.

[39] Y Busby, M De Seta, G Capellini, F Evangelisti, M Ortolani, MICHELE Virgilio, GIUSEPPE Grosso, G Pizzi, P Calvani, S Lupi, et al. "Near-and far-infrared absorption and electronic structure of Ge-SiGe multiple quantum wells". In: *Physical Review B* 82.20 (2010), p. 205317.

[40] Michele Virgilio, Diego Sabbagh, Michele Ortolani, Luciana Di Gaspare, Giovanni Capellini, and Monica De Seta. "Physical mechanisms of intersubband-absorption linewidth broadening in s-Ge/SiGe quantum wells". In: *Physical Review B* 90.15 (2014), p. 155420.

[41] Takeya Unuma, Masahiro Yoshita, Takeshi Noda, Hiroyuki Sakaki, and Hidefumi Akiyama. "Intersubband absorption linewidth in GaAs quantum wells due to scattering by interface roughness, phonons, alloy disorder, and impurities". In: *Journal of applied physics* 93.3 (2003), pp. 1586–1597.

[42] Yanko Todorov. "Dipolar quantum electrodynamics of the two-dimensional electron gas". In: *Physical Review B* 91.12 (2015), p. 125409.

[43] Jacopo Frigerio, Andrea Ballabio, Giovanni Isella, Emilie Sakat, Giovanni Pellegrini, Paolo Biagioni, Monica Bollani, Enrico Napolitani, Costanza Manganelli, Michele Virgilio, Alexander Grupp, Marco P. Fischer, Daniele Brida, Kevin Gallacher, Douglas J. Paul, Leonetta Baldassarre, Paolo Calvani, Valeria Giliberti, Alessandro Nucara, and

Michele Ortolani. "Tunability of the dielectric function of heavily doped germanium thin films for mid-infrared plasmonics". In: *Phys. Rev. B* 94 (8 Aug. 2016), p. 085202. DOI: `10.1103/PhysRevB.94.085202`.

[44] F. Berkmann, O. Steuer, F. Ganss, S. Prucnal, D. Schwarz, I. A. Fischer, and J. Schulze. "Sharp MIR plasmonic modes in gratings made of heavily doped pulsed laser-melted Ge1-xSnx". In: *Opt. Mater. Express* 13.3 (Mar. 2023), pp. 752–763. DOI: `10.1364/OME.479637`.

[45] Cheryl Feuillet-Palma, Yanko Todorov, Robert Steed, Angela Vasanelli, Giorgio Biasiol, Lucia Sorba, and Carlo Sirtori. "Extremely sub-wavelength THz metal-dielectric wire microcavities". In: *Opt. Express* 20.27 (Dec. 2012), pp. 29121–29130. DOI: `10.1364/OE.20.029121`.

[46] M. Zału żny and C. Nalewajko. "Coupling of infrared radiation to intersubband transitions in multiple quantum wells: The effective-medium approach". In: *Phys. Rev. B* 59 (20 May 1999), pp. 13043–13053. DOI: `10.1103/PhysRevB.59.13043`.

[47] Denis Langevin, Clément Verlhac, Julien Jaeck, Loubnan Abou-Hamdan, Eva Taupeau, Baptiste Fix, Nathalie Bardou, Christophe Dupuis, Yannick De Wilde, Riad Haıdar, et al. "Experimental Investigation of the Thermal Emission Cross Section of Nanoresonators Using Hierarchical Poisson-Disk Distributions". In: *Physical Review Letters* 132.4 (2024), p. 043801.

[48] Y. Todorov, A. M. Andrews, R. Colombelli, S. De Liberato, C. Ciuti, P. Klang, G. Strasser, and C. Sirtori. "Ultrastrong Light-Matter Coupling Regime with Polariton Dots". In: *Phys. Rev. Lett.* 105.19 (Nov. 2010), p. 196402. DOI: `10.1103/PhysRevLett.105.196402`.

[49] Yize Stephanie Li and John Nguyen. "Tensilely strained Ge films on Si substrates created by physical vapor deposition of solid sources". In: *Scientific reports* 8.1 (2018), p. 16734.

[50] J.-M. Manceau, N.-L. Tran, G. Biasiol, T. Laurent, I. Sagnes, G. Beaudoin, S. De Liberato, I. Carusotto, and R. Colombelli. "Resonant intersubband polariton-LO phonon scattering in an optically pumped polaritonic device". In: *Applied Physics Letters* 112.19 (May 2018), p. 191106. ISSN: 0003-6951. DOI: `10.1063/1.5029893`.

[51] Jürgen Raab, Francesco P. Mezzapesa, Leonardo Viti, Nils Dessmann, Laura K. Diebel, Lianhe Li, A. Giles Davies, Edmund H. Linfield, Christoph Lange, Rupert Huber, and Miriam S. Vitiello. "Ultrafast terahertz saturable absorbers using tailored intersubband polaritons". In: *Nature Communications* 11.1 (2020), p. 4290. DOI: `10.1038/s41467-020-18004-8`.

[52] Denis G. Baranov, Battulga Munkhbat, Elena Zhukova, Ankit Bisht, Adriana Canales, Benjamin Rousseaux, Göran Johansson, Tomasz J. Antosiewicz, and Timur Shegai. "Ultrastrong coupling between nanoparticle plasmons and cavity photons at ambient con-

ditions". In: *Nature Communications* 11 (1 2020), p. 2715. DOI: `10.1038/s41467-020-16524-x`.

[53] Mathieu Jeannin, Jean-Michel Manceau, and Raffaele Colombelli. "Unified Description of Saturation and Bistability of Intersubband Transitions in the Weak and Strong Light-Matter Coupling Regimes". In: *Phys. Rev. Lett.* 127 (18 Oct. 2021), p. 187401. DOI: `10.1103/PhysRevLett.127.187401`.

[54] Enrico Talamas Simola, Michele Montanari, Cedric Corley-Wiciak, Luciana Di Gaspare, Luca Persichetti, Marvin H Zöllner, Markus A Schubert, Tommaso Venanzi, Marina Cagnon Trouche, Michele Ortolani, et al. "Subnanometer control of the heteroepitaxial growth of multimicrometer-thick Ge/Si-Ge quantum cascade structures". In: *Physical Review Applied* 19.1 (2023), p. 014011.

5

CHALLENGES IN MODULATION DOPING OF N-TYPE GE/SIGE HETEROSTRUCTURES: THE ROLE OF EPITAXIAL AND THERMAL STRAINS

In the previous articles, we demonstrated the feasibility of growing high-quality SiGe parabolic quantum wells (PQWs) and highlighted their potential for THz optoelectronics. A crucial next step toward the development of devices operating in the strong-coupling regime, where the Rabi frequency scales as $\sqrt{n_{2D}} \propto 2\Omega_R$, is the optimization of the modulation doping, which directly determines the carrier density and thus the strength of the light-matter interaction.

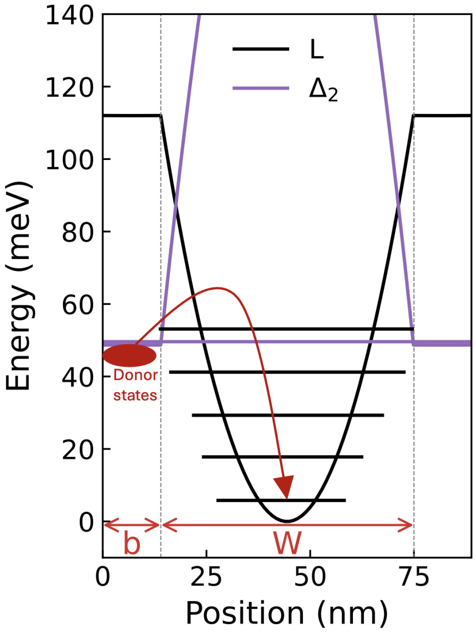

Figure 5.1: *Band profile of a Ge/Si$_{0.18}$Ge$_{0.82}$ heterostructure for the L (black) and Δ_2 (purple) bands. Quantized levels inside the well due to the L valley confinament potential are also shown.*

The purpose of this study is to investigate the influence of strain on the modulation-doping mechanism in n-type Ge/SiGe heterostructures, with a particular focus on parabolic quantum wells. The mechanical tensile strain significantly affects the charge-transfer process when phosphorus donors are incorporated into Ge-rich SiGe barriers. As discussed in Section 1.3.2, in Ge/SiGe heterostructures, strain originates from two distinct contributions: epitaxial strain, due to the lattice mismatch between Si and Ge, and thermal strain, resulting from the different thermal expansion coefficients of these materials. Both contributions modify the band structure and thus critically impact the efficiency of modulation doping. This is due to the close energy of the Δ and L band minima in this Ge compositional range. Furthermore, their energy separation depends on the strain status of the structure.

The structures examined in this study consist of a strain-compensated stack of compressively strained Ge wells embedded between tensile-strained $Si_{0.18}Ge_{0.82}$ barriers. Under tensile strain, the SiGe conduction-band valleys split into the Δ_2 and Δ_4 subbands. As discussed in Section 1.3.3 in the tensile-strained barriers, the conduction-band minimum lies in the Δ_2 valley, while in the Ge well, the minimum lies in the L valley, as shown in the band structure presented in Figure 5.1. This valley configuration defines the energy separation between the well and barrier states, which governs the transfer of electrons from the ionized donors in the barrier to the bound L states in the well. This energy spacing is further modified by quantum confinement in both the well and the barrier, which depends strongly on the alloy composition, effective masses, and band bending. In addition to the limited energy separation $\Delta_2 - L$, the effective electron density n_{2D} can be reduced due to compensation effects from residual acceptors in Ge/SiGe. However, at the concentrations used in this work, dopant deactivation is negligible.

The results presented in this article, published in APL Materials [53], combine experimental characterization with theoretical modeling to elucidate how the total strain (epitaxial + thermal) impacts the process of modulation doping in Ge/SiGe PQWs. I contributed to the preparation of the manuscript and played a central role in both the experimental and modeling efforts. The manuscript won 3rd place in the ”APL Materials Excellence in Research Award”. In particular, through intersubband absorption measurements, we quantified the value of n_{2D} at different temperatures in a specific sample. Through XRD measurements, we experimentally quantified the thermal and epitaxial strain at different temperatures. Moreover, using the theoretical model described in Chapter 2.5, we calculated the value of n_{2D} as a function of T, verifying that the model is in good agreement with the experimental data. Once the theoretical model was validated, we studied the doping efficiency and the behavior of n_{2D} as a function of well thickness and barrier doping at different temperatures.

High-quality samples were grown by ultra-high vacuum chemical vapor deposition (UHV-CVD). I acquired FTIR absorption spectra in the 4-6 THz range at Sapienza University with Dr. Fritz Berkmann using transmission geometry to extract the intersubband response of PQWs with different thicknesses and doping levels. The structural analysis was carried out in collaboration with IHP Microelectronics within the framework of the IHP-RM3 Joint Lab, where, with the help of Dr. Marvin Zöllner, we performed HR-XRD measurements using a DCS500 cooling stage and a DHS1100 heating stage, covering temperatures from -180 °C to 480 °C in steps of 50 °C. I developed a dedicated Python code for data processing and performed numerical simulations using a multi-valley Schrödinger-Poisson solver provided by Prof. Michele Virgilio. These simulations were fundamental for interpreting the experiments and quantifying the contributions of band bending, confinement energies, and strain to the charge-transfer mechanism. An important outcome of this analysis is that we demonstrated the possibility of increasing the modulation-doping efficiency through strain engineering. In particular, it is possible to reduce the tensile strain in the quantum well and consequently raise the energy of the Δ valleys in the barrier by introducing a compressive strain via the tuning of the Ge content, y, in the virtual substrate (as discussed in Section 2.1). This mechanism enhances the energy detuning between the well L-valley states and the barrier Δ_2 states, thereby improving the charge-transfer efficiency. The tuning of y must, however, remain within appropriate limits, since excessive compressive strain would induce plastic relaxation, compromising both the structural quality and the intended band-structure engineering. Our combined experimental-theoretical analysis demonstrates that modulation doping efficiency is strongly influenced by the interplay of confinement, band bending, and both epitaxial and thermal strain, which together determine the energy difference between the L-valley states in the well and the Δ_2-valley states in the barrier. The simulations predict transfer efficiencies approaching 100% at low temperatures for carrier densities of approximately $1 \times 10^{11}\text{cm}^2$. These results provide key guidelines for the optimal design of SiGe PQWs, enabling precise tuning of the electronic population and, consequently, of the light-matter coupling strength. Such behavior is consistent with trends reported in earlier studies on donor activation and valley engineering in strained SiGe heterostructures, which similarly highlight the sensitivity of charge transfer to the Δ-L energy splitting and strain state of the barriers.[54, 55, 56] However, previously reported structures typically achieved transfer efficiencies limited to partial activation at low temperatures, especially in Ge-rich or tensile-strained barriers. In contrast, our combined experimental-theoretical analysis demonstrates that by jointly controlling epitaxial and thermal strain, it is possible to reach nearly complete transfer, with efficiencies approaching 100% for carrier densities of order $10^{11}cm^{-2}$. This comparison underscores how strain engineering provides a more effective route to modulation-doping optimization than approaches based solely on barrier composition or doping concentration reported so far. Overall, this work represents an important step toward the realization of CMOS-compatible quantum photonic devices operating in the THz range, demonstrating how strain engineering, doping design, and quantum confinement must be jointly optimized to achieve efficient modulation doping in Ge/SiGe heterostructures.

APL Materials

RESEARCH ARTICLE | JUNE 10 2025

Challenges in modulation doping of n-type Ge/SiGe heterostructures: The role of epitaxial and thermal strain

E. Campagna ; E. Talamas Simola ; L. Di Gaspare ; D. Marian ; M. H. Zoellner ; F. Berkmann ; L. Baldassarre ; M. Ortolani ; G. Capellini ; M. Virgilio ✉ ; M. De Seta

APL Mater. 13, 061112 (2025)
https://doi.org/10.1063/5.0259848

AIP Publishing

APL Materials ARTICLE pubs.aip.org/aip/apm

Challenges in modulation doping of n-type Ge/SiGe heterostructures: The role of epitaxial and thermal strain

Cite as: APL Mater. 13, 061112 (2025); doi: 10.1063/5.0259848
Submitted: 21 January 2025 • Accepted: 24 May 2025 •
Published Online: 10 June 2025

E. Campagna,[1] E. Talamas Simola,[1] L. Di Gaspare,[1] D. Marian,[2] M. H. Zoellner,[3] F. Berkmann,[4] L. Baldassarre,[5] M. Ortolani,[5] G. Capellini,[1,3] M. Virgilio,[2,a)] and M. De Seta[1,b)]

AFFILIATIONS

[1] Dipartimento di Scienze, Università degli Studi Roma Tre, Viale G. Marconi 446, Roma 00146, Italy
[2] Dipartimento di Fisica "E. Fermi," Università di Pisa, Largo Pontecorvo 3, Pisa 56127, Italy
[3] IHP-Leibniz Institut für Innovative Mikroelektronik, Im Technologiepark 25, Frankfurt (Oder) 15236, Germany
[4] EFM—Experimental Physics and Functional Materials, BTU Cottbus, 03046 Cottbus, Germany
[5] Department of Physics, Sapienza Università di Roma, Piazzale Aldo Moro 2, 00185 Rome, Italy

[a)] Author to whom correspondence should be addressed: michele.virgilio@unipi.it
[b)] Electronic mail: monica.deseta@uniroma3.it

ABSTRACT

N-type Ge-rich Ge/SiGe multi-quantum-wells on Si(001) substrates are a novel material system with great potential due to their compatibility with the CMOS standard. This class of strained quantum heterostructures exhibits different band edge minima in a narrow energy range. Thus, lattice deformation, quantum confinement, and band bending effects can affect the energy ordering of the associated subband states, resulting in a radical variation of their optical and transport properties. This study investigates how these factors influence the 2D subband carrier density in modulation-doped heterostructures. To this end, we focus on the recently demonstrated parabolic quantum well system because of its technological relevance. Using Fourier transform infrared and high-resolution x-ray diffraction spectroscopy in combination with numerical modeling, our results highlight the importance of the temperature dependence of the strain field in determining the efficiency of the charge transfer process. Furthermore, optimal design parameters are identified to achieve either the highest transfer efficiency or the absolute value of the carrier density as a function of the intersubband transition energy in the 3–8 THz range.

N-type Ge-rich SiGe multilayer heterostructures have great potential due to their compatibility with CMOS technology.[1–3] However, the realization of frontier optoelectronic devices based on this material system has been demonstrated only recently, due to peculiar challenges that have hindered the development of Ge-rich group IV epitaxy.[1,4,5] Indeed, sharp or continuously graded heterointerfaces with highly reproducible chemical profiles extending over several microns have been demonstrated on Si substrates in the last few years only.[4–7] The achieved high crystal quality[8] of these complex planar heterostructures requires mastering the epitaxial strain field $\varepsilon_{\parallel}^{epi}$, associated with the large lattice mismatch existing between silicon (a_{Si} = 5.431 Å) and germanium (a_{Ge} = 5.658 Å). This is typically addressed by using a $Si_{1-y}Ge_y$ virtual substrate (VS) whose lattice parameter, controlled by the y Ge molar fraction, is chosen to reciprocally compensate the tensile and compressive biaxial lattice deformation of the different layers composing the heterostructure, a condition that promotes the mechanical stability during the epitaxial growth of thick multilayers. As an example, for a heterostructure comprising the periodic repetition of a $Si_{1-x}Ge_x$ barrier and a Ge well layer having equal thicknesses, the y concentration of a fully relaxed VS has to be set exactly half way between x and 1 to compensate for the tensile deformation occurring in the barrier layers with the compressive one featured by the Ge wells.

In addition to the presence of this epitaxial strain, it must be considered that, upon cooling the heterostructures from the growth temperature (typically in the 650–800 K range), the strain field in each layer is also affected by the thermal strain in the plane $\varepsilon_{\parallel}^{therm}$ arising from the mismatch of the thermal expansion coefficient $\alpha(T)$ existing between the Si substrate and the Ge-rich active region. Therefore, the total in-plane strain experienced by each layer can be expressed as $\varepsilon_{\parallel} = \varepsilon_{\parallel}^{epi} + \varepsilon_{\parallel}^{therm}$.

The strain field has a direct impact on the electronic structure. As such, it has been used to engineer transport and optical properties, for example, in transistors[9] or in light emitters.[10] Furthermore, by modifying the band offsets at the heterointerfaces, the lattice strain can have an impact on vertical tunneling transport[3,4,11] and influence the charge transfer mechanism in modulation-doped heterostructures.[12] Accurate strain management is, therefore, critical, especially at low temperatures where the total strain is significantly enhanced by the increased contribution of the in-plane thermal strain component $\varepsilon_{\parallel}^{therm}$ (see Ref. 8). This is essential for optimizing the design and performance of SiGe-based quantum devices, including quantum cascade lasers, resonant tunneling diodes, and optical detectors and modulators that exploit light–matter interaction in the strong coupling regime. In this latter case, the achievement of the strong coupling condition requires carrier sheet densities exceeding 2×10^{11} cm^{-2}, underscoring the need for efficient and well-controlled transfer doping strategies.[5]

We recall here that Ge-rich $\mathrm{Si}_{1-x}\mathrm{Ge}_x$ alloys feature different band edges in a narrow energy interval above the absolute conduction minimum. In Ge, this minimum is located at the fourfold degenerate L point of the BZ, while for Ge content $x \lesssim 0.82$, it lies at the bottom of the sixfold degenerate Δ valleys. The strain field influences the energy separation of the L and Δ states since both react to the hydrostatic component of the lattice distortion; furthermore, the uniaxial part splits the energy of the Δ_6 states into Δ_4 and Δ_2 separate levels, pushing toward lower (higher) energies the Δ_2 valleys with respect to the Δ_4 ones when an in-plane tensile (compressive) biaxial deformation is applied. In light of the above considerations and due to the modest values of the conduction band offset at L featured by the Ge-rich SiGe/Ge heterointerface, a barrier Ge concentration x around 0.80 represents a typical trade-off to guarantee an effective confinement potential $\Delta E_{\mathrm{L-L}}$ for the L carriers (of the order of 130 meV) and enough energy separation $\Delta E_{\Delta-\mathrm{L}}$ between the absolute conduction band minima in the SiGe barrier (at Δ_2) and in the Ge well (at L).[12]

The relative energy separation of the Δ_2 and L subband states, respectively confined in the barrier and well regions, is key in determining both the transport and the optical properties of a given heterostructure. Such energy difference strongly depends on the chemical profile, lattice strain, confinement masses, and band bending effects, and a modification of its value significantly affects the efficiency of the well charging mechanisms, as in modulation-doped heterostructures the donor states are associated with the barrier Δ_2 levels.

To shed light on this last point, in this work we investigate the impact of epitaxial and thermal strain, confinement energy, and band bending effects on the transfer charge process in modulation-doped n-type Ge/SiGe quantum structures. To this aim, we focus on the recently demonstrated Ge/SiGe parabolic quantum wells (PQWs) because of their relevance for photonic applications in the THz range,[5,7,13–16] which is associated with the stability of their optical properties against temperature variations. As a matter of fact, modulation-doped PQWs feature a single intersubband transition (ISBT) absorption resonance, whose energy is largely independent of the carrier density and distribution in the subbands.[17] This characteristic makes PQWs an ideal quantum system for assessing the amount of transferred charge in the well by measuring the ISBT spectral weight.[18,19]

We combined high-resolution x-ray diffraction (HR-XRD) and Fourier transform infrared (FTIR) spectroscopy measurements on state-of-the-art n-type compositional graded Ge/SiGe PQWs grown by ultrahigh-vacuum chemical vapor deposition (UHV-CVD) on silicon substrates,[5,7,19] together with electronic states modeling based on a multi-valley Schroedinger–Poisson solver,[12] to provide valuable insight for design optimization, with a focus on precisely controlling the quantum well charging process, as required for various applications.[5,16]

The investigated samples consist of a periodic stack of Ge-rich PQWs separated by $\mathrm{Si}_{0.18}\mathrm{Ge}_{0.82}$ barriers having a thickness b = 15 nm. The multilayer structures, sketched in Fig. 1(a), have been grown on Si after the deposition of a reverse graded almost fully relaxed $\mathrm{Si}_{1-y}\mathrm{Ge}_y$ VS, whose final y value was varied in the range y = 0.85–0.91 to strain-balance the QW region and prevent its plastic relaxation.[8] The growth temperature of both the VS and the multilayer stack was T_G = 753 K. The parabolic confining potential was realized by continuously varying the Ge content in the region between two $\mathrm{Si}_{0.18}\mathrm{Ge}_{0.82}$ barrier layers up to 100%, which corresponds to the bottom of the PQWs. The compositional Ge content profile, measured by means of scanning transmission electron microscopy (STEM) and secondary ion mass spectrometry (SIMS), is shown in Fig. 1(b) for one of the investigated samples (S1), indicating a highly reproducible match with the nominal compositional profile. To shed light on the corresponding confining potential, we show in the inset of Fig. 1(a) the band-edge values at a $\mathrm{Si}_{0.18}\mathrm{Ge}_{0.82}$/Ge heterojunction, lattice matched to a cubic VS with y = 0.9, which represents the discontinuities occurring between the barrier and the bottom of the PQW.

Doping was achieved by phosphorus co-deposition in the d = 8–10 nm thick central region of the barrier. The donor concentration N_P has been tuned around 10^{18} cm^{-3} to obtain a total 2D carrier density per period, available for the transfer doping process, of $n_{2D}^{tot} = N_P \times d$ in the [1–15] $\times$ 10^{11} cm^{-2} range, as typically used in quantum devices. The SIMS profiles for the donor atoms in PQW samples are in good agreement with the nominal profiles, demonstrating that the P ions remain well confined in the barrier region (see Ref. 19). The comparison of the donor density measured by SIMS on thick test samples with the activated electron density obtained by optical reflectivity and Hall effect measurements indicates a donor activation ratio of ~100%, suggesting the absence of dopant segregation effects for impurity density at the 10^{18} cm^{-3} scale. Finally, the SIMS analysis highlights the presence of an exponential dopant diffusion tail with a characteristic length scale of only 3.5 nm.

Figure 1(a) evidences that the conduction band minimum occurs at L in the Ge compressive strained well and at Δ_2 in the tensile strained $\mathrm{Si}_{0.18}\mathrm{Ge}_{0.82}$ barrier. In this condition, we calculate a band offset $\Delta E_{\mathrm{L-L}}$ at the L point of about 112 meV. The energy difference $\Delta E_{\Delta-\mathrm{L}}$ is relatively small, around 50 meV. A reversed Δ_2 alignment

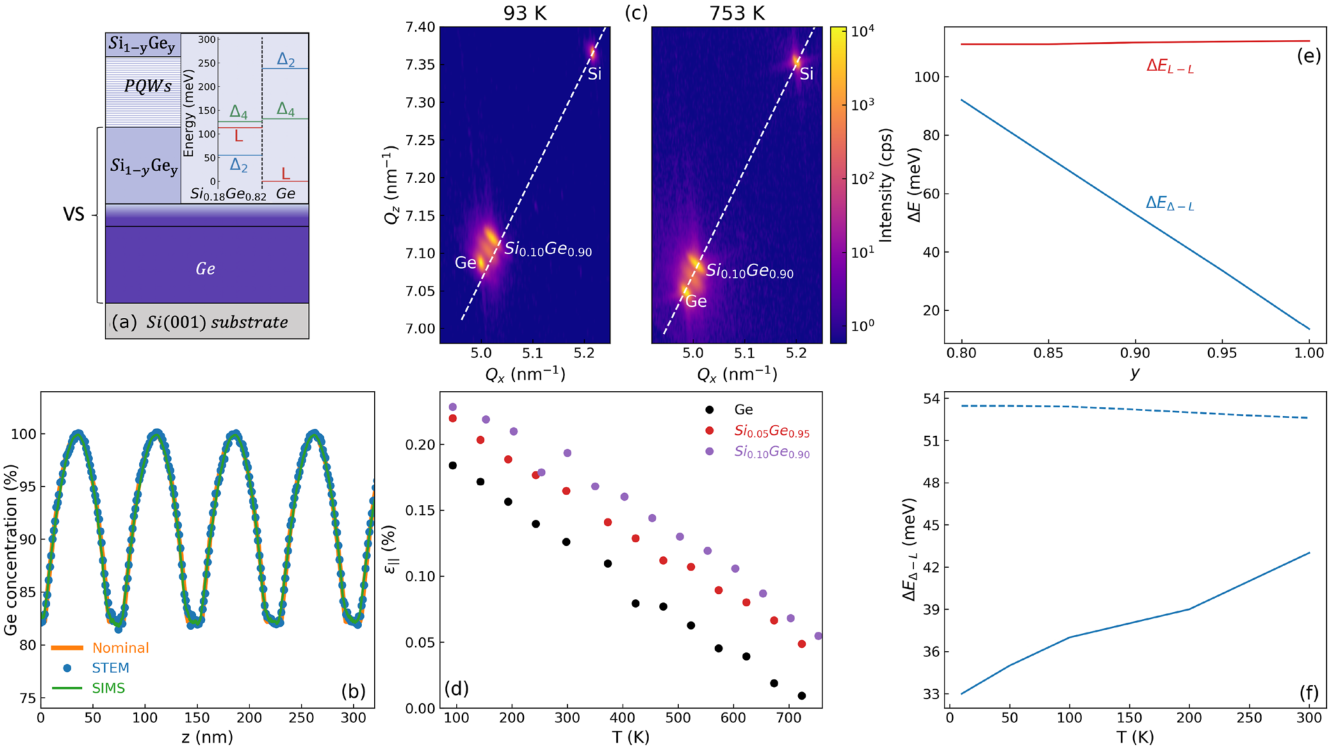

FIG. 1. (a) Sketch of the deposited multilayer structure. The periodic stack composed of PQWs and the $Si_{0.18}Ge_{0.82}$ barriers is deposited on top of the reverse graded relaxed $Si_{1-y}Ge_y$ VS. The inset shows the calculated energy positions of L, Δ_2, and Δ_4 band edges at a $Si_{0.18}Ge_{0.82}$/Ge heterointerface for $y = 0.9$. (b) Nominal Ge compositional profile for the PQW S1 sample along the growth direction (orange), compared with the ones measured by means of STEM (blue) and by SIMS (green). (c) (224) XRD maps of a reverse graded VS with final Ge content $y = 0.9$, acquired at 93 and 753 K. The dashed white line represents the calculated component of the transferred momentum for a relaxed cubic SiGe alloy. (d) In-plane strain $\varepsilon_{\parallel}(T)$ of the Ge and $Si_{0.1}Ge_{0.9}$ layers of the VS as a function of the temperature resulting from the XRD measurements. The data relative to a $Si_{0.05}Ge_{0.95}$ VS are also shown for comparison. (e) Calculated energy differences between the Δ_2–L and L–L edges at the $Si_{0.18}Ge_{0.82}$/Ge heterointerface at low T as a function of the VS Ge content y. (f) Calculated $\Delta E_{\Delta-L}$ as a function of T, including (continuous line) and neglecting (dashed line) the thermal strain for the same interface of (d) with $y = 0.9$.

is observed, leading to Δ_2 subband confinement within the SiGe barrier layers. It is important to note that the strain-dependent values of ΔE_{L-L} and $\Delta E_{\Delta-L}$ play a critical role in determining carrier confinement within the Ge well and the effectiveness of the transfer doping mechanism, respectively.

To disentangle the thermal and epitaxial contribution to the lattice strain field, we have first experimentally quantified $\varepsilon_{\parallel}(T)$ in two SiGe reversed graded VS samples featuring a final Ge concentration $y = 0.9$ and $y = 0.95$, using high resolution (224) XRD maps acquired in the temperature range spanning between 93 K and the growth temperature $T_G = 753$ K.

In Fig. 1(c), we display the XRD reciprocal space maps acquired on the $Si_{0.1}Ge_{0.9}$ VS at $T_G = 93$ K (left) and $T = 753$ K (right). The white dashed line represents the so-called "relaxation line" that evidences the relationship between the in-plane component Q_x and the out-of-plane component Q_z of the momentum transfer vector for a relaxed (cubic) lattice cell. We can clearly distinguish at $Q_x \simeq 5.2$ nm^{-1} the (224) peak of the Si reciprocal lattice point (RLP) corresponding to the substrate lattice, which moves along the relaxation line as the temperature changes, maintaining its cubic symmetry. At a lower value of $Q_x \simeq 5.0$ nm^{-1}, we observe the RLPs corresponding to the virtual substrate, with the two most intense peaks associated with the constant composition Ge and $Si_{0.1}Ge_{0.9}$ layer. It is evident that upon lowering T, the RLPs of Ge and $Si_{0.1}Ge_{0.9}$ layers move above the relaxation line, pointing to an accumulation of in-plane tensile strain in the VS.[20]

From XRD maps, the temperature dependence of $\varepsilon_{\parallel}$ in the SiGe and Ge layers can be quantitatively assessed in the whole temperature range of interest, following Ref. 20. As shown in Fig. 1(d), the $Si_{0.1}Ge_{0.9}$ and Ge lattices are practically fully relaxed around the growth temperature, while the lowering of T induces a monotonic increase in the tensile biaxial strain, whose value at 73 K is of the order of 0.2%. The T-independent offset that appears between the $Si_{0.1}Ge_{0.9}$ and Ge $\varepsilon_{\parallel}(T)$ values in Fig. 1(d) is to be attributed to the residual epitaxial tensile strain $\varepsilon_{\parallel}^{epi}(y = 0.9, T_G)$ of the SiGe layer, present at the growth temperature, of the order of 10^{-4}, arising from its aforementioned incomplete plastic relaxation on the fully relaxed underlying Ge buffer region.[21] It is evident how the less mismatched $Si_{0.05}Ge_{0.95}$ VS, also shown in Fig. 1(d) for comparison, features a lower value of $\varepsilon_{\parallel}$.

The increase in the in-plane lattice strain value observed for a decreasing measurement temperature is fully accounted for by the following relationship, as discussed in Ref. 20:

$$\varepsilon_{\parallel}(y,T) = \varepsilon_{\parallel}^{therm}(y,T) + \varepsilon_{\parallel}^{epi}(y,T_G) \tag{1}$$

with

$$\varepsilon_{\parallel}^{therm}(y,T) = \int_{T}^{T_G} [\alpha_{Si_{1-y}Ge_y}(T') - \alpha_{Si}(T')]dT', \tag{2}$$

where T_G is the growth temperature and $\alpha_{Si_{1-y}Ge_y}$ and α_{Si} are the temperature dependent thermal expansion constants of the VS and Si wafer lattices whose functional dependence on T controls the negative slope observed in Fig. 1(d), respectively.

We now focus on the electronic band offsets at the $\mathrm{Si_{0.18}Ge_{0.82}}$/Ge heterojunction, addressing first the role of the epitaxial strain. We show in Fig. 1(e) $\Delta E_{\Delta-\mathrm{L}}$ and $\Delta E_{\mathrm{L-L}}$ calculated at low T as a function of the y concentration in the relaxed VS. While the well depth $\Delta E_{\mathrm{L-L}}$ is affected only weakly by the strain field, $\Delta E_{\Delta-\mathrm{L}}$ significantly decreases upon increasing y, since the larger values of the tensile deformation shift downward the Δ_2 valleys in the barrier. Consequently, we expect that $\Delta E_{\Delta-\mathrm{L}}$ also varies with T, since the thermal strain $\varepsilon_{\parallel}(\mathrm{T})$ is itself temperature-dependent. To shed light on this point, in Fig. 1(f) we show $\Delta E_{\Delta-\mathrm{L}}$ as a function of T, calculated for $y = 0.9$, both neglecting (dashed line) and including (continuous line) the thermal strain. In the first case, the energy difference is quite stable against temperature variations. Conversely, when thermal strain is taken into account, the room temperature (RT) value for $\Delta E_{\Delta-\mathrm{L}}$ of 43 meV decreases down to about 32 meV at low T. This energy reduction significantly impacts the amount of carriers that can be transferred from the doped barrier into the well.

To observe and quantify this effect in realistic n-type Ge/SiGe multi-quantum-well systems, we have deposited on a $\mathrm{Si_{0.1}Ge_{0.9}}$ VS a strain compensated structure made of 25 identical PQWs having well width $W = 61$ nm (sample S1). Its flatband potential profile associated with the L and Δ_2 edges and the related wavefunctions, calculated at 10 K, neglecting and considering the thermal strain, are shown in panels (a) and (b) of Fig. 2, respectively. The thermal strain has also been considered for RT calculations, reported in Fig. 2(c). In line with the above considerations, the lowest $\Delta E_{\Delta-\mathrm{L}}$ value is obtained at low T, taking into account the thermal strain. Notice also that the amount of the energy effectively available to trigger the transfer doping may be further reduced by not equal confinement energies of Δ_2 and L subbands, related to different barrier and well layer thicknesses and confinement masses ($m_{\Delta_2} \simeq 0.9\, m_0$ and $m_L = 0.13\, m_0$).

Our simulations indicate that the PQWs host several confined states, with a constant energy separation $\hbar\omega_0 = 12$ meV (2.9 THz). The central 8 nm of the barrier layers have been doped with a donor concentration N_P of 8×10^{17} cm^{-3}, corresponding to a 2D carrier density per period of $n_{2D}^{tot} = 6.4 \times 10^{11}$ cm^{-2} to activate the ISBTs. The resulting electronic structures, obtained through the self-consistent solution of the Poisson equation and the multi-valley Schrödinger equation, are shown in panels (d) ($T = 10$ K, neglecting the thermal strain), (e) ($T = 10$ K, including thermal strain), and (f) ($T = 300$ K, including thermal strain) of Fig. 2. Note that, although the energy level spacing decreases for the Hartree contribution to the effective potential, the ISBT energy is still expected at the flatband value $\hbar\omega_0$, according to Kohn's theorem.[22] The role of the thermal strain in affecting the self-consistent potential profile is evident: the reduction of $\Delta E_{\Delta-\mathrm{L}}$ predicted at low T when the effect of $\varepsilon_{\parallel}^{therm}$ is taken into account limits the amount of transferred charge, resulting in a weaker Hartree potential and a consequently deeper well.

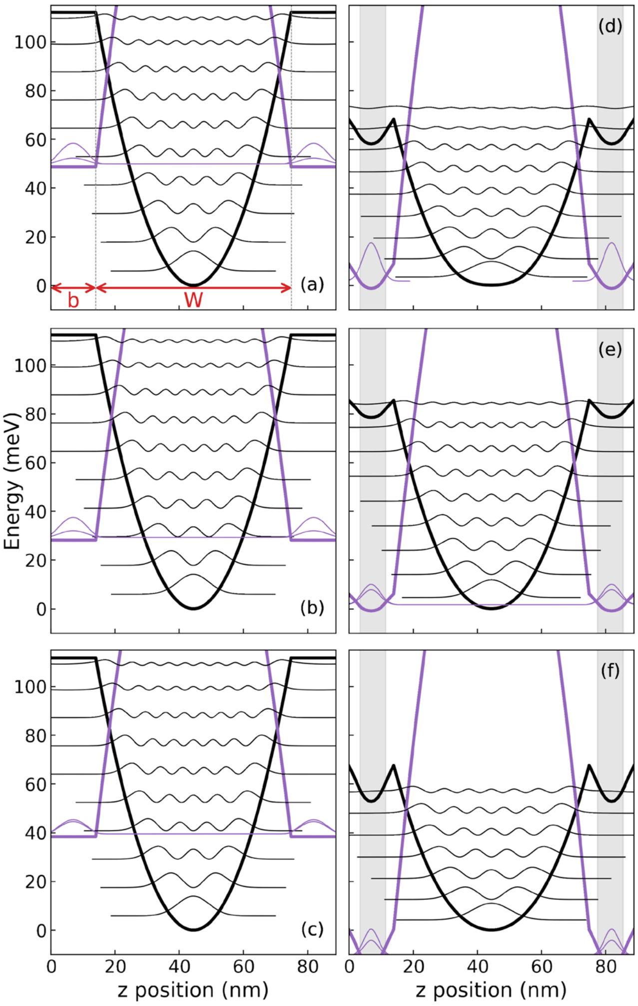

FIG. 2. Conduction band edge profiles at L (black line) and Δ_2 (purple line) along the growth direction z of sample S1. The well width W and barrier thickness b are 61 and 15 nm, respectively. The square modulus of the wavefunctions, plotted at the energy level of the corresponding quantized state, is also shown. Panels (a) and (b) show the flatband profiles calculated at 10 K, neglecting and including the thermal strain, respectively; and panel (c) shows the flatband profiles calculated at 300 K considering the thermal strain. Panels (d)–(f) are the same as panels (a)–(c) for the same structure doped in the central 8 nm of the barriers (gray region) with $N_P = 8 \times 10^{17}$ cm^{-3}.

The 2D carrier density in the L subbands calculated as a function of T, both including (red curve) and neglecting (blue curve) the thermal strain, is shown in Fig. 3(a). At RT, we obtain comparable values around $n_{2D}^{L} = 3.5 \times 10^{11}$ cm^{-2}, corresponding to a transfer

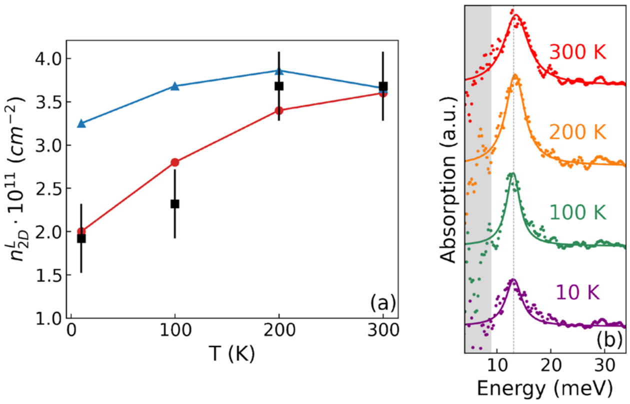

FIG. 3. (a) Calculated n_{2D}^{L} for sample S1 as a function of temperature, neglecting (blue curve) and taking into account (red curve) the thermal strain. Black symbols are the experimental values of n_{2D}^{L} obtained from the ISBT absorption spectra shown in panel (b).

efficiency $\eta = \frac{n_{2D}(L)}{n_{2D}^{tot}} = 50\%$. Lowering T, this ratio remains stable only if the $\varepsilon_{\parallel}^{therm}$ contribution to the strain field is neglected. Conversely, including this term, the transfer efficiency decreases to 30% at 10 K.

To validate these predictions, we have acquired by FTIR spectroscopy the dichroic transmission spectrum of the sample at different temperatures to isolate the ISBT contribution to the absorption spectrum and estimate the transferred charge density n_{2D}^{L}.[12] The ISBT absorption spectra reported in Fig. 3(b) feature a single peak at 12.8 meV (3.1 THz), in good agreement with the subband spacing estimated in the flatband condition $\hbar\omega_0$. Moreover, this peak energy remains extremely stable in the 10–300 K range, further confirming the achievement of a parabolic confinement potential in our compositionally graded PQWs. From the spectral weight of the 2D absorbance, we have estimated the sheet carrier density in the well, following the procedure reported in Ref. 12. The obtained experimental n_{2D}^{L} densities at different temperatures, reported in Fig. 3(a) as black squares, follow the monotonic behavior predicted by the model with the inclusion of $\varepsilon_{\parallel}^{therm}$, while they seem to be incompatible with the almost dispersionless blue curve. Remarkably, the observed reduction between RT and low T of n_{2D}^{L} values by a factor of 1.7 is also in agreement with the n_{2D}^{L} lowering estimated from the temperature dependence of the Rabi energy, measured in the ultrastrong-coupling regime in Ref. 5.

These findings highlight the critical role of thermal strain in controlling the transfer doping mechanism in n-type Ge/SiGe quantum structures and validate the predictability of the adopted theoretical model. Using this theoretical framework, we numerically investigated the transfer doping efficiency in PQWs having different widths W, i.e., designed to operate at different transition frequencies, and different dopings n_{2D}^{tot} in the [1–15] × 10^{11} cm^{-2} range. Our goal is to identify the configuration that maximizes carrier density in the well and/or transfer efficiency.

First, we performed simulations varying the PQW well width, keeping constant both the barrier thickness (15 nm) and the doping concentration ($n_{2D}^{tot} = 1.5 \times 10^{12}$ cm^{-2}). To preserve the strain compensation condition, the Ge concentration y in the VS was fine-tuned within the range [0.89–0.916]. The relative amount of transferred charge η as a function of T is shown in Fig. 4(a) for PQWs having ISBT at 3, 6, and 8 THz, corresponding to a well width of 58, 28, and 22 nm, respectively. We obtain a decrease in n_{2D}^{L} at low T for all the curves shown in Fig. 4(a).

Somewhat counterintuitively, the highest transfer efficiencies are achieved with the 8 THz PQWs, despite the higher confinement energy of the L subbands, which tends to lower $\Delta E_{\Delta-L}$ (note that the Δ_2 subbands are always found very close in energy to the Δ_2 band edge because of their large confinement mass). To understand this

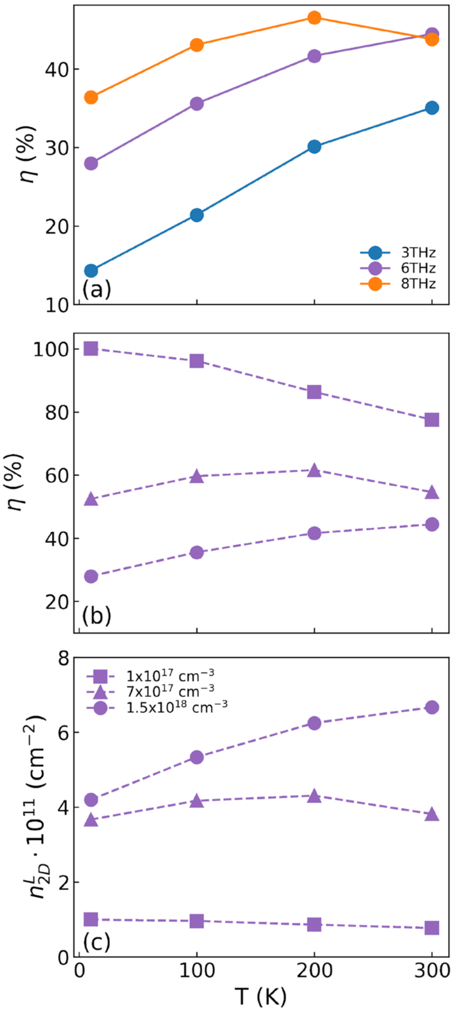

FIG. 4. (a) Calculated transfer efficiency η as a function of the temperature of PQWs having ISBT energy 3 (blue curve), 6 (purple curve), and 8 (orange curve) THz for n_{2D}^{tot} 1.5x10^{12} cm^{-2}. (b) Calculated transfer efficiency η and (c) transferred charge in the well n_{2D}^{L} as a function of temperature in 6 THz PQWs, for donor concentrations $N_d = 1 \times 10^{17}$ cm^{-3}, 7×10^{17} cm^{-3}, 1.5×10^{17} cm^{-3}, corresponding to sheet densities $n_{2D}^{tot} = 1 \times 10^{11}$ cm^{-2}) (squares), 7×10^{11} cm^{-2} (triangles), and 1.5×10^{12} cm^{-2} (circles), respectively.

effect, we observe that the transfer doping mechanism generates an electric field $\mathscr{E}$ in a region of width Δz between the center of the quantum well, where the electrons populate the L subbands, and the ionized donor region. This electric field is roughly equal to $\frac{n_{2D}^{L}}{\varepsilon}$ and produces a Hartree potential difference of about $\Delta V = \mathscr{E} \cdot \Delta z$, which reduces the energy separation of Δ_2 levels and L subbands. ΔV, for a fixed transferred charge, increases with Δz. Therefore, since the carrier flow toward the well stops when the energy of the lowest L subband states approaches the Δ_2 level in the barrier, lower values of Δz, featured just by thinner PQWs, allow larger amounts of n_{2D}^{L}. In the explored parameter range, upon decreasing the PQW width, this effect overcomes the adverse action related to higher confinement energies, thus resulting in larger n_{2D}^{L} densities.[23]

To investigate the charge transfer mechanism as a function of the doping density at different temperatures, we focus on the 6 THz PQW structure and plot the transfer efficiency η and the transferred charge density n_{2D}^{L} as a function of T, calculated for $n_{2D}^{tot} = 1 \times 10^{11}$, 7×10^{11}, and 1.5×10^{12} cm^{-2} [Figs. 4(b) and 4(c)].

We observe that for $n_{2D}^{tot} = 1 \times 10^{11}$ cm^{-2} and low T, the charge is fully transferred in the well due to the modest value of the Hartree potential difference ΔV. In this doping regime, the increase in $\Delta E_{\Delta - \mathrm{L}}$ at higher temperatures caused by a decrease in $\varepsilon_{\parallel}^{therm}$ plays a minor role since the observed trend is dominated by the thermal excitation of carriers in the Δ_2 subbands, which controls the monotonic decrease in the transfer efficiency.

In the highest doping condition, we observe an opposite behavior since the transfer process is not complete at low T, η being of the order of 30% only. In fact, despite the reduced transfer efficiency, n_{2D}^{L} is large enough to equalize the energy of the lowest L subband states and the Δ_2 level in the barrier through the action of ΔV, stopping the transfer. In this condition, the increase in $\Delta E_{\Delta - \mathrm{L}}$ at higher temperatures related to the lower $\varepsilon_{\parallel}^{therm}$ values enhances the amount of transferable carriers. The carrier transfer is also favored by the thermally induced population of excited L subbands. At the intermediate doping $n_{2D}^{tot} = 7 \times 10^{11}$ cm^{-2}, the carrier transfer is incomplete at low T with $\eta \simeq 50\%$, has a maximum at ~200 K, and then decreases at higher temperatures when the thermal excitation of Δ_2 levels becomes the dominant effect. In summary, from Figs. 4(b) and 4(c), we conclude that the optimal transfer efficiency is present at low T for 1×10^{11} cm^{-2}, while the largest absolute value of n_{2D}^{L} is obtained, in the investigated doping range, at RT for the highest doping density of 1.5×10^{12} cm^{-2}.

To further increase the transferred charge density in heavily doped samples, one can act on the tensile strain in the barrier, which can be reduced by depositing the PQW stack on a VS with a Ge content closer to the barrier. In this case, the strain-compensation condition is not satisfied, and the total thickness of the multilayered structure must not exceed the critical value for plastic relaxation.[8] To test this approach, we deposited two samples, S2 and S3, with the same multilayer structure, consisting of 15 modules of the 6 THz PQWs with doping $n_{2D}^{tot} = 1.5 \times 10^{12}$ cm^{-2} but deposited on VS substrates with different Ge compositions, i.e., $y = 0.89$ for the strain-compensated sample S2 and $y = 0.85$ for the not strain-compensated S3.

The analysis of XRD measurements, whose results are reported in the table included in Fig. 5, confirms the reproducibility of the nominally identical compositional profile in the PQW stacks of the two samples and the different strain fields, in agreement with the design values (see also the supplementary material). ISBT absorption spectra of the two samples are reported in Fig. 5(a). Both spectra consist of a single peak centered at 23 meV (5.5 THz), but the spectral weight of sample S3 is greater by a factor of 1.3, indicating that the transferred charge density in sample S3 is 30% higher with respect to the strain compensated one. This result is in line with the self-consistent band structures at 100 K reported in panels (b) and (c) for samples S2 and S3, respectively. The reduced tensile strain in the barrier featured by sample S3 has enabled a higher n_{2D}^{L} density, as testified also by the larger shrinking of the QW depth induced by the Hartree potential. Remarkably, we numerically find an increase in the transfer efficiency from 35% to 50%, perfectly matching the ratio of 1.3 for the carrier density estimated by comparing the two spectral weights of Fig. 5(a).

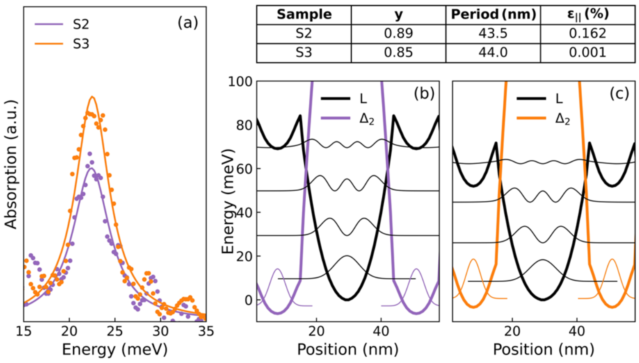

Sample	y	Period (nm)	$\varepsilon_{\parallel}$ (%)
S2	0.89	43.5	0.162
S3	0.85	44.0	0.001

FIG. 5. (a) ISBT absorption spectra of samples S2 (purple symbols) and S3 (orange symbols). (b) and (c) Band edge profiles and square modulus of the wavefunctions calculated for samples S2 and S3, respectively. In the table, the Ge content y in the VS, the period of the MPQW stack, and the average in-plane strain in the PQW stack, as determined from XRD data at 300 K, are reported.

In conclusion, we have combined XRD measurements and FTIR ISBT spectroscopy performed on n-type Ge/SiGe PQWs with their numerical modeling to shed light on the different physical effects controlling the charge transfer process in modulation-doped, Ge-rich Ge/SiGe quantum heterostructures. Our analysis shows how the efficiency of the charge transfer is critically affected by the epitaxial and thermal strain through their impact on the energy separation between the conduction band minima in the well and in the barrier material. In addition, we have numerically studied the transfer efficiency as a function of the donor concentration in the barrier and the well width in order to optimize the design to achieve either the highest carrier density in the well or the maximum transfer efficiency. Indeed, an efficiency of 100% is predicted at low T and for a carrier density of about 1×10^{11} cm^{-2}, while the largest absolute value of n_{2D}^{L} is obtained at RT for the highest investigated doping density of 1.5×10^{12} cm^{-2}, with an efficiency of about 50%. We believe that the improved degree of control over the transfer doping process, achieved in this work, represents an important step forward toward the realization of novel quantum optoelectronic devices based on this CMOS-compatible material system.

In the supplementary material, we report and discuss the 224 reciprocal space maps from the strain-compensated S2 sample and the strain unbalanced S3 sample.

M.D.S. and L.D.G. acknowledge the support of PNRR MUR project PE0000023-NQSTI Spoke 4 CUP B53C22004170006 (Bando a cascata domanda n. 0002/24 "THE UPSIDE") M.V., L.D.G., D.M., and M.D.S. acknowledge the support from the Italian MUR grant PRIN 2022 PNRR Integrable Thz Si-based Quantum Cascade Operation, Mission 4 Component 2, CUP I53D23006680001, funded by the European Union—NextGenerationEU. Part of this work has been carried out within the Joint Lab "Intelligent Electro-Optical Sensing," established between IHP and the University of Rome Tre.

AUTHOR DECLARATIONS

Conflict of Interest

The authors have no conflicts to disclose.

Author Contributions

E. Campagna: Data curation (equal); Investigation (equal); Visualization (equal); Writing – original draft (equal). **E. Talamas Simola**: Conceptualization (equal); Data curation (equal); Investigation (equal); Supervision (equal); Writing – review & editing (equal). **L. Di Gaspare**: Investigation (equal); Methodology (equal); Supervision (equal); Writing – review & editing (equal). **D. Marian**: Formal analysis (equal); Writing – review & editing (equal). **M. H. Zoellner**: Data curation (equal); Investigation (equal); Validation (equal). **F. Berkmann**: Data curation (equal); Investigation (equal). **L. Baldassarre**: Data curation (equal); Investigation (equal). **M. Ortolani**: Data curation (equal); Investigation (equal). **G. Capellini**: Formal analysis (equal); Investigation (equal); Resources (equal); Supervision (equal); Writing – review & editing (equal). **M. Virgilio**: Conceptualization (equal); Funding acquisition (equal); Investigation (equal); Methodology (equal); Software (equal); Supervision (lead); Writing – original draft (lead); Writing – review & editing (equal). **M. De Seta**: Conceptualization (lead); Funding acquisition (equal); Investigation (equal); Methodology (equal); Resources (lead); Supervision (lead); Writing – original draft (lead); Writing – review & editing (equal).

DATA AVAILABILITY

The data that support the findings of this study are available from the corresponding author upon reasonable request.

REFERENCES

[1] I. A. Fischer, M. Brehm, M. De Seta, G. Isella, D. J. Paul, M. Virgilio, and G. Capellini, "On-chip infrared photonics with Si–Ge-heterostructures: What is next?," APL Photonics **7**, 050901 (2022).

[2] D. J. Paul, "The progress towards terahertz quantum cascade lasers on silicon substrates," Laser Photonics Rev. **4**, 610–632 (2010).

[3] T. Grange, D. Stark, G. Scalari, J. Faist, L. Persichetti, L. Di Gaspare, M. De Seta, M. Ortolani, D. J. Paul, G. Capellini, S. Birner, and M. Virgilio, "Room temperature operation of *n*-type Ge/SiGe terahertz quantum cascade lasers predicted by non-equilibrium Green's functions," Appl. Phys. Lett. **114**, 111102 (2019).

[4] D. Stark, M. Mirza, L. Persichetti, M. Montanari, S. Markmann, M. Beck, T. Grange, S. Birner, M. Virgilio, C. Ciano, M. Ortolani, C. Corley, G. Capellini, L. Di Gaspare, M. De Seta, D. J. Paul, J. Faist, and G. Scalari, "THz intersubband electroluminescence from n-type Ge/SiGe quantum cascade structures," Appl. Phys. Lett. **118**, 101101 (2021).

[5] F. Berkmann, T. Venanzi, L. Baldassarre, E. Campagna, E. Talamas Simola, L. Di Gaspare, C. Corley-Wiciak, G. Capellini, G. Nicotra, G. Sfuncia, A. Notargiacomo, E. Giovine, S. Cibella, M. Virgilio, G. Scalari, M. De Seta, and M. Ortolani, "Ultrastrong coupling of Si$_{1-x}$Ge$_x$ parabolic quantum wells to terahertz microcavities," ACS Photonics **11**, 2776 (2024).

[6] T. Grange, S. Mukherjee, G. Capellini, M. Montanari, L. Persichetti, L. Di Gaspare, S. Birner, A. Attiaoui, O. Moutanabbir, M. Virgilio, and M. De Seta, "Atomic-scale insights into semiconductor heterostructures: From experimental three-dimensional analysis of the interface to a generalized theory of interfacial roughness scattering," Phys. Rev. Appl. **13**, 044062 (2020).

[7] M. Montanari, C. Ciano, L. Persichetti, C. Corley, L. Baldassarre, M. Ortolani, L. Di Gaspare, G. Capellini, D. Stark, G. Scalari, M. Virgilio, and M. De Seta, "THz intersubband absorption in n-type Si$_{1-x}$Ge$_x$ parabolic quantum wells," Appl. Phys. Lett. **118**, 163106 (2021).

[8] E. Talamas Simola, M. Montanari, C. Corley-Wiciak, L. Di Gaspare, L. Persichetti, M. H. Zöllner, M. A. Schubert, T. Venanzi, M. C. Trouche, M. Ortolani, F. Mattioli, G. Sfuncia, G. Nicotra, G. Capellini, M. Virgilio, and M. De Seta, "Subnanometer control of the heteroepitaxial growth of multimicrometer-thick Ge/Si–Ge quantum cascade structures," Phys. Rev. Appl. **19**, 014011 (2023).

[9] W. Cao, H. Bu, M. Vinet, M. Cao, S. Takagi, S. Hwang, T. Ghani, and K. Banerjee, "The future transistors," Nature **620**, 501–515 (2023).

[10] F. T. Armand Pilon, Y.-M. Niquet, J. Chretien, N. Pauc, V. Reboud, V. Calvo, J. Widiez, J. M. Hartmann, A. Chelnokov, J. Faist, and H. Sigg, "Investigation of lasing in highly strained germanium at the crossover to direct band gap," Phys. Rev. Res. **4**, 033050 (2022).

[11] K. Driscoll and R. Paiella, "Design of *n*-type silicon-based quantum cascade lasers for terahertz light emission," J. Appl. Phys. **102**, 093103 (2007).

[12] Y. Busby, M. De Seta, G. Capellini, F. Evangelisti, M. Ortolani, M. Virgilio, G. Grosso, G. Pizzi, P. Calvani, S. Lupi *et al.*, "Near- and far-infrared absorption and electronic structure of Ge–SiGe multiple quantum wells," Phys. Rev. B **82**, 205317 (2010).

[13] K. Isensee, N. Kröger-Lui, and W. Petrich, "Biomedical applications of mid-infrared quantum cascade lasers—A review," Analyst **143**, 5888–5911 (2018).

[14] J. Ulrich, R. Zobl, K. Unterrainer, G. Strasser, E. Gornik, K. D. Maranowski, and A. C. Gossard, "Temperature dependence of far-infrared electroluminescence in parabolic quantum wells," Appl. Phys. Lett. **74**, 3158–3160 (1999).

[15] M. Geiser, F. Castellano, G. Scalari, M. Beck, L. Nevou, and J. Faist, "Ultrastrong coupling regime and plasmon polaritons in parabolic semiconductor quantum wells," Phys. Rev. Lett. **108**, 106402 (2012).

[16] C. Deimert, P. Goulain, J.-M. Manceau, W. Pasek, T. Yoon, A. Bousseksou, N. Y. Kim, R. Colombelli, and Z. R. Wasilewski, "Realization of harmonic oscillator arrays with graded semiconductor quantum wells," Phys. Rev. Lett. **125**, 097403 (2020).

[17] L. Brey, N. F. Johnson, and B. I. Halperin, "Optical and magneto-optical absorption in parabolic quantum wells," Phys. Rev. B **40**, 10647 (1989).

[18] M. Geiser, G. Scalari, F. Castellano, M. Beck, and J. Faist, "Room temperature terahertz polariton emitter applied physics letters," Appl. Phys. Lett. **101**, 141118 (2012).

[19] E. Campagna, E. Talamas Simola, T. Venanzi, F. Berkmann, C. Corley-Wiciak, G. Nicotra, L. Baldassarre, G. Capellini, L. Di Gaspare, M. Virgilio, M. Ortolani, and M. De Seta, "High-quality CMOS compatible n-type SiGe parabolic quantum wells for intersubband photonics at 2.5–5 THz," Nanophotonics **13**, 1793–1802 (2024).

[20] G. Capellini, M. De Seta, P. Zaumseil, G. Kozlowski, and T. Schroeder, "High temperature x ray diffraction measurements on Ge/Si(001) heterostructures: A study on the residual tensile strain," J. Appl. Phys. **111**, 073518 (2012).

[21] O. Skibitzki, M. H. Zoellner, F. Rovaris, M. A. Schubert, Y. Yamamoto, L. Persichetti, L. Di Gaspare, M. De Seta, R. Gatti, F. Montalenti, and G. Capellini, "Reduction of threading dislocation density beyond the saturation limit by optimized reverse grading," Phys. Rev. Mater. **4**, 103403 (2020).

[22] W. Kohn, "Cyclotron resonance and de Haas-van Alphen oscillations of an interacting electron gas," Phys. Rev. **123**, 1242 (1961).

[23] The tiny variations in the strain field related to the tuning of y in the VS have a negligible impact on the transferred charge density.

CONCLUSIONS

In this thesis, we demonstrate the growth and optimization of CMOS-compatible Ge/SiGe parabolic quantum wells, and their successful implementation in THz microcavities, leading to the observation of the ultrastrong light-matter coupling regime in a group-IV system. The work combines advances in epitaxial growth, structural and optical characterization, carrier-transfer engineering, and cavity integration, establishing Ge/SiGe PQWs as a competitive alternative to III-V heterostructures for THz photonic technologies.

The first part of the thesis showed that ultra-high-vacuum chemical vapor deposition is an excellent technique for realizing high-quality Ge/Si$_{1-x}$Ge$_x$ PQWs on Si(100) substrates. By employing a reverse-graded buffer in combination with a step-graded virtual substrate, it was possible to obtain stacks of strain-compensated heterostructures with a low dislocation density. High-resolution X-ray diffraction and scanning transmission electron microscopy demonstrated the capability of the deposition technique used at Roma Tre to control, at the nanometer scale, the continuously graded $Si_{1-x}Ge_x$ composition required to form the parabolic potential. The experimentally extracted Ge profile reproduced the ideal parabolic design, with a relative deviation below 1%. The presence of sharp superlattice peaks in XRD and the excellent agreement between data and simulations confirm the crystalline quality, reproducibility, and structural periodicity of the PQW stack. STEM and SIMS analyzes further verified the high cristalline quality and the control achieved on the compositional profile to preserve the parabolic confinement at the electronic level.

Fourier-transform infrared spectroscopy revealed a single, sharp ISBT absorption resonance in all PQWs, with remarkably narrow linewidths, approximately 2 meV at low temperature and 5 meV at room temperature, and energies scaling as the inverse of the well width over the 2.5-5 THz range, as expected by the theory. The resonance energy exhibited minimal dependence on temperature and doping, in agreement with theoretical predictions for an ideal parabolic potential and with Kohn's theorem. These results provide clear evidence of harmonic confinement and the effective cancelation of electron-electron interaction effects in modulation-doped PQWs. Overall, the combination of structural and optical measurements demonstrates that Ge/SiGe PQWs are excellent candidates for THz intersubband devices operating across a wide spectral and temperature range.

The integration of PQWs into THz microcavities enabled the experimental observation, for the first time, of the ultrastrong-coupling regime in a group-IV material platform.

By embedding n-doped PQWs into metal-insulator-doped semiconductor resonators, a pronounced anticrossing was observed in the transmission spectra, with Rabi splittings corresponding to normalized coupling strengths $\eta = \Omega_R/\omega_0 = 0.2$. This result confirms the formation of ISB polaritons and the onset of ultrastrong coupling.

A crucial aspect of maximizing the light-matter interaction is controlling the two-dimensional electron density, n_L^{2D}, in the Ge wells. This thesis clarified that the efficiency of modulation doping is inherently determined by the energy separation $\Delta E_{\Delta-L}$ between the L valleys in the Ge well and the Δ_2 valleys in the barrier, which, in turn, depends on epitaxial and thermal strain, and that it can be optimized by strain engineering. Temperature-dependent HR-XRD revealed that cooling induces tensile-strain buildup in the barriers, lowering the Δ_2 minimum and thus reducing $\Delta E_{\Delta-L}$. This limits charge transfer and decreases n_L^{2D}, as confirmed by FTIR spectroscopy and Schrödinger-Poisson simulations. Optimal transfer efficiency was found at low doping and low temperatures, where values approaching 100% can be reached. Furthermore, it was demonstrated that intentionally reducing the barrier tensile strain, e.g., by growing the structure on a virtual substrate with lower Ge content, leads to larger $\Delta E_{\Delta-L}$ and a 30% increase in transferred charge (efficiency rising from 35% to 50%) compared to strain-compensated samples. This highlights the necessity of co-designing strain and doping to optimize the performance of THz intersubband devices.

The results obtained in this thesis demonstrate the potential of Ge/SiGe parabolic quantum wells for the controlled engineering of intersubband transitions in the THz domain and for integration with compact, strongly confining cavities. However, several aspects still need to be further investigated.

From the point of view of epitaxial growth, improved stability of the parabolic profile, in particular through finer control of dopant interdiffusion, is a necessary step to further reduce the observed broadening. Further optimization of the doping transfer would also be required by varying the barrier thickness.

From the optical point of view, it will be important to enhance the interaction between the PQWs and the confined fields in the patch cavities, by optimizing both the material quality and the cavity geometry, in order to reduce ohmic losses and increase the electromagnetic overlap. In this direction, the optimization of SiGe mirrors highly doped with phosphorus enables a reduction of the optical resistance and an improved field confinement. The implementation of cavities with higher quality factors or with more selective confinement could ultimately enable even more robust coupling regimes and greater spectral stability.

Finally, the native compatibility of the Ge/SiGe system with CMOS technology opens up prospects for integration on silicon photonics platforms, where future developments will have to address the implementation of active devices based on ISB transitions, such as fast modulators or on-chip polaritonic elements for truly scalable THz architectures.

List of Publications

Publications included in this thesis

1. E. Campagna, E. Talamas Simola, T. Venanzi, F. Berkmann, C. Corley-Wiciak, G. Nicotra, L. Baldassarre, G. Capellini, L. Di Gaspare, M. Virgilio, M. Ortolani, and M, De Seta. *"High-quality CMOS compatible n-type SiGe parabolic quantum wells for intersubband photonics at 2.5-5 THz"*. In: Nanophotonics 13.10 (Apr. 2024).

2. F. Berkmann, T. Venanzi, L. Baldassarre, E. Campagna, E. Talamas Simola, Luciana Di Gaspare, C. Corley-Wiciak, G. Capellini, G. Nicotra, G. Sfuncia, A. Notargiacomo, E. Giovine, S. Cibella, M. Virgilio, G. Scalari, M. De Seta, and M. Ortolani. *"Ultrastrong Coupling of* $Si_{1-x}Ge_x$ *Quantum Wells to Terahertz Microcavities"*. In: ACS Photonics 11.7 (July 2024).

3. E. Campagna, E. Talamas Simola, L. Di Gaspare, D. Marian, M. H. Zöllner, F. Berkmann, L. Baldassarre, M. Ortolani, G. Capellini, M. Virgilio, and M. De Seta. *"Challenges in modulation doping of n-type Ge/SiGe heterostructures: The role of epitaxial and thermal strain"*. In: APL Materials 13.6 (June 2025). **The article won 3rd place in the "APL Materials Excellence in Research Award"**

Publications under review or in preparation not included in this thesis

1. R. Civiero, E. Campagna, A. Cerdeira Oliveira, M.H. Zöllner, D. Impelluso, D. Chrastina, G. Capellini and G. Isella. *"Brittle-to-ductile transition and strain relaxation in* $Si_{1-x}Ge_x$ *linearly graded buffers"*. Submitted to Phys. Rev. Mat.

2. D. Ryzhak, E. Campagna, Y. Yamamoto, G. Capellini, and M.H. Zöllner. *"Effects of Annealing Temperature on the Photoluminescence Properties of Germanium Multiple Quantum Wells*. In preparation.

Conference Contribution

(Talk) E. Campagna, E. Talamas Simola, L. Di Gaspare, D. Marian, M.H. Zöllner, F. Berkmann, L. Baldassarre, M. Ortolani, G. Capellini, M. Virgilio and M. De Seta. *"Strain effect on transfer doping in Ge/SiGe PQWs"*. Young Researcher Meeting 2025, 30th September - 3rd October 2025, L'Aquila, Italy.

List of Figures

BIBLIOGRAPHY

[1] P. Forn-Díaz, L. Lamata, E. Rico, J. Kono, and E. Solano. "Ultrastrong coupling regimes of light-matter interaction". In: *Reviews of Modern Physics* 91.2 (June 2019), p. 025005. ISSN: 15390756. DOI: `10.1103/RevModPhys.91.025005`.

[2] I. A. Fischer, M. Brehm, M. De Seta, G. Isella, D. J. Paul, M. Virgilio, and G. Capellini. "On-chip infrared photonics with Si-Ge-heterostructures: What is next?" In: *APL Photonics* 7.5 (May 2022). ISSN: 23780967. DOI: `10.1063/5.0078608/2835169`.

[3] Douglas J. Paul. "The progress towards terahertz quantum cascade lasers on silicon substrates". In: *Laser & Photonics Reviews* 4.5 (Sept. 2010), pp. 610–632. ISSN: 1863-8899. DOI: `10.1002/LPOR.200910038`.

[4] David Stark, Muhammad Mirza, Luca Persichetti, Michele Montanari, Sergej Markmann, Mattias Beck, Thomas Grange, Stefan Birner, Michele Virgilio, Chiara Ciano, Michele Ortolani, Cedric Corley, Giovanni Capellini, Luciana Di Gaspare, Monica De Seta, Douglas J. Paul, Jérôme Faist, and Giacomo Scalari. "THz intersubband electroluminescence from n-type Ge/SiGe quantum cascade structures". In: *Applied Physics Letters* 118.10 (Mar. 2021). ISSN: 00036951. DOI: `10.1063/5.0041327/926261`.

[5] Cristiano Ciuti, Gérald Bastard, and Iacopo Carusotto. "Quantum vacuum properties of the intersubband cavity polariton field". In: *Physical Review B* 72.11 (Sept. 2005), p. 115303. ISSN: 10980121. DOI: `10.1103/PhysRevB.72.115303`.

[6] Markus Geiser, Fabrizio Castellano, Giacomo Scalari, Mattias Beck, Laurent Nevou, and Jérôme Faist. "Ultrastrong coupling regime and plasmon polaritons in parabolic semiconductor quantum wells". In: *Physical Review Letters* 108.10 (Mar. 2012), p. 106402. ISSN: 00319007. DOI: `10.1103/PHYSREVLETT.108.106402/SUPPLEMENT{\_}V02.PDF`.

[7] Walter Kohn. "Cyclotron Resonance and de Haas-van Alphen Oscillations of an Interacting Electron Gas". In: *Physical Review* 123.4 (Aug. 1961), p. 1242. ISSN: 0031899X. DOI: `10.1103/PhysRev.123.1242`.

[8] C. Deimert, P. Goulain, J. M. Manceau, W. Pasek, T. Yoon, A. Bousseksou, N. Y. Kim, R. Colombelli, and Z. R. Wasilewski. "Realization of Harmonic Oscillator Arrays with Graded Semiconductor Quantum Wells". In: *Physical Review Letters* 125.9 (Aug.

2020), p. 097403. ISSN: 10797114. DOI: 10.1103/PHYSREVLETT.125.097403/ENTAL{_}MATERIAL{_}WITH{_}UPDATED{_}REFERENCE{_}NUMBERS.PDF.

[9] Enrico Talamas Simola, Michele Montanari, Cedric Corley-Wiciak, Luciana Di Gaspare, Luca Persichetti, Marvin H. Zöllner, Markus A. Schubert, Tommaso Venanzi, Marina Cagnon Trouche, Michele Ortolani, Francesco Mattioli, Gianfranco Sfuncia, Giuseppe Nicotra, Giovanni Capellini, Michele Virgilio, and Monica De Seta. "Subnanometer Control of the Heteroepitaxial Growth of Multimicrometer-Thick Ge /(Si, Ge) Quantum Cascade Structures". In: *Physical Review Applied* 19.1 (Jan. 2023), p. 014011. ISSN: 23317019. DOI: 10.1103/PHYSREVAPPLIED.19.014011/SUPPLEMENTARY.PDF.

[10] Michele Montanari, Chiara Ciano, Luca Persichetti, Cedric Corley, Leonetta Baldassarre, Michele Ortolani, Luciana Di Gaspare, Giovanni Capellini, David Stark, Giacomo Scalari, Michele Virgilio, and Monica De Seta. "THz intersubband absorption in n-type Si1−xGex parabolic quantum wells". In: *Applied Physics Letters* 118.16 (Apr. 2021), p. 19. ISSN: 00036951. DOI: 10.1063/5.0048344/236392.

[11] Giuseppe Grosso and Giuseppe Pastori Parravicini. *Solid state physics*. Academic press, 2013. ISBN: 0123850312.

[12] John H. Davies. "The Physics of Low-dimensional Semiconductors: An Introduction". In: *The Physics of Low-dimensional Semiconductors* (Dec. 1997). DOI: 10.1017/CBO9780511819070.

[13] Yasuhiro. Shiraki and Noritaka. Usami. "Silicon-germanium (SiGe) nanostructures : production, properties and applications in electronics". In: *Woodhead Publishing* (2011), p. 627.

[14] Shashank Gupta, Donguk Nam, Jelena Vuckovic, and Krishna Saraswat. "Room temperature lasing unraveled by a strong resonance between gain and parasitic absorption in uniaxially strained germanium". In: *Physical Review B* 97.15 (Apr. 2018), p. 155127. ISSN: 24699969. DOI: 10.1103/PHYSREVB.97.155127/FIGURES/15/MEDIUM.

[15] Jasprit Singh. "Electronic and Optoelectronic Properties of Semiconductor Structures". In: *Electronic and Optoelectronic Properties of Semiconductor Structures* (Jan. 2003). DOI: 10.1017/CBO9780511805745.

[16] Friedrich Schäffler. "High-mobility Si and Ge structures". In: *Semiconductor Science and Technology* 12.12 (Dec. 1997), p. 1515. ISSN: 0268-1242. DOI: 10.1088/0268-1242/12/12/001.

[17] Chiara Ciano. "Silicon-Germanium heterostructures for Terahertz emission". PhD thesis. 2021.

[18] Ivan V. Markov. "Crystal Growth for Beginners. Foundations of Nucleation, Crystal Growth and Epitaxy". In: (2004), p. 546.

[19] M. Kamaratos, A. K. Sotiropoulos, and D. Vlachos. “Ultrathin films of Ge on the Si(100)2 × 1 surface”. In: *Surface and Interface Analysis* 50.2 (Feb. 2018), pp. 198–204. ISSN: 1096-9918. DOI: `10.1002/SIA.6358`.

[20] John E. Ayers. “Heteroepitaxy of Semiconductors : Theory, Growth, and Characterization”. In: *Heteroepitaxy of Semiconductors* (Oct. 2018). DOI: `10.1201/9781315221915`.

[21] J. W. Matthews and A. E. Blakeslee. “Defects in epitaxial multilayers: III. Preparation of almost perfect multilayers”. In: *Journal of Crystal Growth* 32.2 (Feb. 1976), pp. 265–273. ISSN: 0022-0248. DOI: `10.1016/0022-0248(76)90041-5`.

[22] Robert R. Reeber and Kai Wang. “Thermal expansion and lattice parameters of group IV semiconductors”. In: *Materials Chemistry and Physics* 46.2-3 (Nov. 1996), pp. 259–264. ISSN: 0254-0584. DOI: `10.1016/S0254-0584(96)01808-1`.

[23] G. Capellini, M. De Seta, P. Zaumseil, G. Kozlowski, and T. Schroeder. “High temperature x ray diffraction measurements on Ge/Si(001) heterostructures: A study on the residual tensile strain”. In: *Journal of Applied Physics* 111.7 (Apr. 2012), p. 73518. ISSN: 00218979. DOI: `10.1063/1.3702443/817927`.

[24] Douglas J. Paul. “Si/SiGe heterostructures: from material and physics to devices and circuits”. In: *Semiconductor Science and Technology* 19.10 (Sept. 2004), R75. ISSN: 0268-1242. DOI: `10.1088/0268-1242/19/10/R02`.

[25] Michele Virgilio and Giuseppe Grosso. “Type-I alignment and direct fundamental gap in SiGe based heterostructures”. In: *Journal of Physics: Condensed Matter* 18.3 (Jan. 2006), p. 1021. ISSN: 0953-8984. DOI: `10.1088/0953-8984/18/3/018`.

[26] Manfred Helm. “Chapter 1 The Basic Physics of Intersubband Transitions”. In: *Semiconductors and Semimetals* 62.C (Jan. 1999), pp. 1–99. ISSN: 0080-8784. DOI: `10.1016/S0080-8784(08)60304-X`.

[27] Angela Vasanelli, Yanko Todorov, and Carlo Sirtori. “Ultra-strong light–matter coupling and superradiance using dense electron gases”. In: *Comptes Rendus Physique* 17.8 (Oct. 2016), pp. 861–873. ISSN: 1631-0705. DOI: `10.1016/J.CRHY.2016.05.001`.

[28] Raffaele Colombelli and Jean Michel Manceau. “Perspectives for intersubband polariton lasers”. In: *CLEO: Science and Innovations, CLEO-SI 2015* 5.1 (May 2015), p. 2267. ISSN: 21603308. DOI: `10.1103/PHYSREVX.5.011031/DELIVERABLE/E81E22B4-EF61-4CB4-A417-442E4F856306`.

[29] Ngoc Linh Tran. “Mid-Infrared Intersubband Polaritonic Devices”. In: (Nov. 2020), p. 255. DOI: `10.34894/VQ1DJA`.

[30] E. T. Jaynes and F. W. Cummings. “Comparison of Quantum and Semiclassical Radiation Theories with Application to the Beam Maser”. In: *Proceedings of the IEEE* 51.1 (1963), pp. 89–109. ISSN: 15582256. DOI: `10.1109/PROC.1963.1664`.

[31] Y. Todorov, L. Tosetto, A. Delteil, A. Vasanelli, C. Sirtori, A. M. Andrews, and G. Strasser. "Polaritonic spectroscopy of intersubband transitions". In: *Physical Review B - Condensed Matter and Materials Physics* 86.12 (Sept. 2012), p. 125314. ISSN: 10980121. DOI: `10.1103/PHYSREVB.86.125314/FIGURES/15/MEDIUM`.

[32] Elena Campagna, Enrico Talamas Simola, Tommaso Venanzi, Fritz Berkmann, Cedric Corley-Wiciak, Giuseppe Nicotra, Leonetta Baldassarre, Giovanni Capellini, Luciana Di Gaspare, Michele Virgilio, Michele Ortolani, and Monica De Seta. "High-quality CMOS compatible n-type SiGe parabolic quantum wells for intersubband photonics at 2.5-5 THz". In: *Nanophotonics* 13.10 (Apr. 2024), pp. 1793–1802. ISSN: 21928614. DOI: `https://doi.org/10.1515/nanoph-2023-0704`.

[33] Fritz Berkmann, Tommaso Venanzi, Leonetta Baldassarre, Elena Campagna, Enrico Talamas Simola, Luciana Di Gaspare, Cedric Corley-Wiciak, Giovanni Capellini, Giuseppe Nicotra, Gianfranco Sfuncia, Andrea Notargiacomo, Ennio Giovine, Sara Cibella, Michele Virgilio, Giacomo Scalari, Monica De Seta, and Michele Ortolani. "Ultrastrong Coupling of Si1-xGex Quantum Wells to Terahertz Microcavities". In: *ACS Photonics* 11.7 (July 2024), pp. 2776–2786. ISSN: 23304022. DOI: `10.1021/ACSPHOTONICS.4C00641`.

[34] R. People and J. C. Bean. "Calculation of critical layer thickness versus lattice mismatch for GexSi1−x/Si strained-layer heterostructures". In: *Applied Physics Letters* 47.3 (Aug. 1985), pp. 322–324. ISSN: 0003-6951. DOI: `10.1063/1.96206`.

[35] Dimitri Dini, Rüdeger Köhler, Alessandro Tredicucci, Giorgio Biasiol, and Lucia Sorba. "Microcavity polariton splitting of intersubband transitions". In: *Physical Review Letters* 90.11 (Mar. 2003), p. 116401. ISSN: 00319007. DOI: `10.1103/PHYSREVLETT.90.116401/FIGURES/4/MEDIUM`.

[36] Y Todorov, A M Andrews, I Sagnes, R Colombelli, P Klang, G Strasser, and C Sirtori. "Strong Light-Matter Coupling in Subwavelength Metal-Dielectric Microcavities at Terahertz Frequencies". In: (2009). DOI: `10.1103/PhysRevLett.102.186402`.

[37] Y Todorov, L Tosetto, J Teissier, A M Andrews, P Klang, R Colombelli, I Sagnes, G Strasser, C Sirtori, C Gmachl, F Capasso, J Faist, D L Sivco, A L Hutchinson, A Y Cho, R Köhler, A Tredicucci, F Beltram, H E Beere, E H Linfield, A G Davies, D A Ritchie, R C Iotti, A Maier, A I Fernández-Domínguez, L Martín-Moreno, F J García-Vidal, S Kumar, B S Williams, Q Qin, A W Lee, Q Hu, J L Reno, L Mahler, C Walther, D S Wiersma, S P Khanna, Y Chassagneux, W Maineults, S Barbieri, J Lockyear, A P Hibbins, J R Sambles, P A Hobson, and C R Lawrence. "Optical properties of metal-dielectric-metal microcavities in the THz frequency range". In: *Optics Express, Vol. 18, Issue 13, pp. 13886-13907* 18.13 (June 2010), pp. 13886–13907. ISSN: 1094-4087. DOI: `10.1364/OE.18.013886`.

[38] A. Delteil, A. Vasanelli, Y. Todorov, C. Feuillet Palma, M. Renaudat St-Jean, G. Beaudoin, I. Sagnes, and C. Sirtori. "Charge-induced coherence between intersubband plasmons in a quantum structure". In: *Physical Review Letters* 109.24 (Dec. 2012), p. 246808. ISSN: 00319007. DOI: `10.1103/PHYSREVLETT.109.246808/FIGURES/4/MEDIUM`.

[39] Markus Geiser, Giacomo Scalari, Fabrizio Castellano, Mattias Beck, and Jérôme Faist. "Room temperature terahertz polariton emitter". In: *Applied Physics Letters* 101.14 (Oct. 2012), p. 141118. ISSN: 00036951. DOI: `10.1063/1.4757611/127876`.

[40] Paul Goulain, Chris Deimert, Mathieu Jeannin, Stefano Pirotta, Wojciech Julian Pasek, Zbigniew Wasilewski, Raffaele Colombelli, Jean-Michel Manceau, P Goulain, M Jeannin, S Pirotta, R Colombelli, J.-M Manceau, C Deimert, Z Wasilewski, and W J Pasek. "THz Ultra-Strong Light–Matter Coupling up to 200 K with Continuously-Graded Parabolic Quantum Wells". In: *Advanced Optical Materials* 11.9 (May 2023), p. 2202724. ISSN: 2195-1071. DOI: `10.1002/ADOM.202202724`.

[41] S. M. Sze and Kwok K. Ng. "Physics of Semiconductor Devices, Third Edition". In: *Physics of Semiconductor Devices, Third Edition* (Jan. 2006), pp. 1–813. DOI: `10.1002/0470068329`.

[42] Oliver Skibitzki, Marvin H. Zoellner, Fabrizio Rovaris, Markus Andreas Schubert, Yuji Yamamoto, Luca Persichetti, Luciana Di Gaspare, Monica De Seta, Riccardo Gatti, Francesco Montalenti, and Giovanni Capellini. "Reduction of threading dislocation density beyond the saturation limit by optimized reverse grading". In: *Physical Review Materials* 4.10 (Oct. 2020), p. 103403. ISSN: 24759953. DOI: `10.1103/PHYSREVMATERIALS.4.103403/FIGURES/5/THUMBNAIL`.

[43] *Dimension Icon AFM — Bruker*.

[44] Cedric Corley-Wiciak. "Scanning X-ray Diffraction Microscopy Reveals the Nanoscale Strain Landscape of Novel Quantum Devices". eng. PhD thesis. 2024. DOI: `http://dx.doi.org/10.18452/28342`.

[45] J P Dismukes, L Ekstrom, and R J Paff. "Lattice Parameter and Density in Germanium-Silicon Alloys Lattice Parameter and Density in Germanium-Silicon Alloys1". In: ().

[46] Brian C. Smith. "Fundamentals of Fourier Transform Infrared Spectroscopy". In: (Mar. 2011). DOI: `10.1201/B10777`.

[47] Fabrizio Rovaris, Marvin H. Zoellner, Peter Zaumseil, Anna Marzegalli, Luciana Di Gaspare, Monica De Seta, Thomas Schroeder, Peter Storck, Georg Schwalb, Giovanni Capellini, and Francesco Montalenti. "Dynamics of crosshatch patterns in heteroepitaxy". In: *Physical Review B* 100.8 (Aug. 2019), p. 085307. ISSN: 24699969. DOI: `10.1103/PHYSREVB.100.085307/DELIVERABLE/0DB04743-F149-4874-A384-D57D780E675C`.

[48] Vasily I. Punegov, Sergey I. Kolosov, and Konstantin M. Pavlov. “Darwin’s approach to X-ray diffraction on lateral crystalline structures”. In: *urn:issn:2053-2733* 70.1 (Dec. 2013), pp. 64–71. ISSN: 2053-2733. DOI: `10.1107/S2053273313030416`.

[49] M. De Seta, G. Capellini, M. Ortolani, M. Virgilio, G. Grosso, G. Nicotra, and P. Zaumseil. “Narrow intersubband transitions in n-type Ge/SiGe multi-quantum wells: control of the terahertz absorption energy trough the temperature dependent depolarization shift”. In: *Nanotechnology* 23.46 (Oct. 2012), p. 465708. ISSN: 0957-4484. DOI: `10.1088/0957-4484/23/46/465708`.

[50] Andrea Ballabio, Jacopo Frigerio, Saleh Firoozabadi, Daniel Chrastina, Andreas Beyer, Kerstin Volz, and Giovanni Isella. “Ge/SiGe parabolic quantum wells”. In: *Journal of Physics D: Applied Physics* 52.41 (July 2019), p. 415105. ISSN: 0022-3727. DOI: `10.1088/1361-6463/AB2D34`.

[51] K. Ismail, J. O. Chu, K. L. Saenger, B. S. Meyerson, and W. Rausch. “Modulation-doped n-type Si/SiGe with inverted interface”. In: *Applied Physics Letters* 65.10 (Sept. 1994), pp. 1248–1250. ISSN: 0003-6951. DOI: `10.1063/1.112085`.

[52] Jacopo Frigerio, Andrea Ballabio, Giovanni Isella, Emilie Sakat, Giovanni Pellegrini, Paolo Biagioni, Monica Bollani, Enrico Napolitani, Costanza Manganelli, Michele Virgilio, Alexander Grupp, Marco P. Fischer, Daniele Brida, Kevin Gallacher, Douglas J. Paul, Leonetta Baldassarre, Paolo Calvani, Valeria Giliberti, Alessandro Nucara, and Michele Ortolani. “Tunability of the dielectric function of heavily doped germanium thin films for mid-infrared plasmonics”. In: *Physical Review B* 94.8 (Aug. 2016), p. 085202. ISSN: 24699969. DOI: `10.1103/PhysRevB.94.085202`.

[53] E. Campagna, E. Talamas Simola, L. Di Gaspare, D. Marian, M. H. Zoellner, F. Berkmann, L. Baldassarre, M. Ortolani, G. Capellini, M. Virgilio, and M. De Seta. “Challenges in modulation doping of n-type Ge/SiGe heterostructures: The role of epitaxial and thermal strain”. In: *APL Materials* 13.6 (June 2025). ISSN: 2166532X. DOI: `10.1063/5.0259848`.

[54] Michele Virgilio, Diego Sabbagh, Michele Ortolani, Luciana Di Gaspare, Giovanni Capellini, and Monica De Seta. “Physical mechanisms of intersubband-absorption linewidth broadening in s-Ge/SiGe quantum wells”. In: *Physical Review B* 90.15 (Oct. 2014), p. 155420. ISSN: 1550235X. DOI: `10.1103/PhysRevB.90.155420`.

[55] M. De Seta, G. Capellini, Y. Busby, F. Evangelisti, M. Ortolani, M. Virgilio, G. Grosso, G. Pizzi, A. Nucara, and S. Lupi. “Conduction band intersubband transitions in Ge/SiGe quantum wells”. In: *Applied Physics Letters* 95.5 (Aug. 2009). ISSN: 00036951. DOI: `10.1063/1.3198204/338079`.

[56] Luca Persichetti, Michele Montanari, Chiara Ciano, Luciana Di Gaspare, Michele Ortolani, Leonetta Baldassarre, Marvin Zoellner, Samik Mukherjee, Oussama Moutanabbir, Giovanni Capellini, Michele Virgilio, Monica De Seta, Luca Persichetti,

Michele Montanari, Chiara Ciano, Luciana Di Gaspare, Michele Ortolani, Leonetta Baldassarre, Marvin Zoellner, Samik Mukherjee, Oussama Moutanabbir, Giovanni Capellini, Michele Virgilio, and Monica De Seta. “Intersubband Transition Engineering in the Conduction Band of Asymmetric Coupled Ge/SiGe Quantum Wells”. In: *Crystals 2020, Vol. 10,* 10.3 (Mar. 2020). ISSN: 2073-4352. DOI: `10.3390/CRYST10030179`.